Aus der

Medizinischen Klinik und Poliklinik I

Klinikum der Ludwig-Maximilians-Universität München

Investigating the mechanistic role of Myeloid ecotropic insertion site 1 in atrial electrophysiology

Dissertation

zum Erwerb des Doktorgrades der Humanbiologie

an der Medizinischen Fakultät der

Ludwig-Maximilians-Universität München

vorgelegt von

Li Mo

aus

Fuxin, China

Jahr
2025

Mit Genehmigung der Medizinischen Fakultät der

Ludwig-Maximilians-Universität München

Erstes Gutachten:	Priv. Doz. Dr. Sebastian Clauß
Zweites Gutachten:	Prof. Dr. Daphne Merkus
Drittes Gutachten:	Prof. Dr. Christopher Reithmann
Dekan:	Prof. Dr. med. Thomas Gudermann

Tag der mündlichen Prüfung: 09.12.2025

Table of content

Table of content 1

Zusammenfassung (Deutsch): 3

Abstract (English): 5

List of figures 7

List of tables 8

List of abbreviations 9

1. Introduction 11

1.1 Atrial fibrillation (AF) 11
1.1.1 Clinical presentation of AF 11
1.1.2 Pathology of AF 12
1.2 Myeloid ecotropic insertion site 1 (Meis1) 16
1.2.1 The general role of Meis1 16
1.2.2 The role of Meis1 on the cardiomyocyte cell cycle 17
1.2.3 The role of Meis1 on arrhythmias 19
1.3 Hypothesis and objectives 20

2. Materials and methods 21

2.1 Ethics statement 21
2.2 Materials 21
2.3 Methods 28
2.3.1 Preparation of the 100 µM Meis1 inhibitor solution 28
2.3.2 Application of the Meis1 inhibitor *in vivo* 28
2.3.3 Echocardiography 28
2.3.4 Baseline surface ECG 30
2.3.5 Invasive EP study 31
2.3.6 Ambulatory ECG Telemetry 34
2.4 Gene expression detection 39
2.4.1 RNA isolation 39
2.4.2 Complementary DNA (cDNA) Synthesis Reaction 40
2.4.3 Primer design 41
2.4.4 qPCR 46
2.5 Immunofluorescence staining 46
2.5.1 Heart harvest and sectioning 46
2.5.2 Immunofluorescence staining 46
2.5.3 Microscopy 47

2.6 Statistical analysis 48

3. Results 49

3.1 Cardiac dimensions and systolic function were unaffected by Meis1 inhibition 49

3.2 Impaired sinus node function after Meis1 inhibition 52

3.3 Prolonged atrial refractoriness after Meis1 inhibition 54

3.4 AVN function was examined after Meis1 inhibition 55

3.5 Unchanged heart rate, P wave duration, and HRV after Meis1 inhibition 58

3.6 Unchanged ventricular conduction after Meis1 inhibition 69

3.7 Enhanced atrial arrhythmogenesis after Meis1 inhibition 71

3.8 Meis1 inhibition influenced the cell cycle-related gene expression 73

3.9 The effect of Meis1 inhibition on cell proliferation 75

4. Discussion 78

4.1 Mouse models in EP research 78

4.2 Effects of Meis1 inhibition on cardiac structure and function 79

4.3 Effects of Meis1 inhibition on cardiac EP 79

4.3.1 Effects of Meis1 inhibition on sinus node function 79

4.3.2 Meis1 inhibition on AV node function 80

4.3.3 Meis1 inhibition on ventricular conduction 81

4.4 Effects of Meis1 inhibition on atrial arrhythmogenesis 82

4.5 Effects of Meis1 on cell cycle and proliferation 83

5. Summary 86

6. Outlook 87

References 88

Acknowledgements 94

Affidavit 96

List of publications 98

Zusammenfassung (Deutsch):

Genomweite Assoziationsstudien haben ergeben, dass eine genetische Variante im MEIS1-Gen (engl. myeloid ecotrophic insertion site 1) mit dem PR-Intervall, einem intermediären Phänotyp für Vorhofflimmern (AF), assoziiert ist. Meis1 ist für seine entscheidende Rolle bei der Regeneration oder Stammzellfunktion bekannt, aber die zugrunde liegenden Mechanismen, die Meis1 mit der kardialen Elektrophysiologie verbinden, sind bisher unbekannt.

Ziel dieser Studie war es, die funktionelle Rolle von Meis1 in der kardialen Elektrophysiologie und Arrhythmogenese zu untersuchen. Das Meis1-Knockdown-Modell wurde durch Injektion eines Meis1-Hemmers in BALB/c-Mäusen etabliert. Herzstruktur und -funktion, elektrophysiologische Eigenschaften und Induzierbarkeit von Vorhofarrhythmien wurden mittels Echokardiographie, Oberflächen-EKG, Telemetrie-EKG und invasiver EP-Studie untersucht. Die Genexpression von Meis1 und seinen Zielgenen, einschließlich Cyclin D2 (CCND2), Amyloid-beta-Precursor-Protein-bindendes Familien-B-Mitglied 1 (Apbb1), Tumorprotein 53 (TP53) und Mini-Chromosome Maintenance Complex Component 3 (MCM3) sowie die Proliferation von Kardiomyozyten, Fibroblasten und Makrophagen wurden untersucht, um ein tieferes Verständnis zugrunde liegender Mechanismen zu erlangen.

Die Echokardiographie zeigte, dass Herzdimensionen und systolische Funktion durch die Meis1-Hemmung nicht beeinflusst wurden. Bei Mäusen, die mit Meis1-Inhibitoren behandelt wurden, wurden jedoch eine signifikante Sinusknotendysfunktion und eine veränderte Vorhofleitung beobachtet, die sich durch eine verlängerte Sinusknoten-Erholungszeit (SNRT) und eine verlängerte effektive Vorhofrefraktärzeit (AERP) äußerte. Die Arrhythmielast war deutlich erhöht, wie durch eine erhöhte Induzierbarkeit von Vorhofarrhythmien mit signifikant verlängerten Episoden bei mit Meis1-Inhibitoren behandelten Mäusen gezeigt wurde. Die veränderte Genexpression von CCND2 und TP53 sowie die erhöhte Proliferation von Kardiomyozyten lassen darauf schließen, dass die Regulierung des Kardiomyozyten-Zellzyklus

ein Mechanismus der durch die Behandlung mit dem Meis1-Inhibitor induzierten atrialen Arrhythmien sein könnte.

Zusammengenommen deuten diese Daten darauf hin, dass Meis1 die kardiale Elektrophysiologie und Arrhythmogenese durch die Zellzyklusregulierung von Kardiomyozyten beeinflussen könnte. Zukünftige Studien sind jedoch erforderlich, um die durch Meis1 vermittelten Mechanismen, die zu Arrhythmien führen, weiter zu untersuchen.

Abstract (English):

Genome-wide association studies discovered a genetic variant in the gene myeloid ecotrophic insertion site 1 (Meis1) was associated with PR interval, an intermediate phenotype for atrial fibrillation (AF). Meis1 is known for its crucial role in regeneration or stem cell function, but the underlying mechanisms linking Meis1 to cardiac electrophysiology (EP) are unknown so far.

The present work was explored to elucidate both the regulatory role of Meis1 in cardiac electrical activity and its contributions to arrhythmia development. A murine model of Meis1 inhibition was generated through intraperitoneal administration of the Meis1 inhibitor in BALB/c mice. Cardiac structure and function, electrophysiologic properties, and inducibility of atrial arrhythmias were evaluated by echocardiography, electrocardiogram (ECG), telemetry ECG, and invasive EP study. To elucidate the underlying mechanisms, Meis1 and its downstream targets, including Cyclin D2 (CCND2), amyloid beta precursor protein-binding family B member 1 (Apbb1), Tumor protein 53 (TP53), and minichromosome maintenance complex component 3 (MCM3), were examined, along with the proliferative activity of cardiomyocytes, fibroblasts, and macrophages.

Echocardiography showed that cardiac dimensions and systolic function were unaffected by Meis1 inhibition. However, significant sinus node dysfunction and a changed atrial conduction indicated by an increased sinus node recovery time (SNRT) and atrial effective refractory period (AERP) were observed in Meis1 inhibitor-treated mice. The arrhythmia burden was markedly elevated, as demonstrated by an increased inducibility of atrial arrhythmias with significantly prolonged episodes in Meis1 inhibitor-treated mice. The regulated gene expression of CCND2 and TP53, along with the increased proliferation of cardiomyocytes, suggests that regulation of the cardiomyocyte cell cycle might be a mechanism of the induced atrial arrhythmias by the Meis1 inhibitor treatment.

Collectively, these findings suggest that Meis1 may affect cardiac EP and arrhythmogenesis by cell cycle regulation of cardiomyocytes. Further studies are needed to investigate Meis1-mediated mechanisms leading to arrhythmias.

List of figures

Figure 1. AF epidemiology. 12
Figure 2. Membrane currents of a typical ventricular action potential. 14
Figure 3. The function of Meis1 in cardiomyocytes cell cycle. 19
Figure 4. Experimental design. 29
Figure 5. Schematic diagram for echocardiography. 30
Figure 6. illustration of lead I ECG configuration for surface ECG. ..31
Figure 7. Visualization of the catheter insertion. 33
Figure 8. Experimental design. 35
Figure 9. ETA-F10 transmitter. 36
Figure 10. Schematic illustration of implanting the transmitter. 37
Figure 11. Telemetry set up. 38
Figure 12. Representative Echocardiographic images. 49
Figure 13. EF. 50
Figure 14. Echocardiographic measurements of cardiac dimensions. 51
Figure 15. Heart weight/body weight ratio. 52
Figure 16. SNRT/BCL ratio. 53
Figure 17. The incidence of sinus pauses. 54
Figure 18. AERP. 55
Figure 19. PR interval in anesthesized mice 10 days after Meis1 inhibition (ECG) and in conscious mice over a 30-day observation (Telemetry). 56
Figure 20. AV conduction properties. 57
Figure 21. AVERP. 57
Figure 22. The incidence of AV block. 58
Figure 23. Heart rate and P wave duration in anesthesized mice 10 days after Meis1 inhibition. 59
Figure 24. 30-day heart rate in conscious mice. 60
Figure 25. 30-day P wave duration in conscious mice. 60
Figure 26. RR interval, SDRR and RMSSD. 62
Figure 27. Frequency-domain parameters of HRV. 66
Figure 28. QRS interval and QTc interval in anesthesized mice 10 days after Meis1 inhibition (ECG) and in conscious mice over a 30-day observation (Telemetry). 70
Figure 29. VERP. 71
Figure 30. Inducibility of atrial arrhythmias. 72
Figure 31. Average number of tachycardia and bradycardia episodes. 73
Figure 32. Gene expression of Meis1 and its target genes. 75
Figure 33. Immunofluorescence staining of Ki67. 77

List of tables

Table 1. Antibodies 21
Table 2. Chemicals and reagents 22
Table 3. Solutions and buffers 24
Table 4. Consumables and Instruments 25
Table 5. Equipment and software 26
Table 6. Annealed RNA components 41
Table 7. Reverse transcription reactions 41
Table 8. Primers design 42
Table 9. PCR reactions for annealing temperature test 43
Table 10. PCR protocol for annealing temperature test 44
Table 11. Reactions for DNA arylamide gel test 44
Table 12. cDNA dilutions 45
Table 13. PCR program for cDNA standards test 45
Table 14. RR interval 63
Table 15. SDRR 63
Table 16. RMSSD 64
Table 17. Percentage of VLF 66
Table 18. Percentage of LF 67
Table 19. Percentage of HF 68
Table 20. LF/HF ratio 68

List of abbreviations

AERP	Atrial effective refractory period
AF	Atrial fibrillation
ANS	Autonomic nervous system
Apbb1	Amyloid beta precursor protein-binding family B member1
APD	Action potential duration
ARIC	Atherosclerosis risk in communities
AV	Atrioventricular
AVERP	Atrioventricular effective refractory period
AVN	Atrioventricular node
BCAA	Branched-chain amino acids
CCND2	Cyclin D2
CDKIs	Cyclin-dependent kinase inhibitors
CDKs	Cyclin-dependent kinases
cDNA	Complementary DNA
cm	centimeter
CHEK1	Checkpoint kinase 1
DAD	Delayed afterdepolarization
DMSO	Dimethyl sulfoxide
DSI	Data sciences international
EAD	Early afterdepolarizations
ECG	Electrocardiogram
EF	Ejection fraction
EP	Electrophysiology
ERP	Effective refractory period
FHS	Framingham heart study
GPR132	G protein-coupled receptor 132
GWAS	Genome-wide association study
Hif-α	Hypoxia-inducible factor-α
HIRA	Histone cell cycle regulator
Hoxb13	Homeobox b13

HRV	Heart rate variability
HSCS	Hematopoietic stem cells
IVS	Interventricular septal thickness
LA	Left atrium
LV	Left ventricle
LVID	Left ventricular internal dimensions
LVPW	Left ventricular posterior wall thickness
MCM3	Minichromosome maintenance complex component 3
Meis1	Myeloid ecotrophic insertion site 1
ms	millisecond
MI	myocardial infarction
NSCLC	Non-small cell lung cancer
OCT	Optimal cutting temperature
PBS	Phosphate-buffered saline
PFA	Paraformaldehyde
PNS	Parasympathetic nervous system
qPCR	Quantitative polymerase chain reaction
RB	Retinoblastoma protein
RMSSD	Root mean square of successive RR interval differences
RV	Right ventricle
RT	Room Temperature
SDRR	Standard deviation of RR intervals
SNRT	Sinus node recovery Time
SNS	Sympathetic nervous system
TALE	Three amino acid loop extension
TBX20	T-box transcription factor 20
TP53	Tumor protein 53
VERP	Ventricular effective refractory period

1. Introduction

1.1 Atrial fibrillation (AF)

1.1.1 Clinical presentation of AF

AF, the most prevalent sustained arrhythmia (Lippi et al., 2021), arises from rapid and disorganized atrial electrical activity, leading to irregular and uncoordinated contractions (Feghaly et al., 2018).

The global prevalence and incidence of AF are on the rise (Kornej et al., 2020). The Framingham Heart Study (FHS) revealed a threefold rise in AF prevalence across five decades of observation (Schnabel et al., 2015). During 2010-2020, about 2.7 million United States individuals were diagnosed with AF (Kornej et al., 2020). Current epidemiological models project the AF burden in the United States population will affect an estimated 6 to 16 million individuals by 2050 (Miyasaka et al., 2006, Go et al., 2001). In Europe, during the period from 2010 to 2020, it has been observed that the occurrence of AF amounts to approximately 4.5 million cases (Escudero-Martinez et al., 2023). Projections made by researchers suggest that by the year 2050, the prevalence of AF in Europe is anticipated to increase to around 16-17 million cases (Kornej et al., 2020) (Figure 1). In Asia, it is projected that by the year 2050, the prevalence of AF will reach a minimum of 72 million individuals (Chiang et al., 2014).

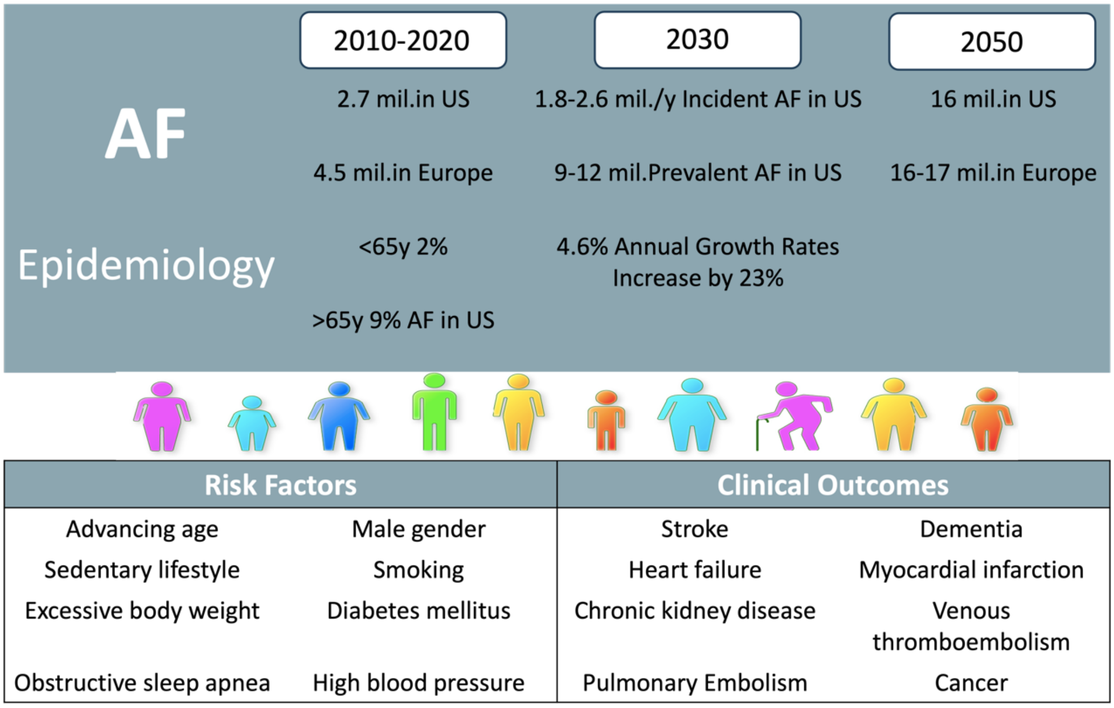

Risk Factors		Clinical Outcomes	
Advancing age	Male gender	Stroke	Dementia
Sedentary lifestyle	Smoking	Heart failure	Myocardial infarction
Excessive body weight	Diabetes mellitus	Chronic kidney disease	Venous thromboembolism
Obstructive sleep apnea	High blood pressure	Pulmonary Embolism	Cancer

Figure 1. AF epidemiology. AF epidemiology is cited and revised by Kornej *et al.*, 2020 (Kornej *et al.*, 2020). Advanced age emerges as the principal determinant of AF, while secondary risk factors comprise male gender, sedentary behavior, smoking, excessive adiposity, diabetic status, obstructive sleep apnea, and hypertensive disorders. AF significantly elevates the risk of multiple systemic complications, including heart failure, myocardial infarction (MI), chronic kidney disease, venous thromboembolism, stroke, and dementia.

The therapeutic approach for AF includes various interventions such as drug therapy, catheter ablation, device implantation, and treatment of comorbidities (Hjerteavdelingen, 2016). Although the therapeutic approaches for AF have significantly increased patient survival, current treatment remains ineffective in addressing the underlying proarrhythmic mechanisms in a subset of patients (Cosedis Nielsen et al., 2012, Mont et al., 2014) and side effects (Roskell et al., 2013). Thus, in order to enhance the existing treatment options, it is essential to develop novel therapies that optimally target the underlying causal proarrhythmic mechanisms.

1.1.2 Pathology of AF

The heart is a rhythmic electromechanical pump that relies on the generation and propagation of action potentials for its functioning (Nerbonne and Kass, 2005). The cardiac action potential is typically categorized into five separate phases: phase 0, phase 1, phase 2, phase 3, and phase 4 (Shih, 1994). Phase 0 is marked by a rapid upstroke, generated by the activation of voltage-gated Na^+ channels (Fozzard, 2002). Immediately after action potential upstroke, phase 1 follows with a transient repolarization caused by an outward potassium current (Nerbonne and Kass, 2005). Phase 2, known as the plateau phase, is characterized by a relatively stable membrane potential resulting from a balance between small, non-activated Na^+ currents and L-type Ca^{2+} currents, and outward hyperpolarizing K^+ currents (Santana et al., 2010). Phase 3 involves significant repolarization towards the diastolic potential, primarily due to increased potassium efflux and decreased calcium and sodium influx (András et al., 2021). Finally, phase 4, the resting state, is mainly driven by the potassium current, establishing the resting membrane potential (Grunnet et al., 2008). The five phases of a typical action potential are illustrated in Figure 2.

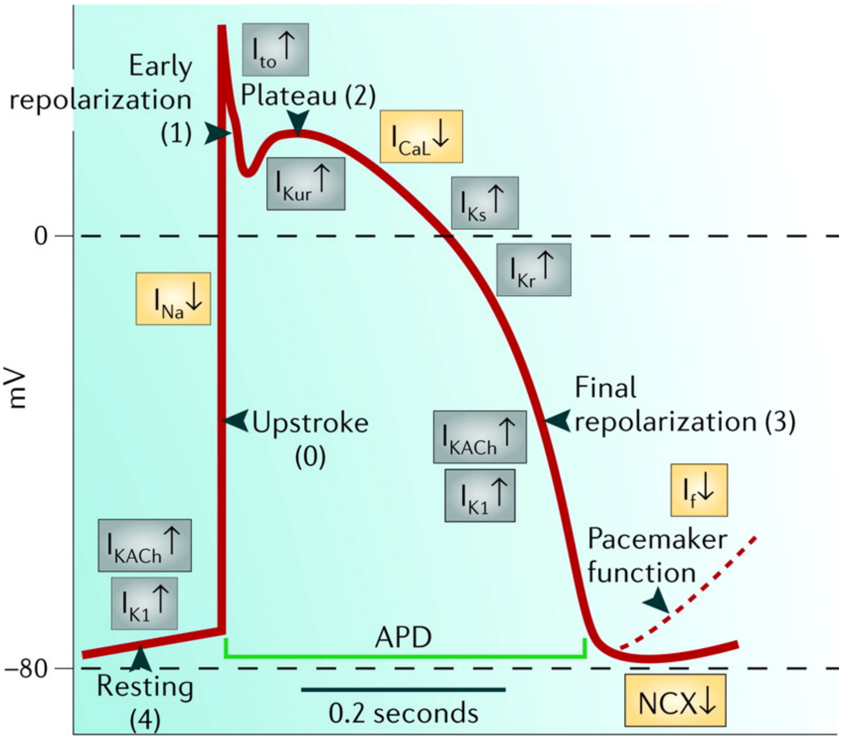

Figure 2. Membrane currents of a typical ventricular action potential. The action potential comprises of five unique phases: resting (phase 4), upstroke (phase 0), early repolarization (phase 1), plateau (phase 2), and final repolarization (phase 3). The inward currents, including sodium current (I_{Na}), calcium current (I_{Ca}), and pacemaker current (I_f). The action potential duration (APD) is around 200 milliseconds (ms) (Grant, 2009).

The mechanisms leading to AF can be categorized as electrical and structural remodeling (Schüttler et al., 2020). The principal mechanisms that generate AF include ectopic electrical activity and reentry (Wakili et al., 2011). Ectopic electrical activity commonly arises from early afterdepolarization (EAD) and delayed afterdepolarization (DAD), often originating from the pulmonary veins (Nattel et al., 2020). EAD arises during either phase 2 or 3 of the action potential repolarization, whereas DAD occurs at nearly or fully complete repolarization (Wit, 2018). When the magnitude of either afterdepolarization exceeds the threshold required to activate an inward current, it results in the generation of action potentials, which are referred to as ‘triggered activity’ (Wit and Boyden, 2007). Experimental studies have shown that EAD and DAD contribute to ectopic activity, which can trigger the onset of AF (Nattel et al., 2020).

Reentry is facilitated by short effective refractory periods (ERP) and slow impulse conduction (Heijman et al., 2014). The pathophysiology of AF reentry primarily involves three proposed mechanisms: rotor formation (Schuessler et al., 1992, Mandapati et al., 2000), multiple wavelet propagation (Moe and Abildskov, 1959), and epicardial-endocardial electrical uncoupling (Eckstein et al., 2011). Functional reentry creates a fixed or moving spiral, which drives AF (Staerk et al., 2017). ‘Multiple wavelet hypothesis’ stated that chaotic, fibrillatory conduction could occur if a sufficient amount of reentrant wavefronts were present in a suitable atrial substrate, repeatedly exciting the atria (Moe and Abildskov, 1959). The electrical dissociation of neighboring atrial bundles is pivotal in creating the AF substrate (Allessie et al., 2010), while ion channel remodeling represents a fundamental mechanism driving its initiation and maintenance (Gaborit et al., 2005). Modifications on ionic currents that prolong APD and the refractory period can help to suppress AF (Nattel et al., 2020). The reduction in the density of I_{Ca} is a key factor in the decrease of the ERP, which is a characteristic of AF at the functional level (Bosch et al., 1999). Furthermore, AF itself induces remodeling of ionic currents, which has a substantial impact on the pathophysiology of AF (Iwasaki et al., 2011). Bosch *et al*. found that AF in humans causes notable alterations in the potassium current and I_{Ca} in the atria, likely responsible for the decrease in APD and APD rate adaptation; these alterations contribute to the modification of electrical patterns in AF (Bosch et al., 1999). AF alters the electrical properties of the atria, creating a substrate that facilitates its recurrence. This self-perpetuating phenomenon, known as ‘AF begets AF’, involves both increasing the ability of AF to persist and making the atria more susceptible to AF induction by premature atrial beats (Allessie et al., 2010).

Atrial fibrosis, the hallmark of atrial structural remodeling (Pellman and Sheikh, 2015), results from dysregulated fibroblast activation and proliferation, causing excessive extracellular matrix (ECM) protein synthesis and disorganized deposition (Polyakova et al., 2008). These proteins serve as established AF substrates, contributing to both arrhythmia initiation and maintenance (Polyakova et al., 2008). Fibrosis contributes to AF pathogenesis through disruption of myocardial bundle continuity and regional conduction abnormalities (Nattel and Harada, 2014).

Elucidating these underlying mechanisms is essential for studying targeted therapies (Mason et al., 2020). The pathophysiologic basis of AF is complex and still incompletely understood (Nattel, 2002, Wakili et al., 2011); hence, further exploration is required.

1.2 Myeloid ecotropic insertion site 1 (Meis1)

1.2.1 The general role of Meis1

As members of the three amino acid loop extension (TALE) homeodomain transcription factor family (Turan et al., 2020), the Meis protein group (Meis1-3) includes Meis1, initially discovered as a frequent viral integration locus in spontaneous leukemogenesis using BXH-2 murine models (Moskow et al., 1995).

Meis1 has been characterized as a pleiotropic regulator across multiple biological systems, with demonstrated functions in embryogenesis, stem cell maintenance, and oncogenic transformation (Jiang et al., 2021). Meis1 was discovered to maintain hematopoietic stem cells (HSCS) in a Meis1 knockout mouse model by limiting oxidative metabolism (Unnisa et al., 2012). Meis1 was found to be a site of viral integration in 15% of tumors in BXH-2 mice, suggesting its potential involvement in myeloid leukemia in this mouse strain (Moskow et al., 1995). Meis1 exhibits elevated expression in numerous neuroblastoma cell types and contributes to neuroblastoma development by inhibiting cell differentiation and proliferation (Geerts et al., 2003). Okumura *et al*. found that disrupting Meis1 function in K14^{CreER}-Meis1$^{fl/fl}$ mice by tamoxifen induction results in a reduction of quiescent stem cells and a rise in differentiation into epidermal cells (Okumura et al., 2014). This indicates that Meis1 is essential for regulating epidermal balance in healthy tissues. Conversely, emerging evidence indicated that Meis1 exhibits tumor-suppressive activity in other cancers, such as non-small cell lung cancer

(NSCLC) (Li et al., 2014) and prostate carcinoma (VanOpstall et al., 2020). For example, Li *et al*. observed that reducing Meis1 expression resulted in enhanced proliferation of cells in two NSCLC cell lines, A549 and SPC-A1; conversely, they also discovered that elevated Meis1 in A549 cells can suppress the proliferation of NSCLC (Li et al., 2014). Moreover, Meis1 expression reduces the expansion and migration of prostate tumor cells in CWR22Rv1 and LAPC4 cells (VanOpstall et al., 2020).

An increasing amount of data suggested that Meis1 is associated with the PR interval in the electrocardiogram (ECG) (Van Setten et al., 2018, Sano et al., 2014, Verweij et al., 2014). A meta-analysis of Genome-wide association studies (GWAS) utilizing the data from seven population-based European studies revealed a significant association between a variant located on chromosome 2 within the Meis1 gene and the PR interval (Pfeufer et al., 2010). An analysis of the GWAS involving more than 92,000 individuals of European descent revealed that Meis1 was linked to atrial and atrioventricular (AV) electrical activity (Van Setten et al., 2018). Numerous genomic association studies revealed a correlation between the Meis1 gene mutation and an abnormal PR interval in patients (Smith et al., 2011). The observations indicate a possible function of Meis1 as a genetic determinant in atrial EP.

1.2.2 The role of Meis1 on the cardiomyocyte cell cycle

The cell cycle represents a precisely regulated sequence of molecular events that guarantees accurate genomic replication and equitable distribution of genetic material to daughter cells (Israels and Israels, 2000). The cell cycle comprises four phases: G1, S, G2, and M (Johnson and Walker, 1999). G1, also known as gap 1, is the interval between mitotic division (M phase) and DNA replication (S phase) (Schafer, 1998). The G1-to-S transition is potentiated by mitogen-dependent signaling, culminating in the molecular preparations necessary for chromosomal DNA replication (Israels and Israels, 2000). The G2 phase represents a critical cell cycle checkpoint period separating chromosomal replication completion in S phase from mitotic initiation (Tyson et al., 2002). Meis1 is recognized as an important controller of the cardiomyocyte cell cycle in a mouse model with cardiomyocyte-specific Meis1 knockout (Mahmoud et al., 2013). Meis1 modulates cardiomyocyte cell cycle capture by transcriptionally activating cyclin-dependent kinase inhibitors (CDKIs), such as p15, p16, and p21 (Mahmoud et al., 2013). By targeting cyclin-dependent kinases (CDKs), including CDK2 and CDK4/6, CDKIs trigger cell cycle arrest (Mahmoud et al., 2013). CDKIs can be divided into two subclasses: the Ink4 family (p15Ink4b, p16Ink4a, p18Ink4c, and p19Ink4d), which blocks the assembly of CDK complexes, and the Cip/Kip family (p21Cip1, p27Kip1, and p57Kip2), which specifically disables the kinase activity of pre-formed cyclin/CDK complexes (Shankland and Wolf, 2000). Furthermore, in cardiomyocytes, T-box transcription factor 20 (TBX20) was shown to directly interact with Meis1, resulting in the suppression of Meis1 and CDK1 (Figure 3) (Jiang et al., 2021). Deletion of Meis1 increases the expression of certain cell cycle promotors like checkpoint kinase 1 (CHEK1), minichromosome maintenance complex component 3 (MCM3), and Cyclin D2 (CCND2) while decreasing the levels of cell cycle inhibitors such as amyloid beta precursor protein-binding family B member1 (Apbb1), tumor protein 53 (TP53) and G protein-coupled receptor 132 (GPR132), among others, all of which may influence the effects of Meis1 deletion on the cell process (Jiang et al., 2021) (Mahmoud et al., 2013) (Figure 3). Excessive expression of Meis1 restricted the proliferation of cardiomyocytes and inhibited the renewal of hearts in newborn mice after MI (Mahmoud et al., 2013). This implies that Meis1 plays a crucial role in inducing cell cycle arrest in the myocardium after birth. Numerous miRNAs display stage-specific expression patterns, functioning as molecular regulators that modulate developmental processes including cardiogenesis (Williams et al., 2009). In-silico analysis and luciferase assays demonstrated that miR-548c-3p, miR-509-3p, and miR-23b-3p significantly promote proliferation in rat ventricular cardiomyocytes by inhibiting the translation of Meis1 through specific binding to regions of the 3’UTR that encode the Meis1 gene (Pandey et al., 2016) (Figure 3).

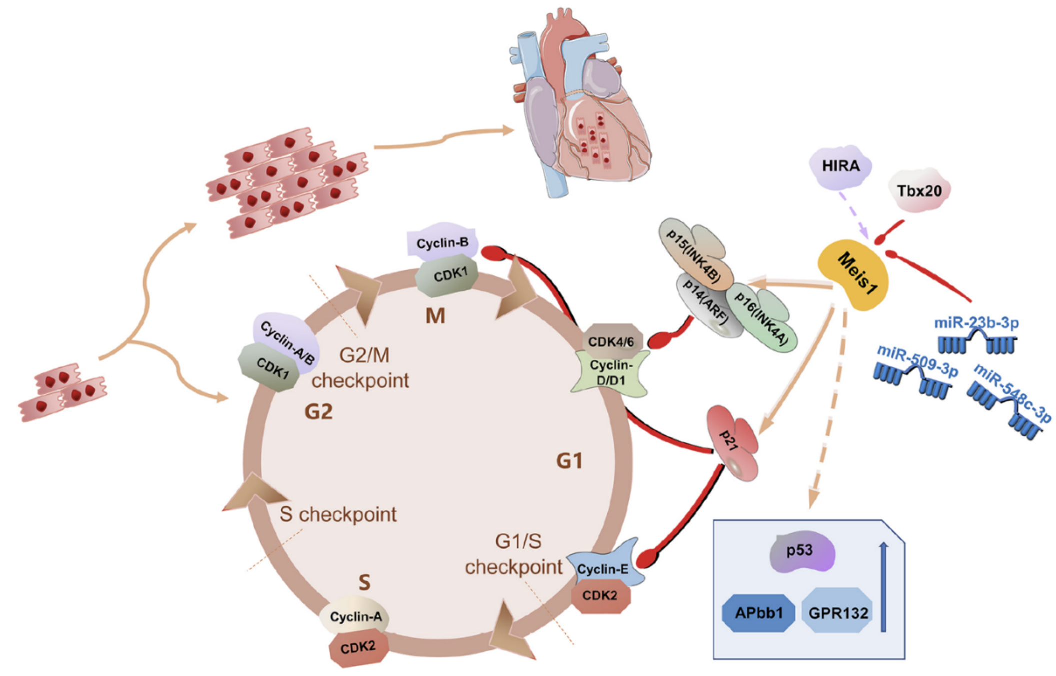

Figure 3. The function of Meis1 in cardiomyocytes cell cycle. Meis1 is a critical regulator of cardiomyocyte cell cycle progression (Jiang et al., 2021). Acting upstream of two synergistic cyclin-dependent kinase inhibitors (CDKIs), its deletion upregulates pro-proliferative factors (CHEK1, CCND2) while suppressing negative regulators (Apbb1, TP53, GPR132). Modulating Meis1 activity-along with associated factors such as HIRA, TBX20, and specific miRNAs-offers a potential strategy to enhance or restrict cardiomyocyte proliferation.

1.2.3 The role of Meis1 on arrhythmias

Meis1 promotes vascularization of ischemic heart tissue and prevents angiotensin II-induced myocardial hypertrophy by increasing the production of Poly (rC)-binding protein 2 (Zhang et al., 2016). Bouilloux *et al*. demonstrated that Meis1 deficiency elevates sudden cardiac death risk by impairing sympathetic neuron target innervation (Bouilloux et al., 2016). The function of Meis1 in the progression of ischemic ventricular fibrillation in C57BL/6 mice with MI was investigated by Liu *et al*. The research indicated that the overexpression of Meis1 in mice with MI leads to a reduction in the occurrence and duration of ventricular fibrillation when compared to control mice, suggesting that Meis1 may represent an exciting new target for the management of arrhythmias following MI (Liu et al., 2022). However, the role of Meis1 in atrial EP and arrhythmogenesis is unknown.

1.3 Hypothesis and objectives

The hypothesis of the project is that Meis1 has an essential function in atrial EP and arrhythmogenesis by regulating the cell cycle in cardiac cells. To test this hypothesis the following four research objectives will be addressed:

1) Cardiac structure and function will be studied in mice treated with a Meis1 inhibitor.
2) Atrial EP and arrhythmogenesis will be examined in mice with and without Meis1 inhibition.
3) The expression of Meis1 target genes will be investigated in heart tissue obtained from Meis1 inhibitor-treated mice.
4) The impact of Meis1 inhibition on cell proliferation within the right atrium (RA) will be studied by immunofluorescence.

2. Materials and methods

2.1 Ethics statement

All animal experiments were conducted in compliance with the University of Munich Animal Care and Ethics Committee guidelines. Additionally, the Government of Upper Bavaria, Germany, granted approval for all mouse experiments (ROB-55.2-2532.Vet_02-16-106).

2.2 Materials

Table 1. Antibodies

Antibody	Type	Host	Application/ Dilution	Manufacturer/Reference
Anti-Ki67	Primary	Rat	IF/1:200	Invitrogen, Waltham, Massachusetts, U.S/14-5698-82
Anti-Desmin	Primary	Rabbit	IF/1:500	Cell signaling, Leiden, Netherland/5332S
Anti-CD64	Primary	Rabbit	IF/1:100	SinoBiological, Eschborn, Germany/50086-R027
Anti-Vimentin	Primary	Chicken	IF/1:300	Thermo Fisher，Bleiswijk, Netherlands/PA1-10003
Anti-rabbit-IgG AF488	Secondary	Rabbit	IF/1:1000	Cell signaling, Leiden, Netherland /4412s

Anti-rat-IgG AF647	Secondary	Rat	IF/1:1000	Thermo Fisher, Bleiswijk, Netherlands/ Lot: 2268323
Anti-chicken-IgY AF555	Secondary	Chicken	IF/1:1000	Thermo Fisher, Bleiswijk, Netherlands / Lot: WD322211
Anti-rabbit-IgG AF568	Secondary	Rabbit	IF/1:1000	ThermoFisher, Bleiswijk, Netherlands/ Lot: 2155282

Table 2. Chemicals and reagents

Chemical or reagent	Manufacturer/Reference
TRIzol	Thermo Fisher, Bleiswijk, Netherlands/15596018
Chloroform ≥ 99%	Sigma-Aldrich, Taufkrichen, Germany/288306
Emprove essential 2-Propanol	Merck Millipore, Darmstadt, Germany/1.00995.1000
99.9% Ethanol	Merck Millipore, Darmstadt, Germany/1.00986.1000
50 µM random hexamers	Thermo Fisher, Bleiswijk, Netherlands/N8080127
10 mM dNTP mix, PCR grade	Thermo Fisher, Bleiswijk, Netherlands/18427089
Nuclease-free water 50 mL	Qiagen, Hilden, Germany/129114
SuperScript IV Reverse Transcriptase	Thermo Fisher, Bleiswijk, Netherlands/18090010
iTaq Universal SYBR Green Supermix	BIO-RAD, Hercules, California, U.S/1725124

Biozym LE Agarose Universalagarose	Biozym, Hessisch Oldendorf, Germany/840004
Triton X-100	Sigma-Aldrich, Taufkrichen, Germany/T8787
TWEEN-20	Sigma-Aldrich, Taufkrichen, Germany/P2287
Bovine serum albumin	Sigma-Aldrich, Taufkrichen, Germany/A2153
Non-sterile goat serum	Abcam, Cambridge, UK/ab7481
Phosphate-buffered saline (10X) (PBS)	Sigma-Aldrich, Taufkrichen, Germany/D1408
Phosphate-buffered saline (1X)	Gibco, Bleiswijk, Netherlands/14190-094
SYBR™ Safe DNA Gel Stain	Thermo Fisher, Bleiswijk, Netherlands/S33102
Tris base	Carl Roth, Karlsruhe, Germany/4855.2
EDTA disodium salt dihydrate	Carl Roth, Karlsruhe, Germany /8043.2
Dimethyl sulfoxide (DMSO)	Sigma-Aldrich, Taufkrichen, Germany/589569
Methanol free 16% paraformaldehyde (PFA)	Thermo Fisher, Bleiswijk, Netherlands/28906
Hoechst 33342	Thermo Fisher, Bleiswijk, Netherlands/H1399
Fluorescence Mounting Medium	Agilent Dako, Santa Clara, California/S3023
Sucrose	Sigma-Aldrich, Taufkrichen, Germany/S1888
Fentanyl 0.5 mg/10 mL	B.Braun, Hesse, Germany
Carprofen 0.005 mg/µL	Zoetis, Louvain-la-Neuve, Belgium/53716-49-7
Ophthalmic ointment	Ubuy, Berlin, Germany/1578675

Meis1 inhibitor	Meinox Pharma Technologies, Sariyer, Istanbul/2250156-71-7

Table 3. Solutions and buffers

TBE buffer (10X), PH 8.3		Final concentration
Tris base	54.5 g	450 mM
EDTA	2.9 g	10 mM
Boric acid	27.8 g	450 mM
Distilled water	To 1000 ml	
Washing buffer for immunofluorescence staining		5%
BSA	5 g	
Tween 20	1 mL	
1xPBS	1000 mL	
Blocking buffer		10%
Washing buffer	9 mL	
Goat serum	1 mL	
methanol free Formaldehyde solution		4%
16 % methanol free PFA	10 mL	
1x PBS	30 mL	
Triton$^{\text{TM}}$ x-100		0.5%
100% Triton$^{\text{TM}}$ x-100	200 µL	
1x PBS	40 mL	
sucrose		30%
Sucrose powder	30 g	
1x PBS	100 mL	

Table 4. Consumables and Instruments

Material	Manufacturer
PCR reaction tube	Corning, Darmstadt, Germany /CLS6531
Pipette tips (10 µl, 200 µl, 1000 µl)	Eppendorf, Darmstadt, Germany /Z683884-1EA
Serological pipettes, sterile (10 ml, 25 ml)	Corning, Darmstadt, Germany /CLS707810N
Cover slips (24x50 mm, #1.5)	Thermo Fisher, Bleiswijk, Netherlands /NC 1034527
Pasteur pipette	VWR, Gliwice, Poland/612-1681
Falcon™ Conical Tubes (15 ml, 50 ml)	Thermo Fisher, Bleiswijk, Netherlands /339650, 339652
Cryovial tube (2 ml)	Simport scientific, Beloeil, Quebec, Canada/T310-2A
Syringe (1 ml, 5 ml, 10 ml)	B. Braun Omnifix Solo, Hesse, Germany/2050-1
27 G needle	B. Braun Melsungen, Hesse, Germany/4657705
Spring scissors	Fine Science Tools, Heidelberg, Germany/91500-09
Iris scissors	Fine Science Tools, Heidelberg, Germany/14084-08
Curved forceps	Fine Science Tools, Heidelberg, Germany/91117-10
Fine forceps	Fine Science Tools, Heidelberg, Germany/11295-51
Real-time PCR 96-well plates	Eppendorf, Darmstadt, Germany/K196321K

Table 5. Equipment and software

Equipment	Software
Three ECG needle electrodes	AD Instruments, 29G, Oxford, United Kingdom
PowerLab data acquisition device	AD Instruments, Oxford, United Kingdom/PL 3508
Animal Bio Amp	AD Instruments, Oxford, United Kingdom/FE231
Ultrasound Vevo® 2100	Fujifilm Visual Sonics, Toronto, Canada
Analytical balance	Merck Millipore, Taufkirchen, Germany/OH30430053
Centrifuge 5430R	Eppendorf, Hamburg, Germany/EP022620511
Centrifuge 5418R	Eppendorf, Hamburg, Germany/EP5401000137
NanoDrop 2000	Thermo Fisher, Dreieich, Germany/ ND2000
C1000 Touch Thermal Cycler	Bio-Rad, Feldkirchen, Germnay/1851196
CFX96 Touch Real-Time PCR Detection System with CFX manger	BioRad, Feldkirchen, Germnay/1845097
Cryotome	CryoStar NX70, Lecia/957030L
Leica Fluorescence microscopy	DM6 B, Leica Microsystems, Wetzlar, Germany/MC-0000781
Vortex mixer	Neolab, Heidelberg, Germany
EndNote 20	Thomson Reuters, New York, USA
GraphPad Prism 8.0	GraphPad Software, Inc., La Jolla, USA
Image J	By Wayne Rasband, NIH, Bethseda, USA
Ponemah	Data Sciences International, Saint Paul, Minnesota, USA

Labchart Pro 8.0	AD Instruments, Oxford, United Kingdom
EPR-800 octapolar catheter	Millar Instruments/840-8145
ETA-F10 transmitter	Data Sciences International, Saint Paul, Minnesota, USA

2.3 Methods

2.3.1 Preparation of the 100 µM Meis1 inhibitor solution

Small-molecular Meis1 inhibitor was kindly provided by Prof. Fatih Kocabas from Yeditepe University. A 10 mM Meis1 inhibitor stock solution was prepared in Dimethyl sulfoxide. The stock solution was diluted with PBS (pH 9.05) to a final working concentration of 100 µM. The working concentration was determined based on the designer's recommendation and preliminary data. Its in vivo efficacy was demonstrated through increased bone marrow HSC content and downregulation of Meis1 target genes (Turan et al., 2020). The solution was prepared on the same day as starting the experiments. The working solution was filtered before injection.

2.3.2 Application of the Meis1 inhibitor *in vivo*

Male BALB/c mice aged 3 months were bought from Charles River. Meis1 inhibitor (Molecular weight: 306.32) was intraperitoneally injected into BALB/c mice on days 1, 4, and 7. At day 10, baseline ECG, echocardiography, invasive EP studies, quantitative real-time polymerase chain reaction (qPCR), and Immunofluorescence staining were performed. Saline-injected mice served as controls. Meis1-i indicated the Meis1 inhibitor-treated mice.

2.3.3 Echocardiography

Left ventricular dimensions, systolic function, and left atrial diameter were assessed in anesthetized mice using a high-resolution ultrasound system with 60-Hz transducer (Ultrasound Vevo® 2100, Fujifilm Visual Sonics). The study design is presented in Figure 4.

Anesthesia was induced by placing the mouse in a vaporizer-connected chamber delivering 2.5% isoflurane (1 L/min flow rate). 100% oxygen was given through the vaporizer. The mouse was positioned supine on a heated operating pad once it had reached full anesthesia. The nose of the mouse was immediately covered with an isoflurane inhalation mask. The limbs of the mouse were affixed onto the metal ECG pad. Hair removal on the chest area of the mouse was done using depilatory cream. Body temperature was maintained at 37°C during surgery via continuous rectal thermometry. The complete anesthesia of mice was verified using the pinching method. The transducer was coated with Echo gel. Long-axis (Figure 5A) and short-axis (Figure 5B) left ventricle (LV) images were acquired through transducer repositioning, as depicted in Figure 5. To assess the structure of the LV, various dimensions in the long-axis, including the interventricular septal thickness (IVS), left ventricular internal dimensions (LVID), and posterior wall thickness (PW), were quantified through both diastole and systole. All dimensional analyses were performed using M-mode tracings acquired at the papillary muscle plane. The assessment of the systolic function of the LV was conducted through the estimation of the LV ejection fraction (EF) (Tanaka et al., 1996). EF was determined by assessing end-diastolic and end-systolic LV dimensions via M-mode echocardiography. EF was calculated with the formula: EF (%) = 100 × $(LVIDd^3 - LVIDs^3)/LVIDd^3$ x 100. Following imaging, residual Echo gel was gently removed and mice were returned to their cages for recovery. Each parameter was measured over at least three heartbeats prior to calculating the average of these measurements.

Figure 4. Experimental design. Saline or Meis1 inhibitor was injected in mice on days 1, 4, and 7. Echocardiography, ECG, and EP study were performed on day 10.

Figure 5. Schematic diagram for echocardiography. The schematic diagram for echocardiography in the parasternal short and long axis. (A) Long-axis and (B) short-axis LV imaging planes, with transducer positions indicated by arrows. Created with BioRender.com

2.3.4 Baseline surface ECG

To evaluate the overall cardiac conduction properties, the baseline surface ECG was recorded in anesthesized mice 10 days after Meis1 inhibition. Figure 6 illustrates the experimental design. To start the experiment, the mouse was first weighed. The mouse was anesthetized in the induction chamber. The mouse was quickly transferred to a warmed operation pad and positioned in a supine orientation. The anesthesia conditions applied were consistent with those used for the Echocardiography. A lead-I ECG configuration was established by subcutaneous insertion of electrodes in both forelimbs and right hindlimb (Figure 6). Five-minute recordings with a good signal were selected following full narcosis for analysis. LabChart software quantified key ECG metrics including, including heart rate, P wave duration, PR interval, QRS duration, and QT interval.

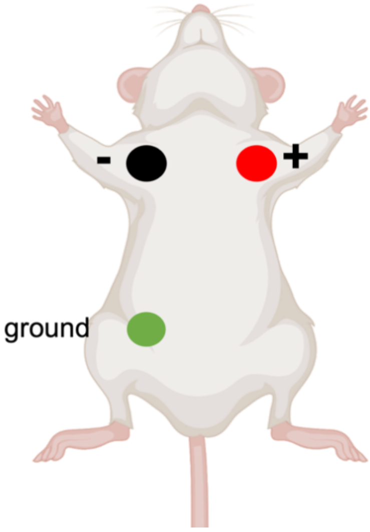

Figure 6. illustration of lead I ECG configuration for surface ECG. Illustration of lead I ECG configuration for surface ECG. The negative electrode (-) is shown in black, the positive electrode (+) is shown in red, and the ground electrode is shown in green. Created with BioRender.com.

2.3.5 Invasive EP study

2.3.5.1 Jugular vein preparation

An EP study was conducted to assess the conduction features of the sinus node, atrioventricular node (AVN), atrium, and ventricle in detail and to assess arrhythmia inducibility. Figure 4 illustrates the experimental design. The surgery was carried out in a sterile condition. First, the mouse was weighed. Then, anesthesia was induced with 2.5% isoflurane at 1 L/min through a vaporizer-coupled induction chamber. The mouse was properly positioned supine on a heated operating pad once it had reached full anesthesia. The nose of the mouse was immediately covered with an isoflurane inhalation mask. The limbs of the mouse were affixed to the surgical mat. Eye ointment was applied to the mouse to reduce the eye dryness. Body heat was sustained at 37°C while surgery via continuous rectal thermometry. To induce analgesia, mice were intraperitoneally injected with Fentanyl and Carprofen at a concentration of 0.50 µg/g. The toe-pinch method was used to verify the complete anesthesia of the mouse, and after the absence of reflexes and the recovery of normal breathing, surgery was started.

2.3.5.2 EP Catheterization in the RA and right ventricle (RV)

Three-lead ECG monitoring was established via subcutaneous electrodes placed in bilateral forelimbs and right hindlimb. Surgical exposure was achieved through a 0.5 cm longitudinal incision positioned 2-3 mm right of midline, created using sequential blunt dissection and sharp tissue transection. An incision was made in the skin, extending caudally to the transverse pectoralis muscle from the submandibular region. The blunt forceps were used to lift the skin and the non-sharp edges of the scissors were used to completely separate it from the underlying tissue. The closed scissors were inserted into the subcutaneous tissue, then they were opened, and the branches were pulled back to form a subcutaneous pocket. Incision length was increased by approximately 1 centimeter (cm). The angled forceps were used to remove the surrounding muscle and fat tissue in a blunt dissection manner, exposing the right jugular vein. A little incision was created along the longitudinal axis of the vein using micro scissors, followed by the insertion of a EP catheter, which was directed towards the RA and RV (Figure 7). The positioning was appropriate when the proximal electrodes displayed a ventricular signal, while the distal electrodes displayed an atrial signal (Tomsits et al., 2023). The vein was ligated proximally with suture. Continuous gentle traction maintained jugular vein alignment during catheter insertion. The vein was ligated distally using supplementary suture. After confirming proper intracardiac placement, the distal ligature was tightened. Li *et al.* have demonstrated that this method effectively minimizes blood loss and ensures accurate placement of the catheter in the proper anatomical location (Li and Wehrens, 2010).

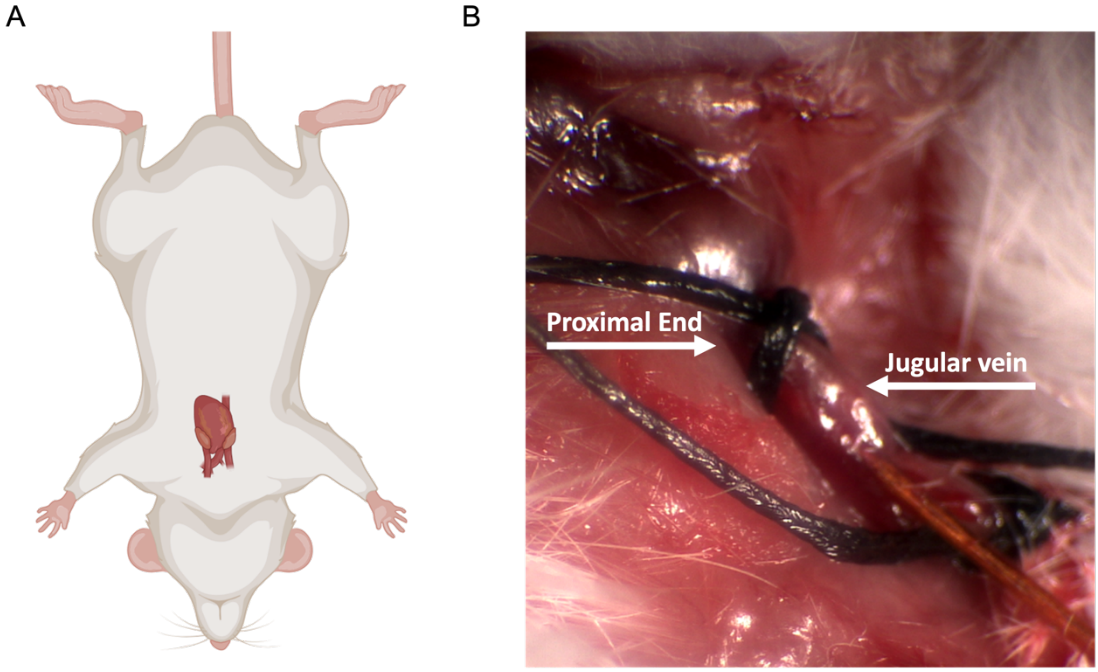

Figure 7. Visualization of the catheter insertion. Visualization of the catheter insertion. (A) The mouse was put in a supine position during the surgery. (B) The catheter was placed into the jugular vein, with the proximal end indicated by the white arrow. Created with BioRender.com.

2.3.5.3 Stimulation protocol

The sinus node's electrophysiological performance was assessed by calculating the sinus node recovery time (SNRT) following 30-second pacing durations at progressively shorter intervals (120, 100, 80 ms) (Hulsmans et al., 2017). SNRT was measured from the last pacing stimulus to the onset of the first intrinsic sinus P wave (Li and Wehrens, 2010). The SNRT was corrected by dividing by the corresponding basic cycle. Starting at 120 ms, the atrial pacing cycle length was decremented by 10 ms until failure of one-to-one AV conduction, defining the Wenckebach point (Cepiel et al., 2017). Following the same methodology, the cycle length producing two-to-one conduction was determined. The ERP of the atrium, AV node, and ventricle was assessed using the S1-S2 stimulation procedure. This treatment involved pacing the atria and ventricles with a sequence of seven fixed stimuli (S1) in basic cycle periods of 120 ms and 100 ms, followed by an additional, premature, eighth stimulus (S2) that was detrimentally coupled. The atrial effective refractory period (AERP) was defined as the longest S2 coupling interval failing to produce a P wave, while AV effective refractory period (AVERP) represented the maximal S2 delay failing to conduct to the ventricles (Pauly et al., 2023). The ventricular effective refractory period (VERP) represented the maximal coupling interval (S1-S2) at which the extrastimulus failed to capture the ventricle (Nasi - Er et al., 2019). The length of the retrograde (VA) conduction was measured by gradually decreasing the rate of ventricular pacing.

Atrial arrhythmia induction was accomplished through S1S2S3 train stimulation and burst pacing (3 seconds and 6 seconds). The S1S2S3 protocol employed S1 baseline cycles of 120 ms and 100 ms, with S2 and S3 extrastimuli delivered at decreasing intervals from 40 ms to 20 ms in 5 ms decrements. Burst pacing consisted of 3-second and 6-second trains at progressively faster rates starting from 60 ms down to 10 ms cycle lengths in 5 ms steps. The atrial arrhythmias were defined by high-frequency polymorphic atrial excitation, regular or irregular ventricular conduction, changes in the basic atrial cycle length after stimulation, or alterations in atrial signal morphology that suggest an ectopic origin. Only arrhythmia episodes longer than 1 second were considered for further evaluation (Tomsits et al., 2023). The inducibility of atrial arrhythmias was evaluated by determining the percentage of mice that could be induced with atrial arrhythmias. In addition, the arrhythmia inducibility was also evaluated by determining the percentage of successful stimulations that resulted in atrial arrhythmias. Further, the average atrial arrhythmia burden representing the average duration of all respective episodes in an entire group was also calculated.

2.3.6 Ambulatory ECG Telemetry

To study the impact of Meis1 inhibition on ECG parameters, time-domain and frequency-domain heart rate variability (HRV) and spontaneous arrhythmia occurrence, ambulatory ECG telemetry was performed in conscious mice. Telemetry transmitters were intraperitoneally implanted. Following the implantation, there was a 7-day period for acclimatization. The saline or Meis1 inhibitor was administered on days 1, 4, and 7. Telemetry ECG recordings were conducted continuously until day 30. The study design is shown in Figure 8.

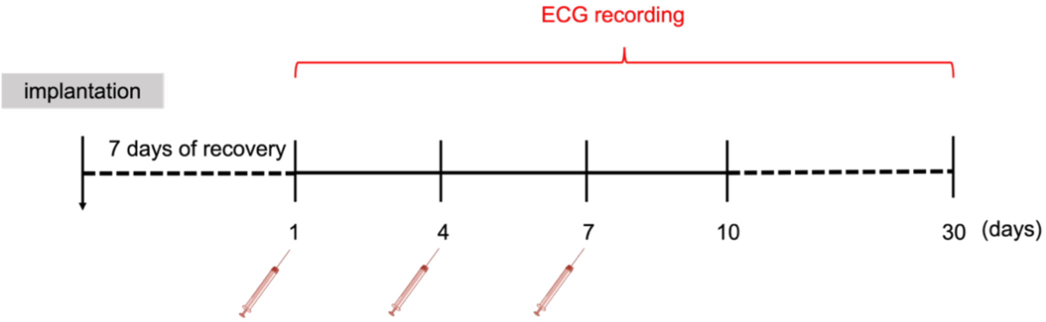

Figure 8. Experimental design. After the transmitter implantation, a 7-day recovery period was observed to ensure complete recovery of the mouse. The saline or Meis1 inhibitor was administered on days 1, 4, and 7. Telemetry ECG recordings were conducted continuously until day 30.

2.3.6.1 Transmitter preparation

The ETA-F10 transmitter manufactured by Data sciences international (DSI) was used. The transmitter consists of a negative lead and a positive lead of approximately 10 cm in length (Figure 9). The leads of the transmitter were cut to the proper length before implanting. The positive lead (red) is approximately 2.5 cm long, while the negative lead (white) is approximately 3.5 cm long. A small section of the insulation sheath was removed from the electrode tips to expose the 5-7 mm conduction wire. The transmitter was brought into proximity with the supplied magnet to activate. The radio device was used to identify the transmitter signal at 530 Hz frequency when it is turned on.

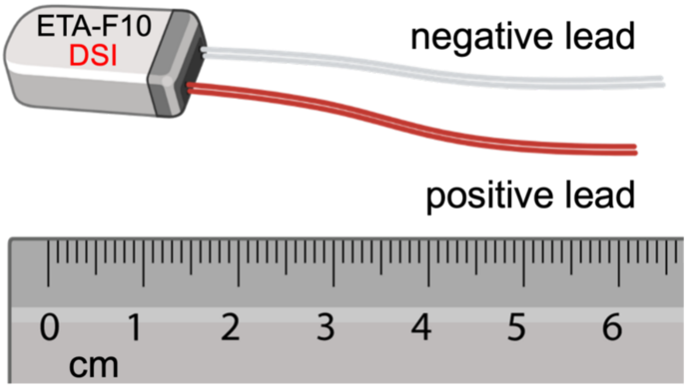

Figure 9. ETA-F10 transmitter. ETA-F10 transmitter with positive (red) and negative (white) leads. Created with BioRender.com.

2.3.6.2 Transmitter implantation

The mouse was weighed prior to the surgery. The initial body weight served as a reference for assessing the recovery of mice after surgery. The operating table and all surgical instruments were sterilized to preserve aseptic conditions during the surgery. Fentanyl and Carprofen at doses of 0.5 µg/g were injected intraperitoneally into the anesthetized mice to produce analgesia. The anesthesia procedure and analgesic injection in mice were consistent with the EP study described previously. Telemetry implantation was achieved as described by Tomsits *et al* (Tomsits et al., 2022). Depilatory cream was used to remove hair from the abdomen’s chest area, and chlorhexidine was applied to disinfect the surgical area. A 2 cm ventral midline abdominal incision was created, followed by blunt dissection of skin from underlying tissues. Electrode leads were implanted in subcutaneous pockets at the lower left and upper right chest position (Tomsits et al., 2022). To establish the lead II configuration, the negative electrode was positioned in the upper-right pocket, while the positive lead was placed in the lower-left pocket (Figure 10). The transmitter was inserted into the peritoneum superior to the intestine. A 14-gauge syringe was utilized to penetrate the subcutaneous tissue in the upper-right and lower-left regions of the chest to facilitate electrode placement. The red and white electrodes were directed through the syringe to establish a lead II arrangement. The positive (red) and negative (white) electrodes were secured in the lower-left and upper-right chest regions, respectively, with 6.0 sutures. The 7.0 sutures were used to properly close all incisions and apply disinfectant to the wounds. After the operation, the mouse was transferred to the cage and put in a place where it could receive heat to maintain its body temperature until it completely recovered from anesthesia.

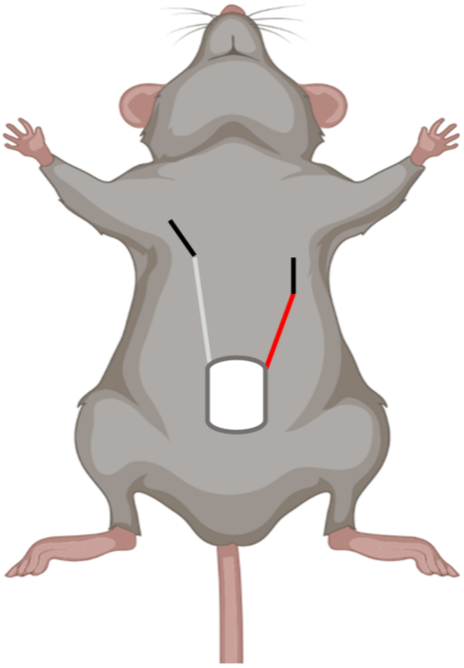

Figure 10. Schematic illustration of implanting the transmitter. To establish the lead II configuration, the negative (white) and positive (red) leads were implanted in the upper-right and lower-left pockets, respectively (Modified according to Tomsits *et al.*, 2022). Created with BioRender.com

2.3.6.3 Data acquisition

The mouse cage was positioned on the signal receiver. A connection was established between the signal collector and the data gathering system. A connection was established between the acquisition equipment and a computer containing software capable of visualizing the data. The process of collecting and recording telemetry data was started. The telemetry system used in the study is shown in Figure 11.

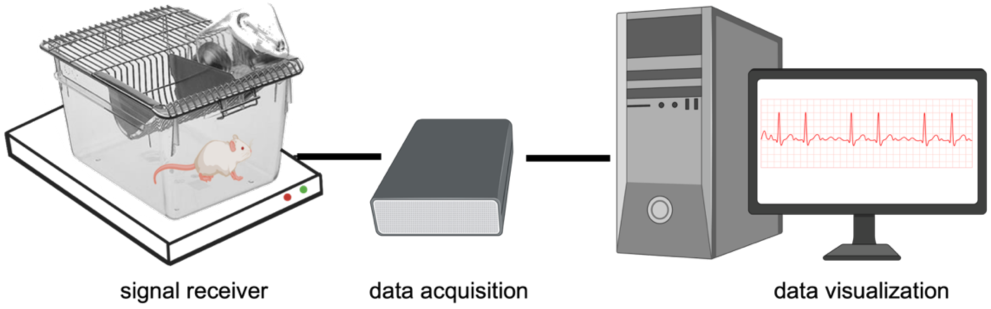

Figure 11. Telemetry set up. A mouse cage was placed on the signal collector. Signal collector and the data gathering system were connected. A computer containing data visualization software connected to the acquisition system (Modified according to Tomsits *et al*., 2022). Created with BioRender.com.

2.3.6.4 ECG parameters analysis

The data analysis was conducted with Ponemah software. The ECG parameters, including heart rate, P wave duration, PR interval, QRS duration, and QT interval, were assessed in conscious mice at three time points: baseline, day 10, and day 30. Because mice have a circadian rhythm (Li et al., 1999), a 15-minute ECG recording was analyzed during the day (from 9:00 to 15:00) and night (from 20:00 to 03:00).

2.3.6.5 HRV analysis

Daytime and nighttime 3-minute ECG segments with clear signal quality were analyzed for time- and frequency-domain HRV parameters using Ponemah. The time domain parameters included the RR intervals, the standard deviation of RR intervals (SDRR), and the root mean square of successive RR interval differences (RMSSD). In the frequency domain analysis, various parameters were examined, such as the very low-frequency power (0–0.4 Hz), the low-frequency power (0.4–1.5 Hz), and the high-frequency power (1.5–4.0 Hz) (Shaffer and Ginsberg, 2017).

2.3.6.6 Spontaneous arrhythmias analysis

Ponemah software was used to analyze spontaneous arrhythmias, including sinus pause, AV block, bradycardia, and tachycardia. Sinus pauses and AV block which lasted longer than one second were analyzed. According to Kaese *et al.*, the normal heart rate in mice spans 500-724 bpm, corresponding to cycle lengths of 82-120 ms (Kaese and Verheule, 2012). Bradycardia was defined as twenty or more subsequent RR intervals exceeding 120 ms, while tachycardia required twenty or more successive RR intervals below 82 ms (Tomsits et al., 2022). A sinus pause was characterized by the absence of the P wave (Da Costa et al., 2002). AV block implies a delay or disruption in AV impulse conduction (Kashou et al., 2017). Sinus pause and AV block incidence was expressed as the percentage of mice per group demonstrating these events. The overall incidence of tachycardia and bradycardia was determined by calculating the average number of tachycardia or bradycardia events in each mouse over a period of 30 days.

2.4 Gene expression detection

2.4.1 RNA isolation

Following the termination of the mouse, the heart of the mouse was subjected to perfusion using cold PBS. The heart was removed and dissected into the RA, the RV, the left atrium (LA), and the LV. The collected tissue was immediately placed in liquid nitrogen and rapidly frozen. The sample was preserved at -80°C freezer until its next use. To achieve homogenization, frozen tissue was cut into pieces with a mortar and pestle while immersed in liquid nitrogen. The minced tissue was thereafter placed into a sterilized 2.0 mL Eppendorf tube.

The TRIzol reagent was utilized following the supplied instructions to extract total RNA. In the LV, 1 mL of TRIzol was added, while in each of RA, RV, and LA, 500 mL of TRIzol was supplied. The tissue was homogenized on ice using a homogenizer. The nucleoprotein complex was incubated for a duration of 10 minutes to ensure complete dissociation. Cell lysis was performed by supplementing the TRIzol reagent with 0.2 mL chloroform per 1 mL, followed by vigorous vortexing. Following a 15-minute RT incubation, centrifugation was performed at 12000 × g and 4 °C for 15 minutes. The mixture was partitioned over three distinct layers: the lower layer consisted of red phenol-chloroform, the middle layer was transparent, and the upper phase was an aqueous solution without color. The RNA supernatant was pipetted into a fresh vessel. Isopropanol (0.5 mL per 1 mL TRIzol) was added for RNA precipitation, followed by 10 minutes RT incubation and 10-minute centrifugation at 12000 × g (4°C). The precipitation of total RNA produced a white flocculent pellet that accumulated at the bottom of the tube. The liquid above the sediment was removed using a micro pipettor. Lysis efficiency was enhanced by supplementing the TRIzol solution with an equivalent volume of 75% ethanol. The sediment was reconstituted. The sample was gently mixed using a vortex mixer for a short duration.

Following centrifugation at 7500 × g for 5 minute (4°C), supernatant was removed via micropipette aspiration. Following 10 minutes of air-drying, the RNA pellet was resuspended in 40 µL RNase-free water with vigorous pipette mixing. The sample was heated at 56°C for 10 minutes in a heating block. After brief centrifugation (1200 × g, 1 minute), RNA quality was evaluated by NanoDrop 2000 spectrophotometry. Sample demonstrating A260/A280 ratio between 1.8-2.0 was deemed acceptable. Purified RNA was adjusted to 50 ng/µL in RNase-free water and archived at -80°C for long-term storage.

2.4.2 Complementary DNA (cDNA) Synthesis Reaction

cDNA was generated from 500 ng RNA using SuperScript IV Reverse Transcriptase Kit under standard reaction conditions. A 20 µl reaction mixture containing annealed RNA components (Table 6) and reverse transcription reactions (Table 7) was prepared for each sample.

Table 6. Annealed RNA components

Procedure	Component	Volume
Anneal primer to template RNA	50 ng / μL random hexamers	1 μL
	10 mM dNTP mix	1 μL
	Template RNA (50 ng/μL)	10 μL
	RNase-free water	1 μL

The constituents were thoroughly combined and subjected to a brief centrifugation. The RNA primer mixture was subjected to a thermal treatment at 65°C for 5 minutes, followed by a subsequent incubation on ice for at least 1 minute. The reverse transcription reactions were prepared as indicated in Table 7.

Table 7. Reverse transcription reactions

Procedure	Component	Volume
Prepare reverse transcription reaction mix	5× SSIV Buffer	4 μL
	100 mM DTT	1 μL
	Ribonuclease Inhibitor	1 μL
	SuperScript IV Reverse Transcriptase (200 U/μL)	1 μL

The tube was sealed, thoroughly mixed, and briefly centrifuged. Reverse transcription was initiated by mixing Table 7 reagents with Table 6 RNA, proceeding through incubation steps of 23°C (10 minutes), 55°C (10 minutes), and 80°C (10 minutes for enzyme deactivation).

2.4.3 Primer design

Primers were designed using the Primer-BLAST (Ye et al., 2012). Table 8 detailes all primer sequences employed in this work. The provided primer was in a lyophilized state. The primers were centrifuged prior to the initial use. Working primer solutions (10 μM) were prepared from 100 μM stocks by dilution in RNase-free water.

The primers that are used adhere to the principles of effective primer design. Generally, the length of primers should be a minimum of 18 nucleotides (Abd-Elsalam, 2003) with a GC content of approximately 50-55%, and exhibit minimal secondary structure, such as hairpins or loops (Dieffenbach et al., 1993). All primers incorporate a G/C nucleotide at their 5' terminus, exhibiting melting temperatures approximately 5°C above the target annealing temperature. The forward and reverse primers for qPCR amplify unique target sequences that are 70-180 base pairs long.

Table 8. Primers design

Gene	Forward Primer	Reverse Primer
Meis1	5’GTTGTCCAAGCCATCACCTT-3’	5’-ATCCACTCGTTCAGGAGGAA-3’
MCM3	5’-AGCGCAGAGAGACTACTTGGA-3’	5’-GCGGTTAGCCCTCTTTTCATTC-3’
Apbb1	5’-AGGAGGCCCCAATGGAGTT-3’	5’-GCGCACAGCGAAACACTTG-3’
CCND2	5’-GAGTGGGAACTGGTAGTGTTG-3’	5’-CGCACAGAGCGATGAAGGT-3’
TP53	5’-GTCACAGCACATGACGGAGG-3’	5’-TCTTCCAGATGCTCGGGATAC-3’
GAPDH	5’-AACTTTGGCATTGTGGAAGG-3’	5’-GGATGATGTTCTGGGCAGC-3’

2.4.3.1 Primer test

Prior to conducting a qPCR reaction, the specificity and efficiency of the primers were assessed. This can be achieved by performing an annealing temperature test, a primer standard test, and then examining the product through electrophoresis on a DNA acrylamide gel. Melting curve analysis was performed to validate primer annealing specificity. There should only be one peak on the curve with no shoulders. The specific PCR products were differentiated from other products such as primer dimers by employing this method. qPCR reaction efficiency was determined through standard curve analysis. The reaction efficiency should always fall within the range of 90-110%. The R^2 valve should be as close to 1.0 as possible, falling within an acceptable range of 0.95-1.0. A single melting curve, an efficiency range of 90-110%, a coefficient of determination greater than 0.95, and a suitable fragment in electrophoresis were considered sufficient evidence for the efficacy of a primer pair.

2.4.3.1.1 Annealing temperature test

The iTaqTM Universal SYBR Green supermix and other reaction components (as indicated in Table 9) were thawed to RT. After thorough vortexing and brief centrifugation, sample was maintained on ice with SYBR Green protected from light exposure. The Mastermix was prepared in accordance with the instructions provided in Table 9.

1 µl of template cDNA and 9 µl of Mastermix were included in each reaction. The concentration of template cDNA used was 2.5 ng/µl. The mixture was placed into the designated 96-well plate and the plate was securely covered. The plate was subjected to a short centrifugation to remove the air bubbles. The thermal cycling protocol (Table 10) was programmed on the real-time PCR detection equipment.

Table 9. PCR reactions for annealing temperature test

Components	Amount
iTaq Universal Sybrgreen Supermix	5 µL
Forward primer (10 µM)	1 µL
Reverse primer (10 µM)	1 µL
cDNA template (2.5 ng/µl)	1 µL
Nuclease-free water	2 µL
Total volume	10 µL

Table 10. PCR protocol for annealing temperature test

Steps	Temperature	Duration	Cycle
Polymerase activation	95 ºC	2 minutes	40 x
DNA Denaturation	95 ºC	15 seconds	
Annealing	55 ºC -65 ºC	1 minute	
Melt cure analysis	65°C-95°C		

2.4.3.1.2 DNA acrylamide gel test

Following the completion of qPCR runs, the 96-plate was briefly centrifuged. Each sample was combined with 1 µl of 6× loading dye and electrophoresed alongside a DNA ladder on agarose gel (Table 11). The gel was then subjected to electrophoresis for a duration of one hour at a voltage of 120 volts. Subsequently, the gel was placed under UV light for photography, and the height of the band was compared to the estimated length of the amplicon produced by the primer pairs. An examination was conducted to determine whether a single band was observed at the appropriate elevation. Furthermore, melting curve analysis enabled precise determination of the optimal annealing temperature for all primer combinations.

Table 11. Reactions for DNA arylamide gel test

Components	Amount
Ladder 50 bp	2 µL
Loading dye (6x)	1 µL
Nuclease-free water	3 µL

2.4.3.1.3 cDNA standards test

Following that, a series of standard dilutions of the tested sample cDNA were prepared (Table 12).

Table 12. cDNA dilutions

Standards	Concentrations (ng/μL)
Standard 1	12.5
Standard 2	6.25
Standard 3	3.12
Standard 4	1.56
Standard 5	0.78
Standard 6	0.39
Standard 7	0.195
Standard 8	0.975

The mixture for qPCR (Table 9) was then pipetted in duplicates in a 96-well plate using the following approach. The plate was sealed using foil and underwent centrifugation. It was then put through to the PCR program (Table 13) in the thermocycler.

Table 13. PCR program for cDNA standards test

Steps	Temperature	Duration	Cycle
Polymerase activation	95 °C	2 minutes	40X
DNA Denaturation	95 °C	15 seconds	
Annealing	Meis1: 55.7 °C MCM3: 59 °C Apbb1: 61.4 °C CCND2: 59 °C Tp53: 59 °C GAPDH: 60 °C	1 minute	
Melt cure analysis	65°C-95°C		

Annealing temperatures were optimized via gradient PCR, chosen based on amplification specificity and efficiency. In an ideal qPCR reaction, the melting curve exhibited a single peak. By employing this approach, it became possible to differentiate specific PCR products from other products, such as primer dimers.

2.4.4 qPCR

After determining the optimal conditions for qPCR through primer testing, qPCR was conducted. Target gene expression, including Meis1, CCND2, MCM3, Apbb1, and TP53, was quantified by qPCR. The SYBR Green reagent was utilized for this purpose. The qPCR procedure started by loading the specified approach (Table 9) into a 96-well plate. The plate was then sealed with foil and centrifuged. The qPCR was carried out in a thermocycler according to the following protocol (Table 14). All samples were amplified in duplicates. To prevent contamination, all experimental steps were conducted in a sterile environment. Gene expression levels were normalized to GAPDH and analyzed via the ΔCt method.

2.5 Immunofluorescence staining

2.5.1 Heart harvest and sectioning

The harvested heart tissue was placed in a 4% PFA fixative solution for a duration of 30 minutes in order to preserve tissue morphology and ensure the retention of protein antigenicity. The tissue was transferred to a solution containing 30% sucrose and allowed to undergo a dehydration process for a duration of 24 hours.

Heart was chamber-dissected (RA/LA/RV/LV), flash-frozen on dry ice in optimal cutting temperature (OCT) matrix, and positioned to maintain anatomical orientation, subsequently embedded. A section measuring 10 micrometers was obtained from each tissue block and affixed onto Superfrost Plus slides.

2.5.2 Immunofluorescence staining

For fixation, slides were treated with 4% paraformaldehyde solution (10 minutes, RT). Slides were subjected to three 5-minute PBS washes with gentle agitation. To prevent the slides from drying out, water was added to the staining box. A xylol-containing liquid blocker was applied to each tissue separately, marking a circle around each one. A 10-minute treatment with 0.5% Triton X-100 (in PBS) was used for cell permeabilization. The slides were subjected to three rounds of washing with PBS, with each round lasting for a duration of 5 minutes. To reduce non-specific binding and excessive dyeing, a blocking buffer was applied and the sample was incubated for 2 hours. Then, the tissues were incubated with primary antibodies, including rat anti-Ki67 primary antibody, rabbit anti-mouse desmin antibody, chicken anti-mouse vimentin primary antibody, and rabbit anti-mouse CD64 primary antibody, at a temperature of 4^{o}C overnight. On the subsequent day, the slides were subjected to three rounds of washing using a washing buffer, with each round lasting for a duration of 5 minutes. The tissues were subjected to incubation with Alexa Fluor 647 goat anti-rat IgG, Alexa Fluor 488 goat anti-rabbit IgG, Alexa Fluor 555 goat anti-chicken IgG, AF 568 Goat anti-rabbit, and Hoechst for 45 minutes at RT. Slides were washed three times (5 min per wash) in washing buffer. Tissue sections were mounted with fluorescent mounting medium and coverslipped. The slides were stored within a section protector in order to shield them from light exposure. The slides were kept in the air for at least 30 minutes for air drying. The utilization of fluorescence imaging was conducted using a Leica Fluorescence Microscopy.

2.5.3 Microscopy

Following immunofluorescence staining, an initial overview image was captured using the Leica DM6 B microscope at a magnification of 10X for each individual section. Images were then captured at a magnification of 20X in order to completely cover all areas and animals. The images were assessed utilizing the Fiji ImageJ-win64 software. The assessment of cardiomyocyte proliferation was conducted by quantifying the proportion of nuclei that were positive for both Ki67 and desmin, as well as the total number of desmin-positive cell nuclei. Fibroblast proliferation was evaluated by determining the percentage of cells co-expressing Ki67 and vimentin, along with the total count of vimentin-positive cells. Accordingly, the proportion of Ki67/vimentin double-positive cells was calculated relative to the total vimentin-positive cell population. Macrophage proliferation was assessed by determining the percentage of nuclei co-expressing Ki67 and CD64, along with the total CD64-positive cell count. For this purpose, nuclei co-expressing Ki67 and CD64 were first counted, and their ratio to CD64-positive cells was then calculated.

2.6 Statistical analysis

Data are reported as mean ± SEM (standard error of the mean). Statistical comparisons were performed in GraphPad Prism 10.0, employing Mann-Whitney tests for continuous data and either Fisher's exact or Chi-square tests for categorical variables, with significance defined as $p<0.05$

3. Results

3.1 Cardiac dimensions and systolic function were unaffected by Meis1 inhibition

Echocardiographic assessment evaluated cardiac structure and systolic function following Meis1 inhibition, measuring IVS, left ventricular posterior wall thickness (LVPW), LVID, and LA diameter. Figure 12 displays representative parasternal long-axis B-mode and M-mode recordings.

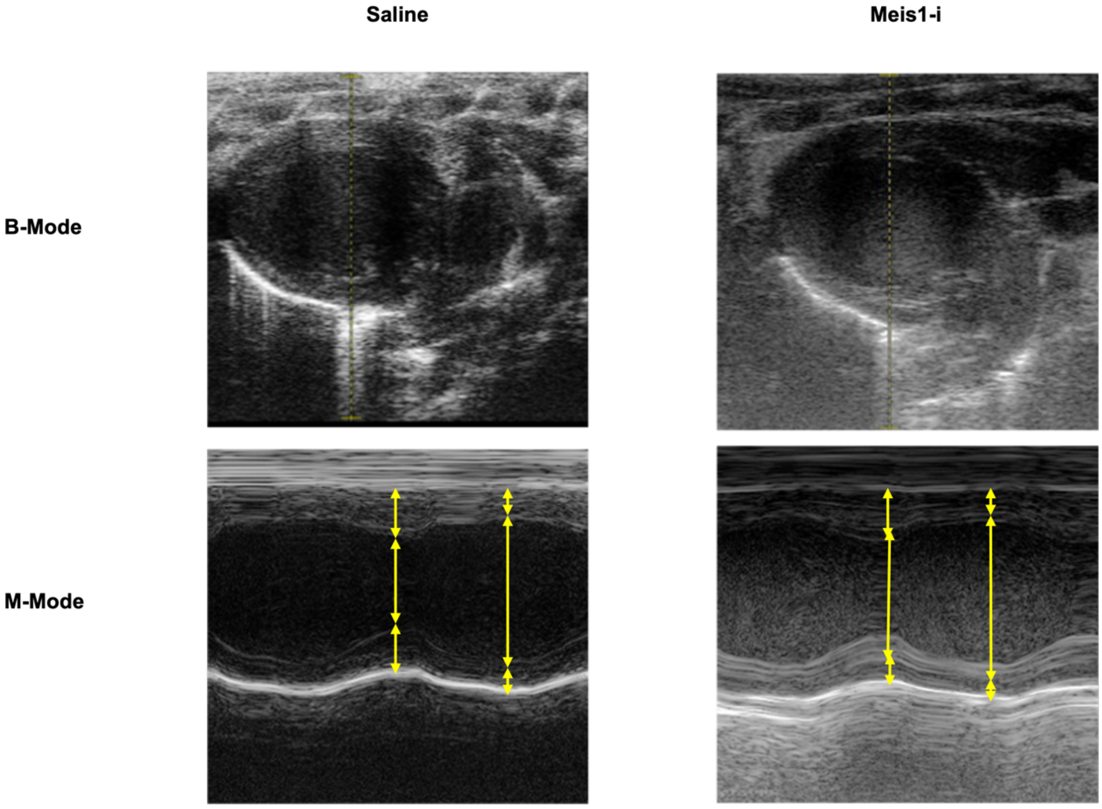

Figure 12. Representative Echocardiographic images. Representative Echocardiographic B-mode and M-mode images from saline (left panel) and Meis1 inhibitor-treated mice (right panel) in parasternal long axis. Meis1-i represents the Meis1-inhibitor group.

EF was assessed to investigate the role of Meis1 in cardiac systolic function. Meis1 inhibitor-treated mice exhibited a normal cardiac systolic function as indicated by the EF (saline vs. Meis1 inhibitor: 67.81 ± 1.26 % vs. 66.81 ± 1.40 %, *p*=0.50, Figure 13).

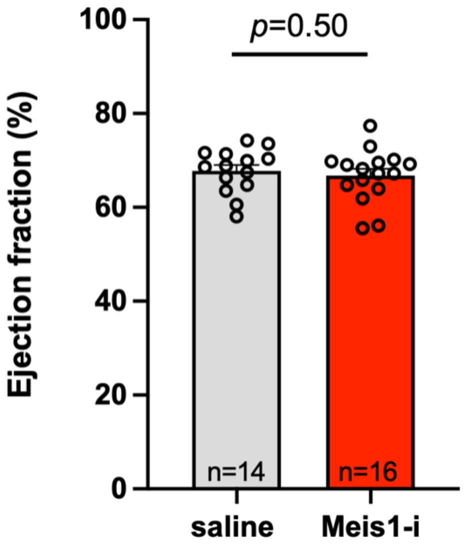

Figure 13. EF. EF was compared between saline-treated mice and Meis1 inhibitor-treated mice. Data were expressed as mean ± SEM. Grey circles represent data of individual mice. Mann-Whitney U test was used. *$p<0.05$. Meis1-i represents the Meis1-inhibitor group.

Echocardiography from parasternal long axis showed no significant differences in LVID (saline vs. Meis1 inhibitor: 3.82 ± 0.06 mm vs. 3.78 ± 0.05 mm, p=0.77, Figure 14A) and IVS (saline vs. Meis1 inhibitor: 0.72 ± 0.02 mm vs. 0.68 ± 0.03 mm, p=0.16, Figure 14B). Similarly, LVPW (saline vs. Meis1 inhibitor: 0.67 ± 0.02 mm vs. 0.66 ± 0.02 mm, p=0.89, Figure 14C), and LA diameter (saline vs. Meis1 inhibitor: 1.86 ± 0.04 mm vs. 1.92 ± 0.04 mm, p=0.44, Figure 14D) were unaffected (Figure 14).

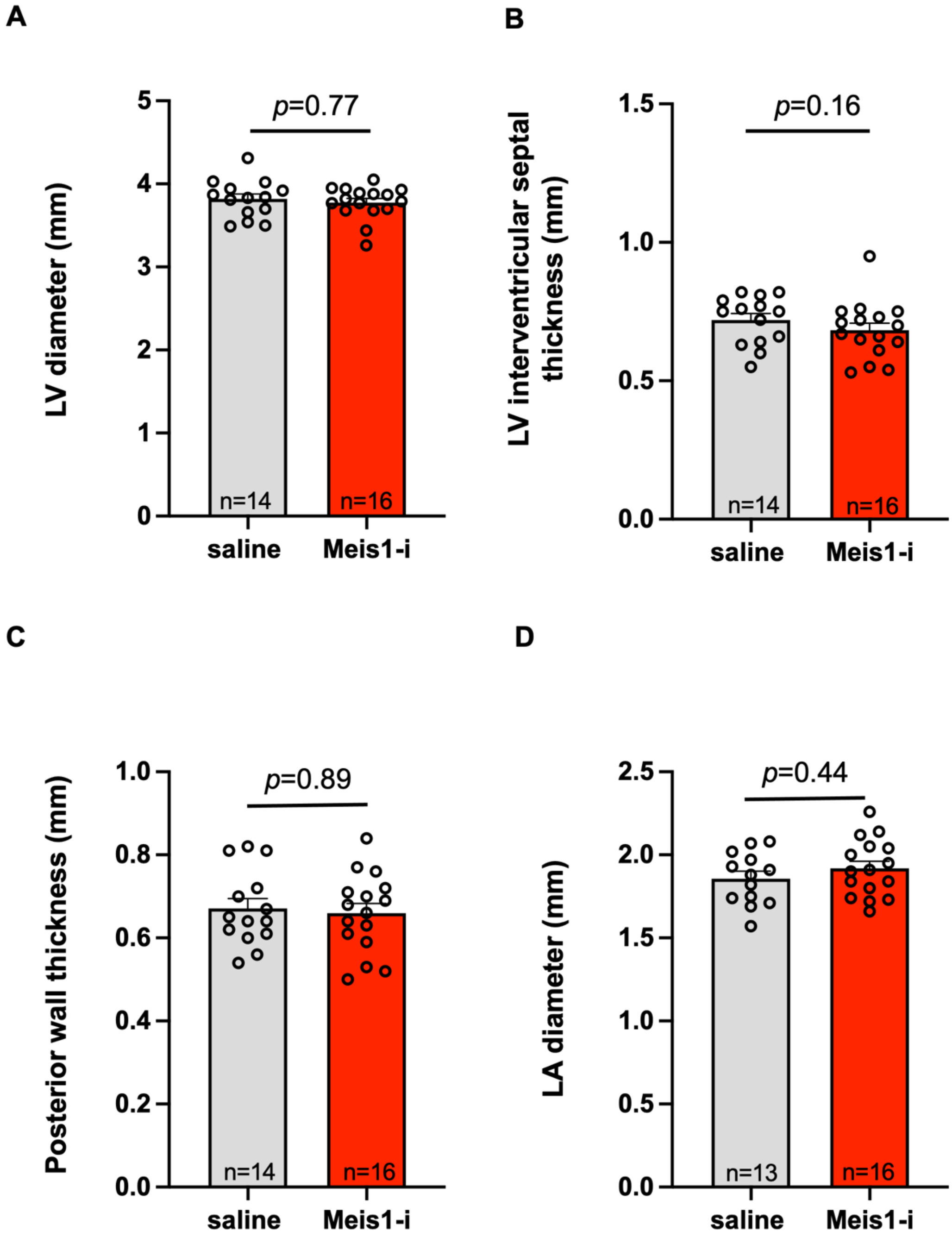

Figure 14. Echocardiographic measurements of cardiac dimensions. Echocardiographic measurements of cardiac dimensions were compared between saline-treated mice and Meis1 inhibitor-treated mice. (A) LVID. (B) IVS. (C) PW. (D) LA diameter. Data were expressed as mean ± SEM. Grey circles represent data of individual mice. Mann-Whitney U test was used. *$p<0.05$. Meis1-i represents the Meis1-inhibitor group.

The heart weight/body weight ratio did not differ significantly between Meis1 inhibitor-treated mice and saline-treated mice (saline vs. Meis1 inhibitor: 0.63 ±

0.01% vs. 0.65 ± 0.01%, *p*=0.09, Figure 15). In sum, Meis1 inhibition has no effect on cardiac structure or systolic function.

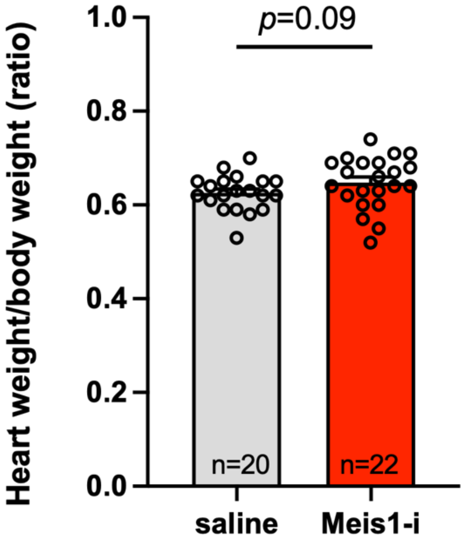

Figure 15. Heart weight/body weight ratio. The heart weight/body weight ratio was compared between saline and Meis1 inhibitor-treated mice. Data were expressed as mean ± SEM. Grey circles represent data of individual mice. Mann-Whitney U test was used. **p*<0.05. Meis1-i represents the Meis1-inhibitor group.

3.2 Impaired sinus node function after Meis1 inhibition

SNRT is an indicator of sinus node function (Steinbeck and Lüderitz, 1976). SNRT at three pacing cycle lengths: 120 ms, 100 ms, and 80 ms were measured respectively (Figure 16). SNRT/BCL ratio (%) under each pacing rate was calculated. SNRT/BCL ratio at 120 ms pacing cycle length did not show any difference between saline-treated mice and Meis1 inhibitor-treated mice (saline vs. Meis1 inhibitor: 129.61 ± 8.06 vs. 133.78 ± 5.86, *p*=0.48, Figure 16A). At 100 ms and 80 ms pacing cycle lengths, Meis1 inhibitor-treated mice had significantly higher SNRT/BCL ratio compared to saline-treated mice (at 100 ms cycle length, saline vs. Meis1 inhibitor: 133.22 ± 10.36 vs. 156.99 ± 9.20, **p*<0.05, Figure 16B; at 80 ms cycle length, saline vs. Meis1 inhibitor: 125.19 ± 8.31 vs. 154.86 ± 5.55, ****p*<0.001, Figure 16C).

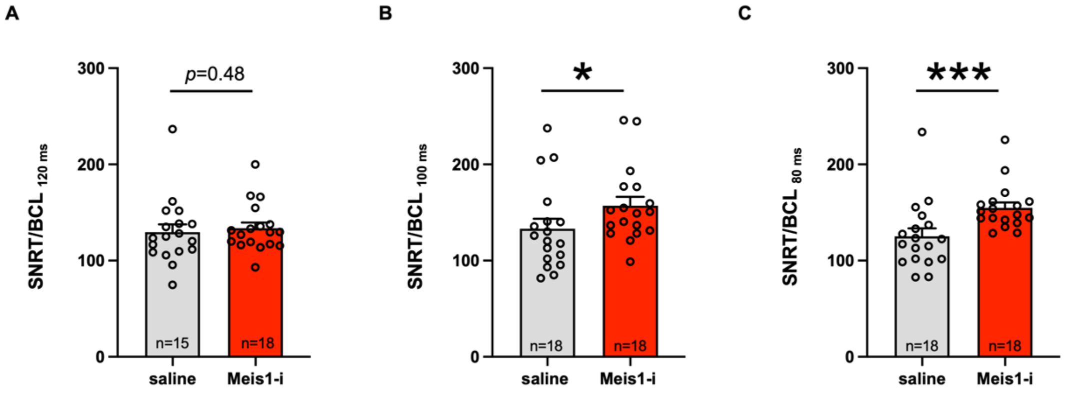

Figure 16. SNRT/BCL ratio. (A-C) SNRT/BCL ratio at 120, 100, and 80 ms pacing cycles. Data show mean ± SEM with grey circles indicating individual mouse values. **p*<0.05, ***p*<0.01 by Mann-Whitney U test. Meis1-i represents the Meis1-inhibitor group.

To further assess the impact of Meis1 inhibition on sinus node function in awake mice, implantable telemetry devices were used, and the incidence of sinus pauses was evaluated (Figure 17). Over the 30 days period, no sinus pause was observed in saline-treated mice (0/4 mice), resulting in a 0% incidence rate of sinus pause. In contrast, one sinus pause was observed in one mouse from the Meis1 inhibitor-treated group (1/4 mice) corresponding to a 25% incidence rate. Figure 17A shows the representative sinus pause. Meis1 inhibition showed no significant effect on spontaneous sinus pause incidence between groups (Figure 17B).

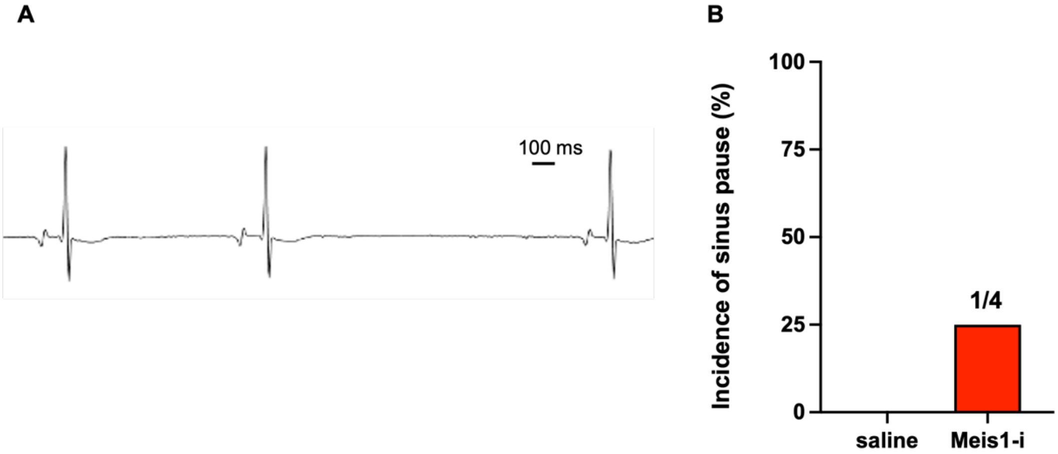

Figure 17. The incidence of sinus pauses. The incidence of sinus pauses was compared between the saline and Meis1 inhibitor groups. Only episodes with a duration greater than one second were included. (A) The representative sinus pause episode from the Meis1 inhibitor-treated mouse. (B) Incidence of sinus pauses. Data represent mean ± SEM, **p*<0.05 by Fisher's exact test. Meis1-i represents the Meis1-inhibitor group.

3.3 Prolonged atrial refractoriness after Meis1 inhibition

AERP served as a metric for assessing atrial conduction/refractoriness (Maguire et al., 2000). Meis1 inhibition significantly prolonged AERP versus saline controls at both 120 and 100 ms cycle lengths (at 120 ms cycle length, saline vs. Meis1 inhibitor: 40.44 ± 1.49 ms vs. 48.40 ± 2.17 ms, ***p*<0.01, Figure 18A; at 100 ms cycle length, saline vs. Meis1 inhibitor: 41.44 ± 2.07 ms vs. 48.75 ± 2.05 ms, **p*<0.05, Figure 18B).

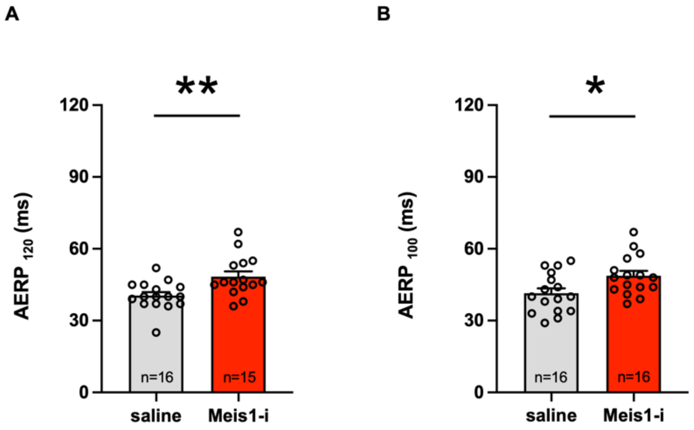

Figure 18. AERP. AERP was compared between the saline and Meis1 inhibitor groups. AERP measurements at basic cycle lengths of (A) 120 ms (B) 100 ms. Data represent mean ± SEM with grey circles indicating individual mouse values. Statistical significance by Mann-Whitney U test, *$p<0.05$, **$p<0.01$.

3.4 AVN function was examined after Meis1 inhibition

The impact of Meis1 inhibition on AVN function was assessed by measuring the PR interval in anesthesized mice 10 days after Meis1 inhibition (ECG) and in conscious mice over a 30-day observation (Telemetry), in addition to evaluating Wenckebach cycle length, 2:1 cycle length, and VA conduction during the EP study. Compared with saline-treated mice, Meis1 inhibitor-treated mice had a significantly prolonged PR interval in anesthesized mice 10 days after Meis1 inhibition (saline vs. Meis1 inhibitor: 36.63 ± 0.88 ms vs. 39.28 ± 0.97 ms, *$p<0.05$, Figure 19A). In conscious mice, the PR interval exhibited no differences between Meis1 inhibitor-treated mice and saline-treated mice during daytime recordings over 30 days of observation; however, the PR interval of Meis1 inhibitor-treated mice demonstrated a significant increase on days 10 and 30 compared to baseline measurements (Meis1 inhibitor 10 days vs. Meis1 inhibitor baseline: 34.79 ± 1.4 ms vs. 31.02 ± 0.71 ms, *$p<0.05$; Meis1 inhibitor 30 days vs. Meis1 inhibitor baseline: 36.27 ± 0.82 ms vs. 31.02 ± 0.71 ms, **$p<0.01$, Figure 19B). During nighttime telemetry recordings, the inhibition of Meis1 had an impact on the PR interval on day 10 (saline vs. Meis1 inhibitor: 31.53 ± 1.10 ms vs. 34.67 ± 0.36 ms, *$p<0.05$, Figure 19C).

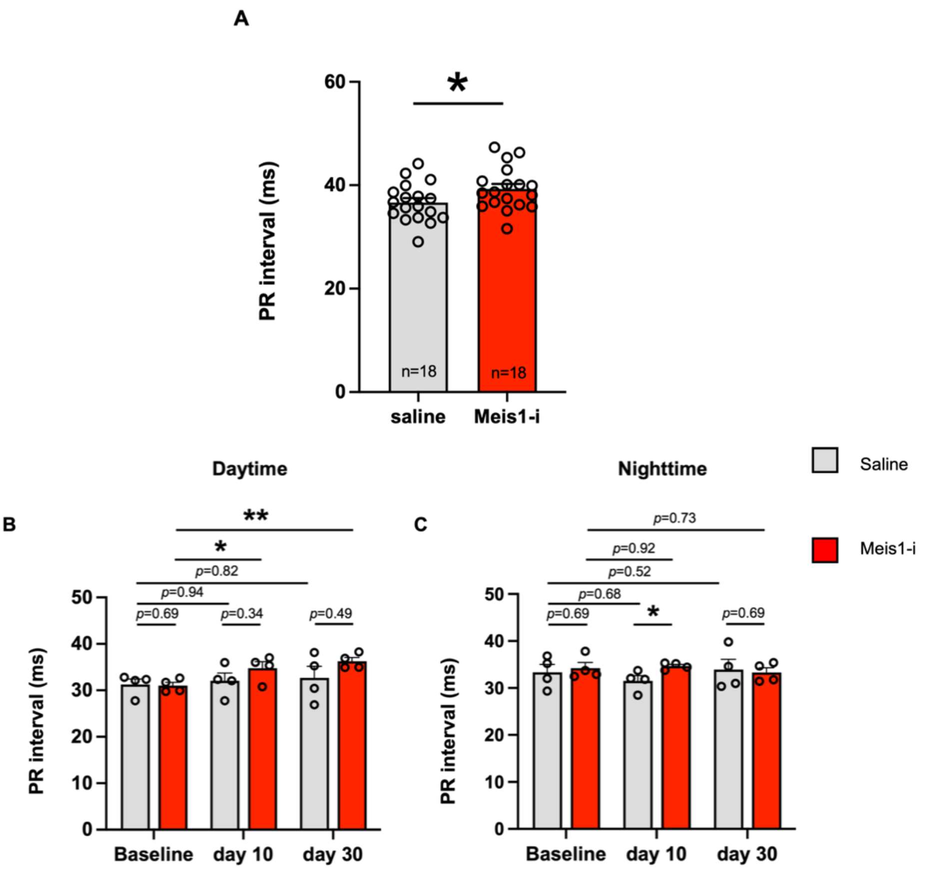

Figure 19. PR interval in anesthesized mice 10 days after Meis1 inhibition (ECG) and in conscious mice over a 30-day observation (Telemetry). PR interval was compared between the saline and Meis1 inhibitor groups. (A) PR interval in anesthesized mice 10 days after Meis1 inhibition. (B) Daytime PR interval in conscious mice during a 30-day observation. (C) Nighttime PR interval in conscious mice over a 30-day observation. Data were presented as mean ± SEM. Grey circles denote the data from single mice. One-way ANOVA accompanied by Dunnett's test was employed within the same group, and the Mann-Whitney-U Test was used between the two groups. *$p<0.05$, **$p<0.01$. Meis1-i represents the Meis1-inhibitor group.

The AV conduction properties were measured by EP study. No significant difference in antegrade AV conduction was observed between the two groups, as evidenced by Wenckebach cycle length (saline vs. Meis1 inhibitor: 77.79 ± 2.57 ms vs. 80.35 ± 3.02 ms, $p=0.38$, Figure 20A), 2:1 cycle length (saline vs. Meis1 inhibitor: 61.58 ± 2.02 ms vs. 63.47 ± 2.37 ms, $p=0.70$, Figure 20B) or retrograde AV conduction (saline vs. Meis1 inhibitor: 82.82 ± 3.58 ms vs. 83.09 ± 3.73 ms, $p=0.91$, Figure 20C).

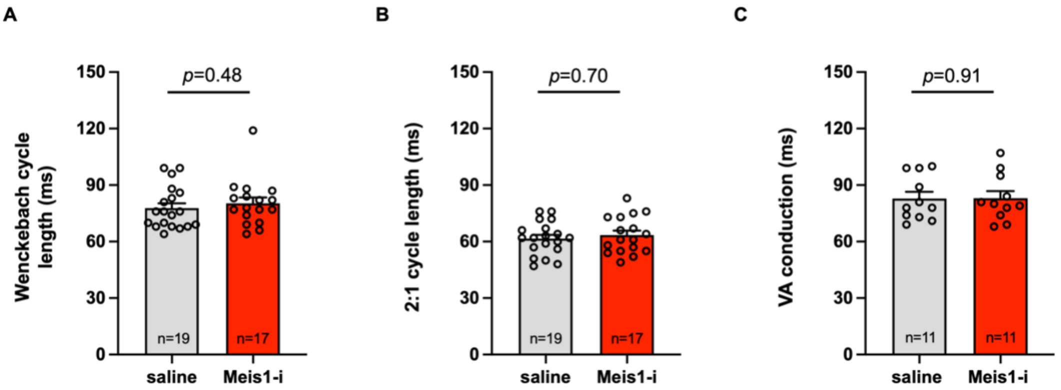

Figure 20. AV conduction properties. AV conduction properties were compared between Meis1 inhibitor-treated mice and saline-treated mice. (A) Wenckebach cycle length. (B) 2:1 AV conduction cycle length. (C) VA conduction. Values represent mean ± SEM with individual data points, *$p<0.05$ by Mann-Whitney test. Meis1-i represents the Meis1-inhibitor group.

Furthermore, AVERP was not different between the two groups of saline-treated mice and Meis1 inhibitor-treated mice (at 120 ms cycle length, saline vs. Meis1 inhibitor: 56.24 ± 2.55 ms vs. 58.06 ± 3.89 ms, *p*=0.94, Figure 21A; at 100 ms cycle length, saline vs. Meis1 inhibitor: 58.53 ± 2.72 ms vs. 55.61 ± 3.42 ms, *p*=0.40, Figure 21B). In sum, AV conduction properties were not affected after Meis1 inhibition.

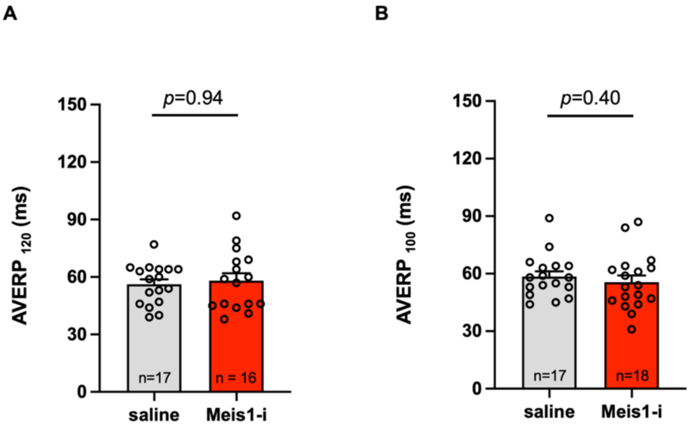

Figure 21. AVERP. AVERP was compared between Meis1 inhibitor-treated mice and saline-treated mice. (A) AVERP at a basic cycle length of 120 ms. (B) AVERP at a basic cycle length of 100 ms. Data were expressed as mean ± SEM. Grey circles represent data of individual mice. Statistical significance was assessed by the Mann-Whitney-U test, *$p<0.05$. Meis1-i represents the Meis1-inhibitor group.

To evaluate the effect of inhibiting Meis1 on the occurrence of spontaneous AV block in conscious mice, the incidence of AV block was evaluated (Figure 22).

There was no difference in the incidence of spontaneous AV block between saline-treated mice (25%) and Meis1 inhibitor-treated mice (25%). The representative spontaneous AV block is shown in Figure 22A.

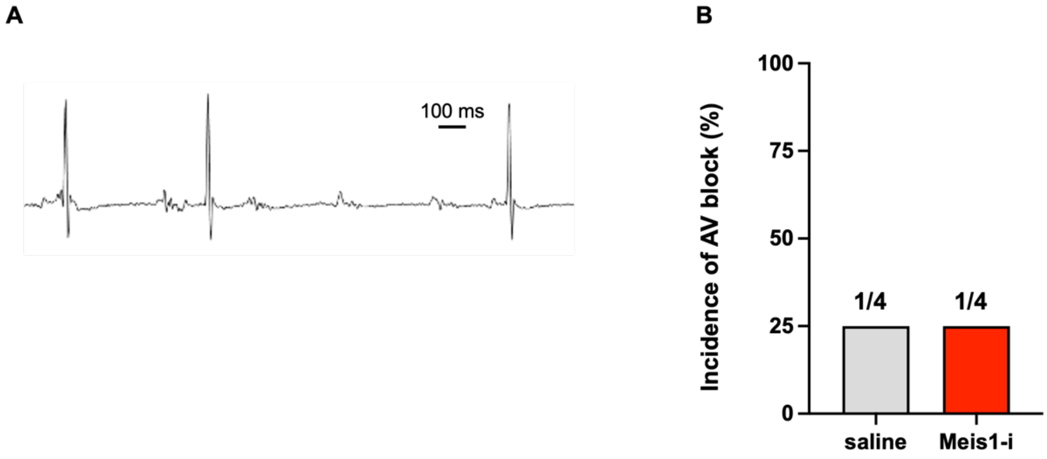

Figure 22. The incidence of AV block. The incidence of AV block was compared between Meis1 inhibitor-treated mice and saline-treated mice. Only episodes with a duration greater than one second were included. (A) A representative AV block episode from a Meis1 inhibitor-treated mouse. (B) Incidence of AV block. Values represent mean ± SEM, *$p<0.05$ by Fisher's exact test. Meis1-i represents the Meis1-inhibitor group.

3.5 Unchanged heart rate, P wave duration, and HRV after Meis1 inhibition

Heart rate and P wave duration in anesthesized mice 10 days after Meis1 inhibition (ECG study) and in conscious mice over a 30-day observation (Telemetry) were measured, respectively. In anesthesized mice 10 days after Meis1 inhibition, heart rate (saline vs. Meis1 inhibitor: 320.50 ± 13.00 bpm vs. 308.12 ± 10.97 bpm, $p=0.56$, Figure 23A) and P wave duration (saline vs. Meis1 inhibitor: 12.19 ± 0.39 ms vs. 12.47 ± 0.29 ms, $p=0.58$, Figure 23B) did not differ between the saline and Meis1 inhibitor groups.

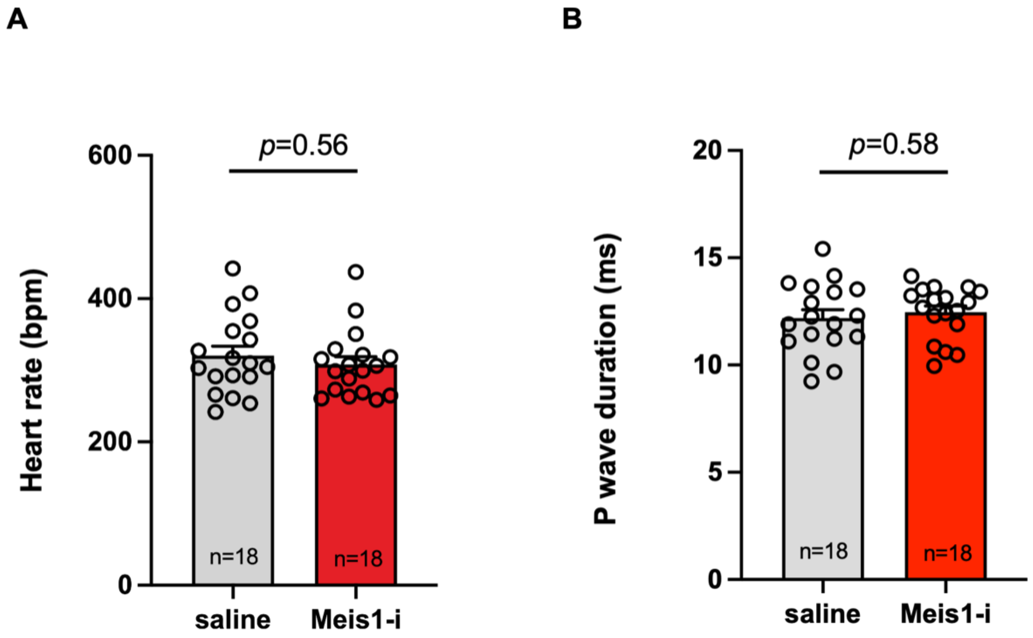

Figure 23. Heart rate and P wave duration in anesthesized mice 10 days after Meis1 inhibition. Heart rate and P wave duration in anesthesized mice 10 days after Meis1 inhibition were compared between saline and the Meis1 inhibitor-treated mice. (A) Heart rate. (B) P wave duration. Data represent mean ± SEM with individual values. Mann-Whitney U test was used, **p*<0.05. Meis1-i represents the Meis1-inhibitor group.

To further investigate the effects of Meis1 inhibition on cardiac EP in conscious mice over a 30-day observation, measurements obtained from saline-treated mice were compared to Meis1 inhibitor-treated mice during daytime and nighttime recordings. Heart rate showed no significant differences between saline- and Meis1 inhibitor-treated mice at baseline, day 10, or day 30 in both daytime and nighttime recordings (Figure 24A and 24B). Meis1 inhibitor-treated mice exhibited significantly reduced heart rates in daytime ECGs on day 10 and day 30 relative to baseline (day 10 vs. baseline: 373.78 ± 13.20 bpm vs. 460.19 ± 13.2 bpm, ***p<0.001; day 30 vs. baseline: 368.24 ± 9.34 bpm vs. 460.19 ± 13.20 bpm, ***p<0.001, Figure 24A). Saline-treated mice showed a comparable but non-significant trend (Figure 24A and 24B).

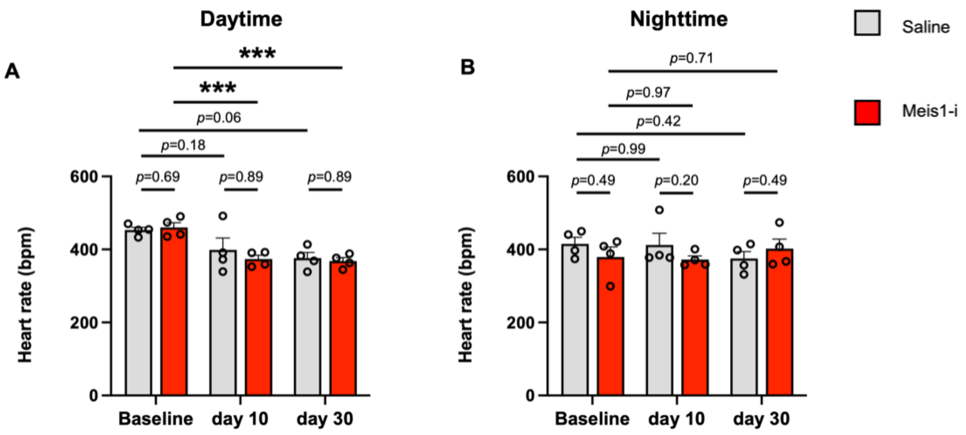

Figure 24. 30-day heart rate in conscious mice. Heart rate in conscious saline- and Meis1 inhibitor-treated mice was compared across 30 days, analyzing both daytime (left) and nighttime (right) periods. (A) Daytime heart rate. (B) Nighttime heart rate. Values represent mean ± SEM with individual data points. Within-group comparisons used ANOVA with Dunnett's test; between-group comparisons used Mann-Whitney U test. $*p<0.05$, $**p<0.01$, $***p<0.001$. Meis1-i represents the Meis1-inhibitor group.

P wave duration showed no significant difference between saline and Meis1 inhibitor groups during 30-day monitoring (Figure 25A and 25B).

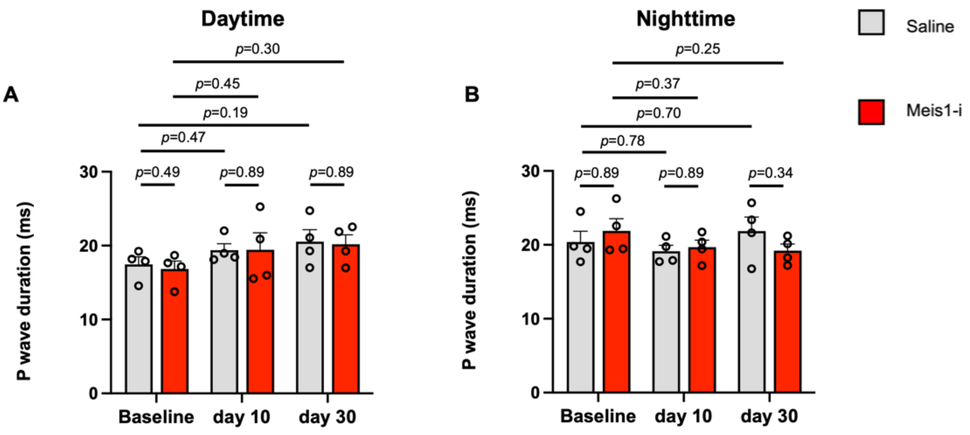

Figure 25. 30-day P wave duration in conscious mice. P wave duration was compared between saline and Meis1 inhibitor groups over 30 days (daytime left, nighttime right). (A) Daytime P wave duration. (B) Nighttime P wave duration. Values represent mean ± SEM with individual data points. Within-group comparisons used ANOVA with Dunnett's test; between-group comparisons used Mann-Whitney U test. $*p<0.05$. Meis1-i represents the Meis1-inhibitor group.

HRV time-domain analysis assessed RR intervals, SDRR, and RMSSD. In the daytime recording, no significant changes in RR intervals, SDRR, or RMSSD were observed between Meis1 inhibitor-treated mice and saline-treated mice (Figure 26A, 26C, 26E). However, variations within the same group were observed at different time intervals. During the nighttime recording, Meis1 inhibitor-treated mice did not show any statistically significant variation in RR interval, SDRR, or RMSSD compared to the saline-treated ones (Figure 26B, 26D, 26F). Details are shown in table 14, table 15, and table 16.

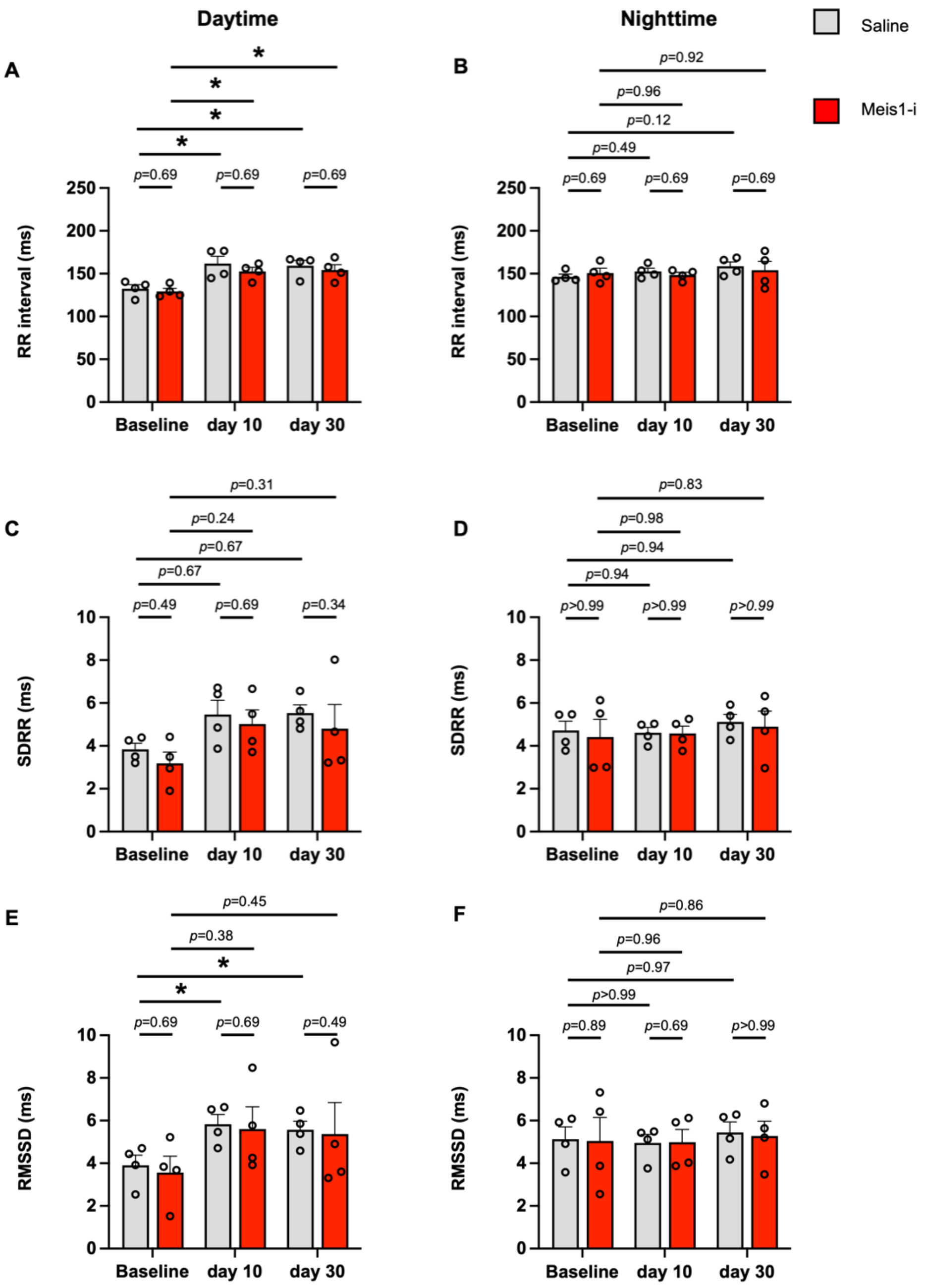

Figure 26. RR interval, SDRR and RMSSD. RR interval, SDRR, and RMSSD were compared between saline-treated mice and Meis1 inhibitor-treated mice during the daytime (left) and nighttime (right). (A) Daytime RR interval. (B) Nighttime RR interval. (C) Daytime SDRR. (D) Nighttime SDRR. (E) Daytime RMSSD. (F) Nighttime RMSSD. Results presented as mean ± SEM where grey circles denote individual values. Statistical analysis included within-group one-way ANOVA with Dunnett's test and intergroup Mann-Whitney U tests. *$p<0.05$. Meis1-i represents Meis1 inhibitor-treated mice.

Table 14. RR interval

Groups	mean±SEM (ms)	p-value
Daytime: Meis1-i baseline vs. saline baseline	129.21±3.56 vs.132.48±4.64	0.69
Daytime: Meis1-i day 10 vs. saline day 10	152.66±4.75 vs.161.81±8.43	0.69
Daytime: Meis1-i day 30 vs. saline day 30	154.29±6.24 vs.159.31±6.18	0.69
Daytime: Meis1-i day 10 vs. Meis1-i baseline	152.66±4.75 vs.129.21±3.56	0.02
Daytime: Meis1-i day 30 vs. Meis1-i baseline	154.29±6.24 vs.129.21±3.56	0.01
Daytime: saline day 10 vs. saline baseline	161.81±8.43 vs.129.21±3.56	0.02
Daytime: saline day 30 vs. saline baseline	159.31±6.18 vs.132.48±4.64	0.03
Nighttime: Meis1-i baseline vs. saline baseline	150.69±5.59 vs.146.37±3.21	0.69
Nighttime Meis1-i day 10 vs. saline day 10	148.42±3.10 vs.152.54±3.83	0.69
Nighttime: Meis1-i day 30 vs. saline day 30	154.02±10.28 vs.158.58±5.14	0.69
Nighttime: Meis1-i day 10 vs. Meis1-i baseline	148.42±3.10 vs.150.69±5.59	0.96
Nighttime: Meis1-i day 30 vs. Meis1-i baseline	154.02±10.28 vs.150.69±5.59	0.92
Nighttime: saline day 10 vs. saline baseline	152.54±3.83 vs.146.37±3.21	0.49
Nighttime: saline day 30 vs. saline baseline	158.58±5.14 vs.146.37±3.21	0.12

Table 15. SDRR

Groups	mean±SEM (ms)	p-value
Daytime: Meis1-i baseline vs. saline baseline	3.19±0.53 vs.3.84±0.29	0.49
Daytime: Meis1-i day 10 vs. saline day 10	5.02±0.66 vs.5.46±0.67	0.69
Daytime: Meis1-i day 30 vs. saline day 30	4.81±1.12 vs.5.53±0.38	0.34
Daytime: Meis1-i day 10 vs. Meis1-i baseline	5.02±0.66 vs.3.19±0.53	0.24
Daytime: Meis1-i day 30 vs. Meis1-i baseline	4.81±1.12 vs.3.19±0.53	0.31
Daytime: saline day 10 vs. saline baseline	5.46±0.67 vs.3.84±0.29	0.67
Daytime: saline day 30 vs. saline baseline	5.53±0.38 vs.3.84±0.29	0.67

Nighttime: Meis1-i baseline vs. saline baseline	4.41±0.82 vs.4.72±0.43	>0.99
Nighttime Meis1-i day 10 vs. saline day 10	4.58±0.34 vs.4.61±0.25	>0.99
Nighttime: Meis1-i day 30 vs. saline day 30	4.90±0.73 vs.5.12±0.35	>0.99
Nighttime: Meis1-i day 10 vs. Meis1-i baseline	4.58±0.34 vs.4.41±0.82	0.98
Nighttime: Meis1-i day 30 vs. Meis1-i baseline	4.90±0.73 vs.4.41±0.82	0.83
Nighttime: saline day 10 vs. saline baseline	4.61±0.25 vs.4.72±0.43	0.94
Nighttime: saline day 30 vs. saline baseline	5.12±0.35 vs.4.72±0.43	0.94

Table 16. RMSSD

Groups	mean±SEM (ms)	p-value
Daytime: Meis1-i baseline vs. saline baseline	3.57±0.76 vs.3.90±0.48	0.69
Daytime: Meis1-i day 10 vs. saline day 10	5.61±1.04 vs.5.83±0.46	0.69
Daytime: Meis1-i day 30 vs. saline day 30	5.37±1.47 vs.5.57±0.40	0.49
Daytime: Meis1-i day 10 vs. Meis1-i baseline	5.61±1.04 vs.3.57±0.76	0.38
Daytime: Meis1-i day 30 vs. Meis1-i baseline	5.37±1.47 vs.3.57±0.76	0.45
Daytime: saline day 10 vs. saline baseline	5.83±0.457 vs.3.90±0.48	0.02
Daytime: saline day 30 vs. saline baseline	5.57±0.396 vs.3.90±0.48	0.05
Nighttime: Meis1-i baseline vs. saline baseline	5.04±1.11 vs.5.13±0.58	0.89
Nighttime Meis1-i day 10 vs. saline day 10	4.99±0.60 vs.4.95±0.40	0.69
Nighttime: Meis1-i day 30 vs. saline day 30	5.28±0.69 vs.5.45±0.50	>0.99
Nighttime: Meis1-i day 10 vs. Meis1-i baseline	4.99±0.60 vs.5.04±1.11	0.96
Nighttime: Meis1-i day 30 vs. Meis1-i baseline	5.28±0.69 vs.5.04±1.11	0.86
Nighttime: saline day 10 vs. saline baseline	4.95±0.40 vs.5.13±0.58	>0.99
Nighttime: saline day 30 vs. saline baseline	5.45±0.49 vs.5.13±0.58	0.97

Frequency-domain analysis of VLF, LF, and HF power, along with the LF/HF ratio, showed no significant differences between Meis1 inhibitor- and saline-treated mice during daytime recordings (Figure 27A, 27C, 27E, 27G). VLF, LF, HF power, and LF/HF ratio exhibited similar patterns during nighttime (Figure 27B, 27D, 27F, 27H). Details are shown in table 17, table 18, table 19, and table 20.

In summary, Meis1 inhibition does not affect heart rate and HRV.

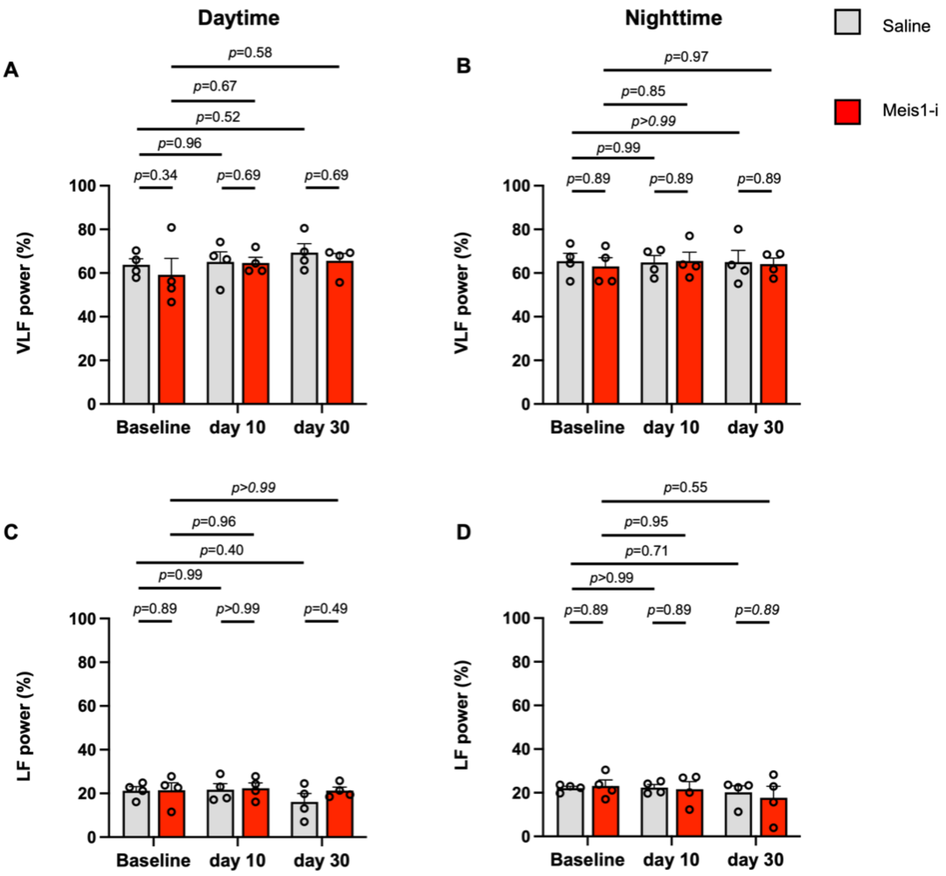

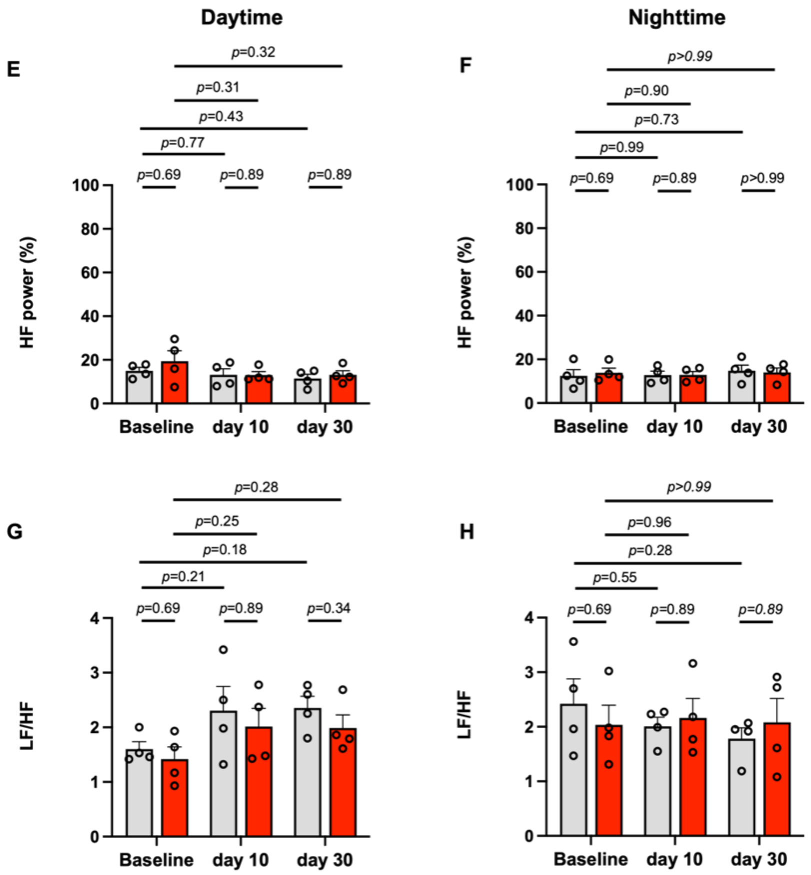

Figure 27. Frequency-domain parameters of HRV. Frequency-domain parameters were compared among the saline and Meis1 inhibitor groups during the daytime (left) and nighttime (right). (A) Percentage of VLF power (0-0.4 Hz) during daytime. (B) Percentage of the VLF power (0-0.4 Hz) during nighttime. (C) Percentage of the LF power (0.4-1.5 Hz) during daytime. (D) Percentage of the LF power (0.4-1.5 Hz) during nighttime. (E) Percentage of the HF power (1.5-4.0 Hz) during daytime. (F) Percentage of the HF power (1.5-4.0 Hz) during nighttime (Shaffer and Ginsberg, 2017). (G) Daytime LF/HF ratio. (H) Nighttime LF/HF ratio. Data were expressed as mean ± SEM. Grey circles represent data of individual mice. One-way ANOVA followed by Dunnett's test was used within the same group, and the Mann-Whitney-U Test was used between saline and Meis1 inhibitor group. **p*<0.05. Meis1-i represents Meis1 inhibitor-treated mice.

Table 17. Percentage of VLF

Groups	mean±SEM	p-value
Daytime: Meis1-i baseline vs. saline baseline	59.21±7.50 vs.63.81±2.75	0.34
Daytime: Meis1-i day 10 vs. saline day 10	64.62±2.57 vs.65.12±4.63	0.69
Daytime: Meis1-i day 30 vs. saline day 30	65.61±3.32 vs.69.37±4.10	0.69
Daytime: Meis1-i day 10 vs. Meis1-i baseline	64.62±2.57 vs.59.21±7.50	0.67
Daytime: Meis1-i day 30 vs. Meis1-i baseline	65.61±3.32 vs.59.21±7.50	0.58

Daytime: saline day 10 vs. saline baseline	65.12±4.63 vs.63.81±2.75	0.96
Daytime: saline day 30 vs. saline baseline	69.37±4.10 vs.63.81±2.75	0.52
Nighttime: Meis1-i baseline vs. saline baseline	63.01±4.02 vs.65.42±3.61	0.89
Nighttime Meis1-i day 10 vs. saline day 10	65.50±4.05 vs.64.86±3.16	0.89
Nighttime: Meis1-i day 30 vs. saline day 30	64.12±2.75 vs.65.02±5.34	0.89
Nighttime: Meis1-i day 10 vs. Meis1-i baseline	65.50±4.05 vs.65.42±3.61	0.85
Nighttime: Meis1-i day 30 vs. Meis1-i baseline	64.12±2.75 vs.63.01±4.02	0.97
Nighttime: saline day 10 vs. saline baseline	64.86±3.16 vs.65.42±3.61	0.99
Nighttime: saline day 30 vs. saline baseline	65.02±5.34 vs.65.42±3.61	>0.99

Table 18. Percentage of LF

Groups	mean±SEM	p-value
Daytime: Meis1-i baseline vs. saline baseline	21.43±3.49 vs.21.22±1.87	0.89
Daytime: Meis1-i day 10 vs. saline day 10	22.35±2.46 vs.21.75±2.75	>0.99
Daytime: Meis1-i day 30 vs. saline day 30	21.27±1.62 vs.16.14±3.84	0.49
Daytime: Meis1-i day 10 vs. Meis1-i baseline	22.35±2.46 vs.21.43±3.49	0.96
Daytime: Meis1-i day 30 vs. Meis1-i baseline	21.27±1.62 vs.21.43±3.49	>0.99
Daytime: saline day 10 vs. saline baseline	21.75±2.75 vs. 21.22±1.87	0.99
Daytime: saline day 30 vs. saline baseline	16.14±3.84 vs.21.22±1.87	0.40
Nighttime: Meis1-i baseline vs. saline baseline	23.10±2.80 vs.22.15±0.837	0.89
Nighttime Meis1-i day 10 vs. saline day 10	21.63±3.51 vs.22.37±1.39	0.89
Nighttime: Meis1-i day 30 vs. saline day 30	17.71±5.25 vs.20.20±2.99	0.89
Nighttime: Meis1-i day 10 vs. Meis1-i baseline	21.63±3.51 vs.23.10±2.80	0.95
Nighttime: Meis1-i day 30 vs. Meis1-i baseline	17.71±5.25 vs.23.10±2.80	0.55
Nighttime: saline day 10 vs. saline baseline	22.37±1.39 vs. 22.15±0.84	>0.99
Nighttime: saline day 30 vs. saline baseline	20.20±2.99 vs.22.15±0.84	0.71

Table 19. Percentage of HF

Groups	mean±SEM	p-value
Daytime: Meis1-i baseline vs. saline baseline	19.37±4.82 vs.14.98±1.57	0.69
Daytime: Meis1-i day 10 vs. saline day 10	13.04±1.58 vs.13.14±2.70	0.89
Daytime: Meis1-i day 30 vs. saline day 30	13.12±1.95 vs.11.44±1.97	0.89
Daytime: Meis1-i day 10 vs. Meis1-i baseline	13.04±1.58 vs.19.37±4.82	0.31
Daytime: Meis1-i day 30 vs. Meis1-i baseline	13.12±1.95 vs.19.37±4.82	0.32
Daytime: saline day 10 vs. saline baseline	13.14±2.70 vs.14.98±1.57	0.77
Daytime: saline day 30 vs. saline baseline	11.44±1.97 vs.14.98±1.57	0.43
Nighttime: Meis1-i baseline vs. saline baseline	13.90±2.09 vs.12.43±2.86	0.69
Nighttime Meis1-i day 10 vs. saline day 10	12.87±1.59 vs.12.78±1.81	0.89
Nighttime: Meis1-i day 30 vs. saline day 30	14.05±2.01 vs.14.79±2.59	>0.99
Nighttime: Meis1-i day 10 vs. Meis1-i baseline	12.87±1.59 vs.13.90±2.09	0.90
Nighttime: Meis1-i day 30 vs. Meis1-i baseline	14.05±2.01 vs.13.90±2.09	>0.99
Nighttime: saline day 10 vs. saline baseline	12.78±1.81 vs.12.43±2.86	0.99
Nighttime: saline day 30 vs. saline baseline	14.79±2.59 vs.12.43±2.86	0.73

Table 20. LF/HF ratio

Groups	mean±SEM	p-value
Daytime: Meis1-i baseline vs. saline baseline	1.42±0.23 vs.1.60±0.13	0.69
Daytime: Meis1-i day 10 vs. saline day 10	2.02±0.33 vs.2.3±0.44	0.89
Daytime: Meis1-i day 30 vs. saline day 30	1.99±0.24 vs.2.36±0.21	0.34
Daytime: Meis1-i day 10 vs. Meis1-i baseline	2.02±0.33 vs.1.42±0.23	0.25
Daytime: Meis1-i day 30 vs. Meis1-i baseline	1.99±0.24 vs.1.42±0.23	0.28
Daytime: saline day 10 vs. saline baseline	2.31±0.44 vs.1.60±0.13	0.21
Daytime: saline day 30 vs. saline baseline	2.36±0.21 vs.1.60±0.13	0.18

Nighttime: Meis1-i baseline vs. saline baseline	2.04±0.36 vs.2.42± 0.46	0.69
Nighttime Meis1-i day 10 vs. saline day 10	2.16±0.36 vs.2.01±0.17	0.89
Nighttime: Meis1-i day 30 vs. saline day 30	2.08±0.44 vs.1.78±0.20	0.89
Nighttime: Meis1-i day 10 vs. Meis1-i baseline	2.16±0.36 vs.2.04±0.36	0.96
Nighttime: Meis1-i day 30 vs. Meis1-i baseline	2.08±0.44 vs.2.04±0.36	>0.99
Nighttime: saline day 10 vs. saline baseline	2.01±0.17 vs.2.42±0.46	0.55
Nighttime: saline day 30 vs. saline baseline	1.78±0.20 vs.2.42±0.46	0.28

3.6 Unchanged ventricular conduction after Meis1 inhibition

To study the influence of Meis1 inhibition on ventricular conduction, the QRS interval and QTc interval were assessed in anesthesized mice 10 days after Meis1 inhibition (ECG) and in conscious mice over a 30-day observation (Telemetry), respectively. No significant differences in QRS or QTc intervals were observed between saline and Meis1 inhibitor groups 10 days after Meis1 inhibition in anesthetized mice (Figure 28A and 28B). In conscious mice monitored over 30-days no differences in the QRS interval and QTc interval among the groups were observed (Figure 28C-F).

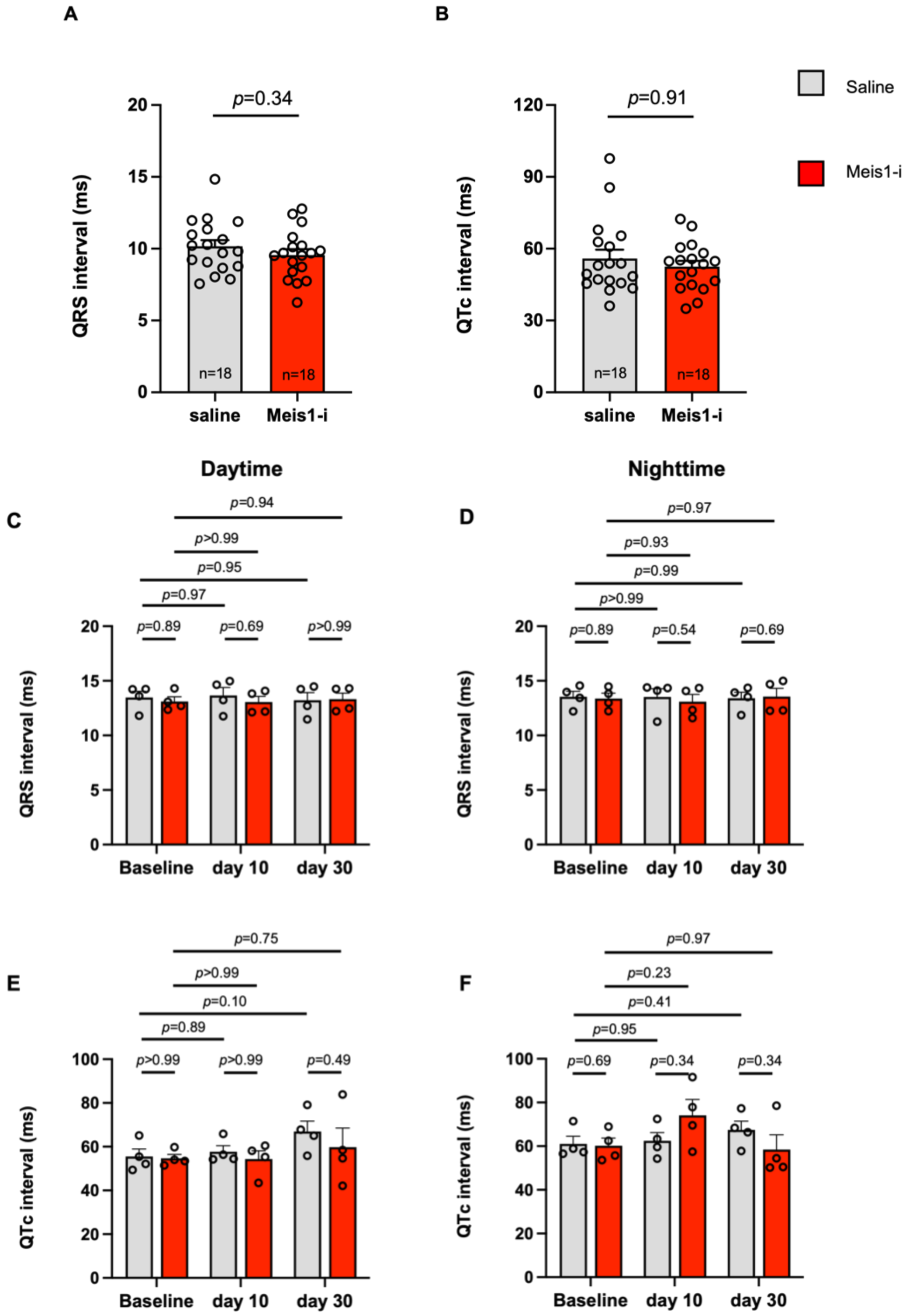

Figure 28. QRS interval and QTc interval in anesthesized mice 10 days after Meis1 inhibition (ECG) and in conscious mice over a 30-day observation (Telemetry). QRS interval and QTc interval were compared between the saline and Meis1 inhibitor groups. (A) QRS interval in anesthesized mice 10 days after Meis1 inhibition. (B) QTc interval in anesthesized mice 10 days after Meis1 inhibition. (The calculation was performed in accordance with Mitchell (Mitchell et al., 1998). (C) Daytime QRS interval in conscious mice during 30-day monitoring. (D) Nighttime QRS interval in conscious mice during 30-day monitoring. (E) Daytime QTc interval in conscious mice during 30-day monitoring. (F) Nighttime QTc interval in conscious mice during 30-day monitoring. Data were expressed as mean ± SEM. Grey circles represent data of individual mice. One-way ANOVA followed by Dunnett’s test was used within the same group, and the Mann-Whitney-U Test was used between saline and Meis1 inhibitor group. *$p<0.05$. Meis1-i represents the Meis1-inhibitor group.

VERP measured during EP study revealed no significant changes between the saline-treated and Meis1 inhibitor-treated mice at both the basic cycle lengths of 120 ms and 100 ms (at 120 ms cycle length, saline vs. Meis1 inhibitor: 49.09 ± 4.42 ms vs. 50.13 ± 3.55 ms, *p*=0.90, Figure 29A; at 100 ms cycle length, saline vs. Meis1 inhibitor: 50.09 ± 4.63 ms vs. 50.00 ± 3.28 ms, *p*=0.85, Figure 29B).

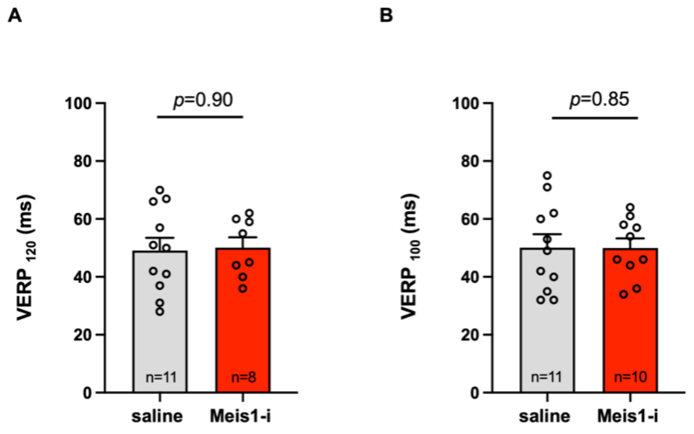

Figure 29. VERP. VERP was compared between the saline and Meis1 inhibitor groups. (A) VERP measured during 120 ms pacing. (B) VERP measured during 100 ms pacing. Data were shown as mean ± SEM, with individual animal measurements depicted as gray data points. Between-group comparisons were analyzed using the Mann-Whitney U test. **p*<0.05. Meis1-i represents the Meis1-inhibitor group.

3.7 Enhanced atrial arrhythmogenesis after Meis1 inhibition

The potential impact of Meis1 inhibition on the inducibility of atrial arrhythmias was investigated by invasive EP studies. The percentage of mice in each group exhibiting atrial arrhythmias and the fraction of stimulations that could successfully induce atrial arrhythmias lasting longer than one second were used to evaluate the arrhythmia inducibility of the mice. Atrial arrhythmias included focal atrial tachycardia, atrial flutter, and AF. A representative AF episode from a Meis1 inhibitor-treated mouse is shown in Figure 30A. Atrial arrhythmias were induced in 44.44% of Meis1 inhibitor-treated mice (10 out of 18), significantly higher than the 10.53% (2 out of 19) observed in saline-treated mice (**p*<0.05, Figure 30B). Furthermore, atrial arrhythmias were induced in 6.04% of stimulations (92 out of a total of 1522) in Meis1 inhibitor-treated mice, compared to 0.43% (6 out of 1410) in saline-treated mice (*****p*<0.0001, Figure

30C). Meis1 inhibitor-treated mice showed a significantly higher average atrial arrhythmia burden compared to saline-treated mice (saline vs. Meis1 inhibitor: 2.47 ± 2..06 s vs. 56.52 ± 25.15 s, *$p<0.05$, Figure 30D).

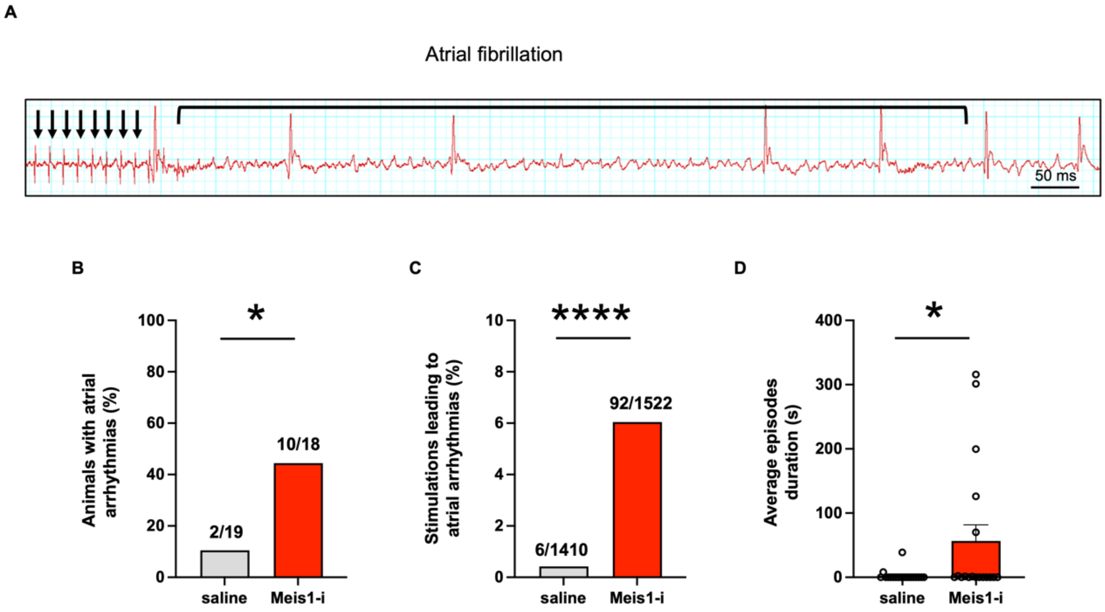

Figure 30. Inducibility of atrial arrhythmias. The inducibility of atrial arrhythmias was compared between the saline and Meis1 inhibitor groups. (A) A representative AF episode from a Meis1 inhibitor-treated mouse. (B) Proportion of mice exhibiting atrial episodes exceeding 1 s. (C) Proportion of stimulations resulting in atrial arrhythmia episodes exceeding 1 s. (D) Average atrial arrhythmia burden. Data were presented as mean ± SEM. Statistical significance was evaluated using Fisher's Exact Test (A, B) and the Mann-Whitney U Test (C). *$p<0.05$, **$p<0.01$, ***$p<0.001$, ****$p<0.0001$. Meis1-i represents the Meis1-inhibitor group.

To further investigate the influence of Meis1 inhibition on spontaneous tachycardia and bradycardia, the prevalence of these episodes was assessed among two groups of mice. The overall incidence of tachycardia and bradycardia was determined by calculating the average number of tachycardia or bradycardia events in each mouse over a period of 30 days. There was no significant difference in the total incidence of tachycardia episodes (saline vs. Meis1 inhibitor: 1.71 ± 0.78 vs. 2.67 ± 1.12, $p=0.49$, Figure 31A) or bradycardia episodes (saline vs. Meis1 inhibitor: 19.88 ± 2.76 vs. 18.46 ± 3.05, $p=0.69$, Figure 31B) between Meis1 inhibitor- and saline-treated mice.

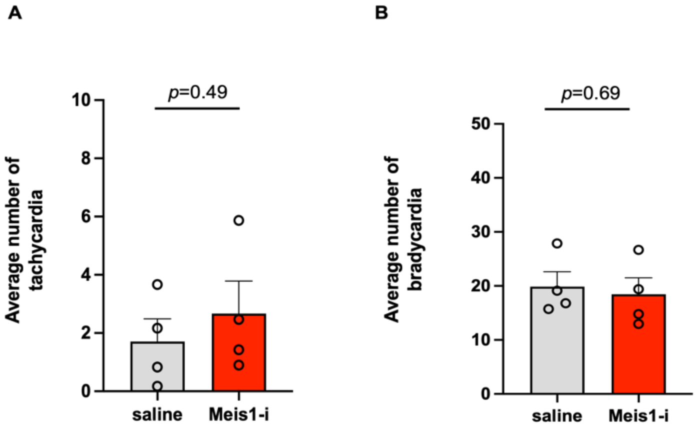

Figure 31. Average number of tachycardia and bradycardia episodes. The average number of tachycardia and bradycardia events was compared between the saline and Meis1 inhibitor groups. (A) Average number of tachycardia events. (B) Average number of bradycardia events. Data were shown as mean ± SEM, with individual animal measurements depicted as gray data points. Between-group comparisons were analyzed using the Mann-Whitney U test. **p*<0.05. Meis1-i represents the Meis1-inhibitor group.

3.8 Meis1 inhibition influenced the cell cycle-related gene expression

The current *in vivo* studies have shown that Meis1 inhibition affects atrial EP and arrhythmogenesis. The cell cycle-related gene expression was investigated to explore the potential mechanisms of how Meis1 could cause an increased vulnerability for atrial arrhythmias.

Gene expression levels of Meis1, MCM3, CCND2, Apbb1, and TP53 in the RA, RV, LA, and LV were checked by qPCR. The administration of the Meis1 inhibitor did not significantly affect Meis1 gene expression in either the RA (saline vs. Meis1 inhibitor:1.00 ± 0.12 vs. 0.95 ± 0.10, *p*=0.86, Figure 32A) or LA (saline vs. Meis1 inhibitor:1.00 ± 0.20 vs. 0.98 ± 0.15, *p*=0.98, Figure 32B); however, CCND2 gene levels were upregulated following Meis1 inhibition in both regions (in RA, saline vs. Meis1 inhibitor:1.00 ± 0.08 vs. 1.41 ± 0.12, **p* <0.05, Figure 32A; in LA, saline vs. Meis1 inhibitor:1.00 ± 0.16 vs. 1.79 ± 0.20, **p* =0.01, Figure 32B). In the RV and LV, the application of the Meis1 inhibitor did not impact the gene expression of Meis1 itself (RV, saline vs. Meis1 inhibitor: 1.00 ± 0.15 vs. 0.76 ± 0.13, *p*=0.15, Figure 32C; LV, saline vs. Meis1 inhibitor:

1.00 ± 0.13 vs. 0.86 ± 0.11, *p*=0.20, Figure 32D). However, the gene expression of TP53 was decreased after Meis1 inhibition, both in the RV (saline vs. Meis1 inhibitor:1.00 ± 0.11 vs. 0.70 ± 0.09, **p*<0.05, Figure 32C) and LV (saline vs. Meis1 inhibitor:1.00 ± 0.19 vs. 0.42 ± 0.06, **p*<0.05, Figure 32D).

In sum, the expression of the CCND2 gene was elevated after Meis1 inhibition in the RA and LA, and the gene expression of TP53 was decreased after Meis1 inhibition in the RV and LV.

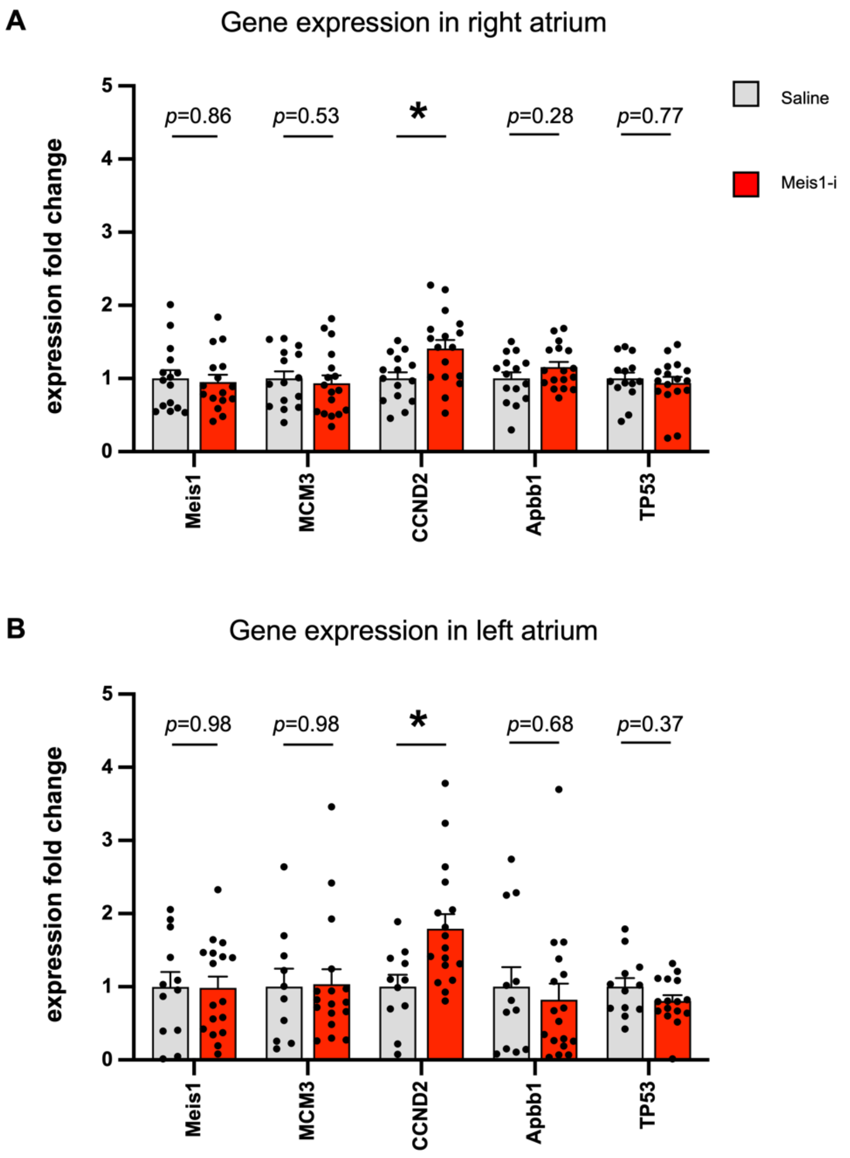

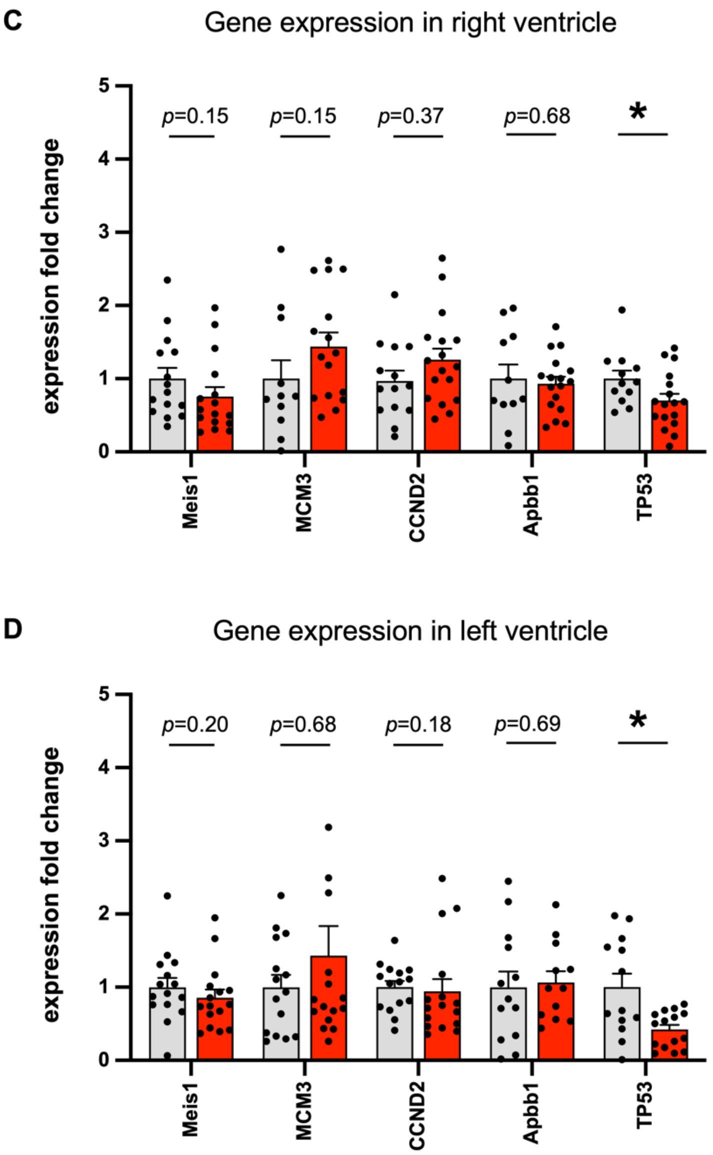

Figure 32. Gene expression of Meis1 and its target genes. Expression of Meis1 and its target genes, such as MCM3, CCND2, Apbb1, as well as TP53, in different heart chambers. (A) Gene expression in RA. (B) Gene expression in LA. (C) Gene expression in RV. (D) Gene expression in LV. Data were presented as mean ± SEM, with individual murine data points indicated by grey circles. Between-group comparisons were evaluated using the Mann-Whitney- U test. **p*<0.05. Meis1-i represents the Meis1-inhibitor group.

3.9 The effect of Meis1 inhibition on cell proliferation

The influence of Meis1 inhibition on cell proliferation in the RA was investigated by immunofluorescence staining of the proliferation marker Ki67. The percentages were determined by the number of double-positive cells divided by number of nuclei. Meis1 inhibitor-treated mice exhibited a markedly elevated proportion Ki67 and desmin double positive cardiomyocytes in the RA compared to controls (saline vs. Meis1 inhibitor: 0.51% ± 0.28 vs. 1.53% ± 0.25, *$p<0.05$, Figure 33A). No notable variations were observed in the percentage of Ki67 and vimentin double-positive fibroblasts in the RA between the two groups (saline vs. Meis1 inhibitor: 16.94% ± 11.17 vs. 15.32% ±7.31, $p=0.90$, Figure 33B). No substantial difference was observed in the percentage of Ki67 and CD64 double-positive macrophages in the RA between the Meis1 inhibitor- and saline-treated mice (saline vs. Meis1 inhibitor: 4.29% ± 1.62 vs. 3.54% ± 1.64, $p=0.32$, Figure 33C).

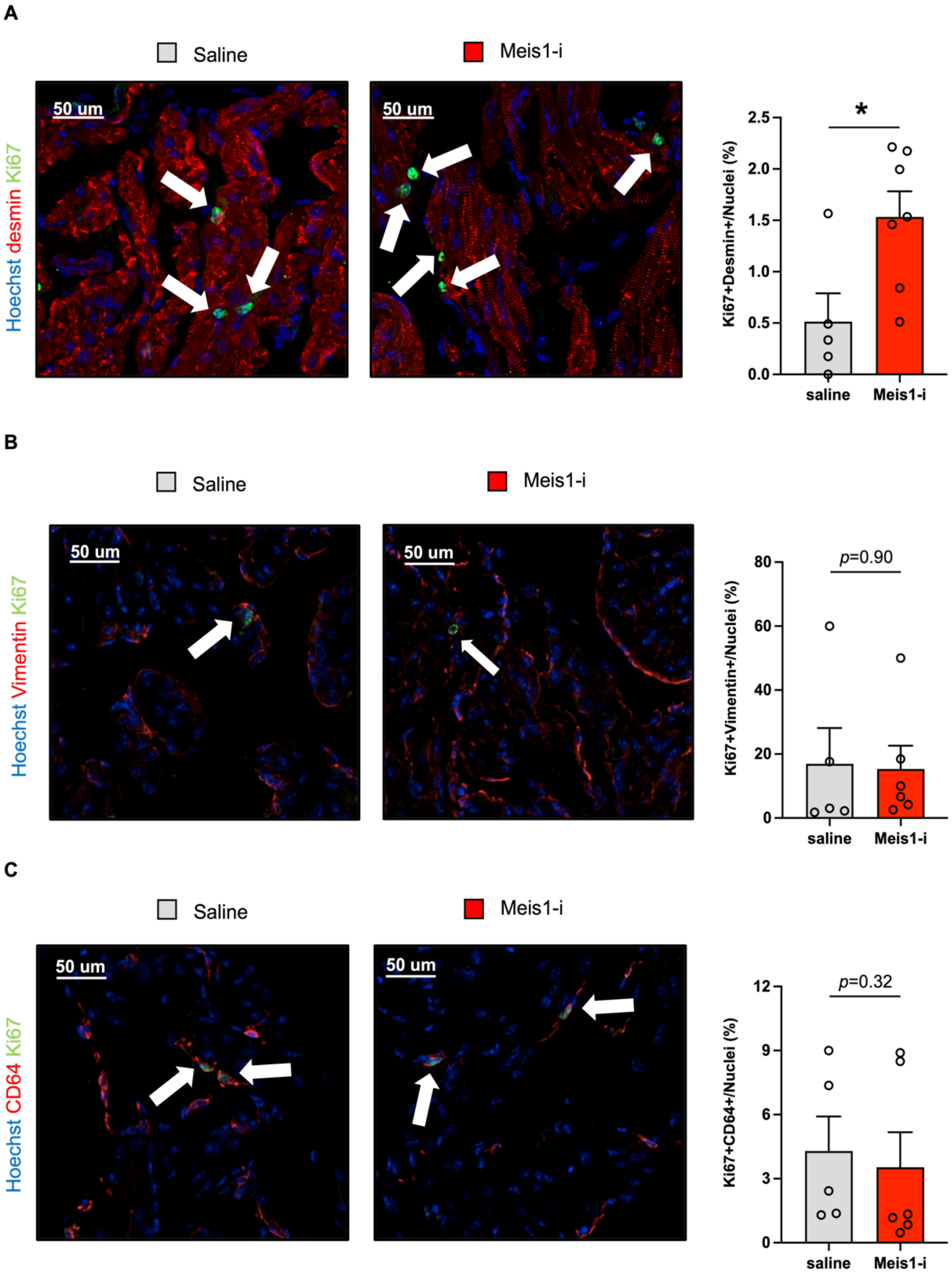

Figure 33. Immunofluorescence staining of Ki67. Immunofluorescence staining of Ki67 in RA. (A) Multi-staining of Ki67 (green) and desmin (red) and percentage of double-positive cardiomyocytes in both the saline-treated and Meis1 inhibitor-treated groups of mice. The white arrows indicate the presence of Ki67-positive cardiomyocytes. (B) Multi-staining of Ki67 (green) and vimentin (red). The white arrows indicate the presence of Ki67-positive fibroblasts. (C) Multi-staining of Ki67 (green) and CD64 (red). The white arrows indicate the presence of Ki67-positive macrophages. Data were shown as mean ± SEM, with individual animal measurements depicted as gray data points. Between-group comparisons were analyzed using the Mann-Whitney U test. *$p<0.05$. Meis1-i represents the Meis1-inhibitor group.

4. Discussion

In the present study, cardiac dimensions and systolic function were unaffected by Meis1 inhibition. However, Meis1 inhibition affected sinus node function and atrial conduction. In addition, Meis1 inhibition resulted in an increased susceptibility for atrial arrhythmias. Gene profiling linked atrial arrhythmias to impaired cell cycle regulation in cardiomyocytes.

4.1 Mouse models in EP research

In the present study, the Meis1-inhibited mouse model was established by intraperitoneally injecting the Meis1 inhibitor into BALB/c mice on days 1, 4, and 7. Mouse models are now widely used in EP studies to investigate arrhythmia mechanisms at genetic and molecular levels (Tomsits et al., 2023). Although the small size of the mouse heart poses challenges for certain investigations, such as invasive EP studies, the mouse model remains a valuable tool in cardiovascular research. Beyond the anatomical similarity of having four chambers (Wessels and Sedmera, 2003), mice offer several advantages, including the ability to generate genetically modified strains, rapid reproduction cycles, and the availability of well-established techniques for cardiac phenotyping (Clauss et al., 2019). Furthermore, novel drug candidates such as the Meis1 inhibitor used in this study, can be easily tested in mice since comparable low amounts of drug are needed. These features make mice particularly suitable for studying the molecular and genetic basis of cardiac disorders. The Meis1 inhibition mouse model has specific advantages for the present study, such as the availability of validated inhibitors and their rapid establishment within 10 days. Turan *et al*. demonstrated reduced expression of Meis1 and associated targets such as hypoxia-inducible factor 1-alpha (Hif-1α), Hif-2α, and hematopoietic stem cell quiescence modulators following Meis1 inhibitor administration in whole bone marrow isolates (Turan et al., 2020). Furthermore, it is not recommended to directly apply a novel inhibitor to large animals due to insufficient knowledge about its effects. Moreover, the production of the inhibitor can not be readily expanded on a large scale. Thus, in this study, it is ideal to choose a mouse model.

Furthermore, the present telemetry study examined the impact of Meis1 inhibition on cardiac EP over a duration of 30 days of ECG recording. Implantable telemetric ECG systems enable prolonged electrophysiological assessment in freely behaving mice, supporting months-long continuous recordings (Tomsits et al., 2021). Telemetry's key strength is permitting long-term Meis1 inhibition evaluation devoid of anesthetic confounds.

4.2 Effects of Meis1 inhibition on cardiac structure and function

Echocardiographic analysis revealed no significant alterations in LVID, IVS, LVPW, EF, or LA diameter following Meis1 inhibition, suggesting preserved cardiac architecture and performance. The findings align with Mahmoud *et al.*'s report of preserved cardiac function, as evidenced by unaltered EF and fractional shortening in mice with cardiomyocyte-specific Meis1 knockout (Mahmoud et al., 2013). Furthermore, Bouilloux *et al.* also observed that cardiac function was unaffected, as evidenced by the unchanged EF in a mouse model with specific inactivation of Meis1 in the peripheral nervous system (Bouilloux et al., 2016). The unchanged parameters suggest that alterations in cardiac structure and function are not the underlying cause of Meis1 inhibition-induced atrial arrhythmias.

4.3 Effects of Meis1 inhibition on cardiac EP

4.3.1 Effects of Meis1 inhibition on sinus node function

Invasive EP studies aim to assess conduction system functionality and elucidate arrhythmogenic mechanisms (Majeed and Sattar, 2021). The findings of this study revealed that Meis1 inhibition significantly impacts sinus node function, as evidenced by prolonged SNRT. The observed prolongation of SNRT and its potential contribution to arrhythmogenesis may be explained by altered gene expression. Meis1 inhibition potentially affects sinus node gene regulatory programs. Meis1 serves as a crucial transcriptional regulator in cardiac conduction system development, directly modulating the expression of key ion channels and gap junction proteins essential for proper electrical conduction (Muñoz-Martín et al., 2024, Crespo-García et al., 2022). Inhibition of Meis1 may disrupt the normal expression of these proteins, leading to impaired electrical conduction and increased susceptibility to arrhythmias. Furthermore, transcriptomic analyses of cardiomyocyte-specific Meis1/Meis2 knockout models reveal activation of multiple signaling pathways, including gap junction remodeling and Wnt signaling cascades (Muñoz-Martín et al., 2024). These molecular alterations may represent the underlying mechanisms by which Meis1 inhibition induces or promotes arrhythmogenesis.

While Meis1 inhibition significantly prolonged SNRT, the absence of observable effects on sinus pause incidence and heart rate in conscious mice may be explained by several factors. First, The modest cohort size (n=4 per group) potentially reduces statistical power for identifying significant variations in these intermittent phenomena. Second, intrinsic biological variability in sinus node function-including circadian rhythm fluctuations and individual differences in autonomic tone-may mask treatment effects (Boukens et al., 2014). Future studies with larger sample sizes and more detailed electrophysiological assessments may provide further insights into the effects of Meis1 inhibition on sinus node function.

4.3.2 Meis1 inhibition on AV node function

A GWAS meta-analysis of seven European cohorts identified a variant at chromosome 2 within the gene Meis1 significantly correlated with PR interval duration, suggesting its involvement in cardiac conduction regulation (Pfeufer et al., 2010). To study the influence of Meis1 inhibition on fundamental cardiac conduction properties, surface ECGs were recorded. In the present study, the PR interval was significantly prolonged by Meis1 inhibition, indicating impaired AV conduction (Bagliani et al., 2017). To further investigate the influence of Meis1 on cardiac EP without the influence of anesthesia, mice were equipped with implantable telemetry devices to monitor the ECG during daytime and nighttime recordings. The analysis of the telemetry data also showed a prolonged PR interval by Meis1 inhibition on the tenth day during nighttime recording. The PR interval reflects atrial depolarization and subsequent impulse conduction through the AVN to the ventricular conduction system (Sanjeev Saksena, 2004). As a mediator between atrial EP and AF risk, the PR interval reflects changes in atrial APD and AV conduction, which jointly impact AF development (Olsson et al., 1971). Cheng *et al*. reported in a FHS prospective analysis that subjects with a PR interval exceeding 200 ms exhibited a two-fold higher adjusted risk of AF (Cheng et al., 2009). Similarly, Soliman *et al*. found in the Atherosclerosis Risk in Communities (ARIC) study, involving 15249 participants, that prolonged PR interval was an independent predictor of AF incidence (Soliman et al., 2009). Extended PR interval was observed in other transgenic mouse models showing arrhythmias. For instance, ECG telemetry showed that specific deletion of the basic helix-loop-helix transcription factor Bmal1 in cardiomyocytes of adult mice resulted in a prolongation of the PR interval and an increased number of arrhythmia episodes (Schroder et al., 2013). Furthermore, in C57BL/6J mice, a notable increase in the PR interval and an elevated susceptibility to inducible ventricular arrhythmia caused by programmed electrical stimulation was observed after acute exposure to phenanthrene (Yaar et al., 2023). However, Meis1 inhibition did not have an impact on the AV conduction, as evidenced by the unchanged Wenckebach cycle length, 2:1 cycle length, and VA conduction. This discrepancy between surface ECG findings and invasive EP measurements may be attributed to several factors. Surface ECG recordings mainly provide global electrical activity and may be affected by atrial conduction characteristics, whereas invasive EP offers more specific and direct measures, especially in evaluating AVN function (Zipes, 2018). A more comprehensive understanding of how Meis1 inhibition influences atrial and AV conduction physiology remains to be established through subsequent research.

4.3.3 Meis1 inhibition on ventricular conduction

The current investigation demonstrated that the administration of the Meis1 inhibitor did not affect QRS duration, QTc interval, or VERP. The preservation of normal QRS complex duration and QTc interval suggests that Meis1 suppression does not significantly influence ventricular conduction velocity or repolarization dynamics, as these electrocardiographic markers specifically represent ventricular depolarization and repolarization processes (Oknińska et al., 2022). This observation is consistent with previous work by Bouilloux *et al*. (2016), who found that conditional Meis1 knockout in the peripheral nervous system of PLATCRE:Meis1LoxP/LoxP mice had no measurable effect on key ECG indices, including QRS duration and corrected QT interval (Bouilloux et al., 2016).

4.4 Effects of Meis1 inhibition on atrial arrhythmogenesis

The administration of the Meis1 inhibitor increased the susceptibility to atrial arrhythmias, and this effect was strongly validated through both the proportion of animals and the proportion of stimulations leading to arrhythmia episodes. The above findings indicate a potential role for Meis1 in arrhythmogenesis.

The prolonged AERP observed in mice administered with the Meis1 inhibitor indicates that Meis1 inhibition altered atrial conduction. Research in animal models indicates that a reduction in AERP correlates with enhanced AF stability and prolonged duration of AF paroxysms (Wijffels et al., 1995). Current studies have not specifically addressed the consequences of Meis1 inhibition on atrial arrhythmia initiation and maintenance, despite clear evidence of its participation in ventricular arrhythmogenic processes (Liu et al., 2022). The observed effects of Meis1 on both ventricular conduction and atrial refractoriness suggest potential, but currently unexplored, mechanisms by which Meis1 might contribute to atrial rhythm disturbances.

Possible mechanisms underlying Meis1 inhibition-induced atrial arrhythmogenesis may involve two primary pathways: (1) Ion channel remodeling. Meis1 regulates sodium channel (NaV1.5) expression and current density, critical determinants of cardiac excitability and conduction velocity (Liu et al., 2022; Gaborit et al., 2005), with potential cascading effects on potassium and calcium currents that coordinate cardiac repolarization (Jeevaratnam et al., 2018); (2) Gap junction dysregulation. Meis1 may modulate connexin 40/43 expression, as abnormal connexin patterning disrupts intercellular coupling and impulse propagation, a hallmark of atrial fibrillation (Jansen et al., 2010, Lawrence et al., 1978). Although extrapolation from ventricular arrhythmia mechanisms provides theoretical support, experimental confirmation using atrial-specific experimental systems is critically required.

Meis1 exhibits pleiotropic functions across multiple biological systems, including developmental processes, stem cell maintenance, oncogenic transformation, and cardiac tissue repair (Liu et al., 2022). Particularly in cardiac autonomic regulation, Meis1 serves as a crucial modulator of sympathetic neuronal development and function-key determinants of proper cardiac innervation and physiological homeostasis (Bouilloux et al., 2016). Conditional knockout studies in murine peripheral nervous systems revealed Meis1's selective impact on sympathetic-mediated cardiac modulation, with preserved parasympathetic activity (Bouilloux et al., 2016). The current telemetric assessments further support this specificity, demonstrating that Meis1 inhibition maintains normal time- and frequency-domain parameters, indicating potential preservation of autonomic balance among the parasympathetic nervous system (PNS) and the sympathetic nervous system (SNS). However, the discrepancy between the preserved autonomic balance in the current study and the more pronounced sympathetic dysregulation reported by Bouilloux et al. could be due to differences in sample size and mouse strains. For instance, the current study employs a sample size of only 4 mice per group, which might be insufficient to fully capture the true phenotypic manifestations. Furthermore, while BALB/c mice were used in the current study, the aforementioned study employed a cross between the PLATCRE strain and Meis1 LoxP/LoxP mice. Such strain-specific variations could potentially contribute to the observed phenotypic differences.

4.5 Effects of Meis1 on cell cycle and proliferation

The present investigation employed qPCR to quantify expression alterations in Meis1 and its direct transcriptional targets involved in cell cycle control, including MCM3, CCND2, Apbb1, and TP53, following treatment with the Meis1 inhibitor (Mahmoud et al., 2013). The results showed that the Meis1 inhibitor had no effect on Meis1 gene expression. The Meis1 inhibitor acts on the protein level without the half-life of the protein. Therefore, a feedback loop that could alter the gene expression of Meis1 is unlikely.

Conversely, in the current qPCR, the administration of Meis1 inhibitors substantially enhanced the expression of CCND2, a crucial regulator of the cell cycle (Chiles, 2004), in both RA and LA. The Meis1 inhibitor caused a decrease in TP53 in RV and LV, which is a protein that negatively regulates the cell cycle (Engeland, 2022). These results corroborate earlier observations by Mahmoud *et al*. (Mahmoud et al., 2013), who demonstrated that genetic ablation of Meis1 differentially modulates cell cycle regulatory networks. Their work revealed upregulation of pro-proliferative factors (CHEK1, CCND2, MCM3) concurrent with downregulation of cell cycle inhibitors (Apbb1, TP53, GPR132). Of particular significance is CCND2, which plays a pivotal role in cell cycle progression through CDK4/6-mediated RB phosphorylation and subsequent inhibition of p21Waf1/Cip1 and p27Kip1 (Shaw, 1996, Busk et al., 2005). Increased promotion of the cardiomyocyte cell cycle could decrease sarcomere stability and elevate the risk of arrhythmias (Gabisonia et al., 2019). TP53 is recognized for its crucial involvement in inhibiting the progression of cancer and regulating the cell cycle (Levine, 1997, Shaw, 1996). After TP53 is activated, the expression of p21 is increased. Elevated p21 levels promote RB-E2F complex stabilization, ultimately repressing transcriptional activation of multiple cell cycle-related genes (Engeland, 2022). Cell cycle arrest occurs due to the decreased expression of multiple regulators (Engeland, 2022). TP53 also inhibits the expression of cyclin A, which serves as another obstacle that blocks cell cycle progression into and through the S phase (Shaw, 1996). Arrhythmogenic cardiomyopathy is associated with activation of the EP300/TP53 pathway, characterized by increased EP300 protein levels, which drive elevated acetylation (K382) and phosphorylation (S15) of TP53, thereby activating the pathway (Rouhi et al., 2022).

Research by Mahmoud *et al*. established Meis1 as a master regulator of cardiomyocyte proliferation control. Their genetic studies demonstrated that both constitutive and conditional knockout of Meis1 in cardiomyocytes significantly extended the postnatal window of cardiac myocyte proliferation (Mahmoud et al., 2013). Conversely, Meis1 overexpression inhibited cardiomyocyte proliferation in newborn mice following MI. Similarly, the present investigation revealed that Meis1 inhibition markedly enhanced cardiomyocyte proliferation, indicating that the increased proliferation may contribute to atrial arrhythmias associated with Meis1 inhibition. While no direct evidence currently links Meis1 inhibition-induced cardiomyocyte proliferation to atrial arrhythmogenesis, several indirect mechanisms may potentially mediate this association. For instance, proliferating cardiomyocytes undergo significant alterations in cell cycle regulators, growth factors and cytokines, global and locus-specific epigenetic changes, and cellular metabolism, all of which may disrupt cardiac electrophysiology and potentially trigger arrhythmias (Yuan and Braun, 2017). Additionally, a critical factor is that cardiomyocyte proliferation signifies cell cycle re-entry (Ahuja et al., 2007), which may lead to dysregulation of calcium signaling (Humeau et al., 2018). The fundamental importance of calcium signaling in cardiac electrophysiological regulation (Landstrom et al., 2017) suggests that impaired calcium homeostasis may represent a significant arrhythmogenic substrate.

5. Summary

This study examined Meis1's impact on cardiac EP and arrhythmogenesis, exploring its mechanistic basis. In order to achieve this objective, a mouse model with Meis1 inhibition was created by injecting a Meis1 inhibitor into BALB/c mice. The study aimed to evaluate the influence of Meis1 on cardiac EP and arrhythmogenesis by examining cardiac structure and function, electrophysiological characteristics, HRV in both time and frequency domains, and the occurrence of atrial arrhythmias. Gene level of Meis1 and its downstream targets implicated in cell cycle regulation and proliferative control of cardiomyocytes, fibroblasts, and macrophages were analyzed to clarify the molecular principles that underlie these processes. The administration of the Meis1 inhibitor increased the SNRT and AERP, as well as the inducibility of atrial arrhythmias. These findings indicate that Meis1 inhibition alters sinus node activity, atrial conduction properties, and atrial arrhythmia susceptibility. Notably, differential regulation of CCND2 (atria) and TP53 (ventricle), coupled with enhanced cardiomyocyte proliferation, implicates cell cycle dysregulation as a potential arrhythmogenic mechanism following Meis1 suppression. Collectively, these data establish Meis1 as a key modulator of cardiac EP and atrial arrhythmogenesis, potentially through cardiomyocyte cell cycle control.

6. Outlook

The mouse model developed in this study can serve as a powerful tool for further research on cardiac EP and arrhythmias. The discovery of Meis1 as a crucial factor in cardiac EP provides new opportunities for therapeutic intervention. Pharmacologically manipulating Meis1 could potentially be utilized to control or prevent arrhythmias in patients. While this study provides important insights, there are questions that require further investigation. Additional investigations are needed to delineate the exact pathways through which Meis1 inhibition promotes arrhythmogenesis via cardiomyocyte proliferative mechanisms. Comprehensive characterization of Meis1-CCND2/TP53 regulatory networks will provide critical insights into its cell cycle modulatory functions. Furthermore, elucidating Meis1's regulatory effects on cardiac ion channel expression and function and its contribution to fibrotic remodeling will be crucial for understanding its pathophysiological role in cardiac EP and arrhythmogenesis. Several study limitations warrant consideration in future investigations. For instance, the generalizability of the findings may be limited by the use of BALB/c mice. Future validation studies should employ additional genetic models, including cardiomyocyte-specific Meis1 knockout mice, to confirm these findings.

References

ABD-ELSALAM, K. A. 2003. Bioinformatic tools and guideline for PCR primer design. *african Journal of biotechnology,* 2**,** 91-95.

AHUJA, P., SDEK, P. & MACLELLAN, W. R. 2007. Cardiac myocyte cell cycle control in development, disease, and regeneration. *Physiological reviews,* 87**,** 521-544.

ALLESSIE, M. A., DE GROOT, N. M., HOUBEN, R. P., SCHOTTEN, U., BOERSMA, E., SMEETS, J. L. & CRIJNS, H. J. 2010. Electropathological substrate of long-standing persistent atrial fibrillation in patients with structural heart disease: longitudinal dissociation. *Circulation: Arrhythmia and Electrophysiology,* 3**,** 606-615.

ANDRÁS, V., TOMEK, J., NAGY, N., VIRÁG, L., PASSINI, E., RODRIGUEZ, B. & BACZKÓ, I. 2021. Cardiac transmembrane ion channels and action potentials: cellular physiology and arrhythmogenic behavior. *Physiological reviews*.

BAGLIANI, G., DELLA ROCCA, D. G., DI BIASE, L. & PADELETTI, L. 2017. PR interval and junctional zone. *Card Electrophysiol Clin,* 9**,** 411-433.

BOSCH, R. F., ZENG, X., GRAMMER, J. B., POPOVIC, K., MEWIS, C. & KÜHLKAMP, V. 1999. Ionic mechanisms of electrical remodeling in human atrial fibrillation. *Cardiovascular research,* 44**,** 121-131.

BOUILLOUX, F., THIREAU, J., VENTEO, S., FARAH, C., KARAM, S., DAUVILLIERS, Y., VALMIER, J., COPELAND, N. G., JENKINS, N. A. & RICHARD, S. 2016. Loss of the transcription factor Meis1 prevents sympathetic neurons target-field innervation and increases susceptibility to sudden cardiac death. *Elife,* 5**,** e11627.

BOUKENS, B. J., RIVAUD, M. R., RENTSCHLER, S. & CORONEL, R. 2014. Misinterpretation of the mouse ECG:'musing the waves of Mus musculus'. *The Journal of physiology,* 592**,** 4613-4626.

BUSK, P. K., HINRICHSEN, R., BARTKOVA, J., HANSEN, A. H., CHRISTOFFERSEN, T. E., BARTEK, J. & HAUNSØ, S. 2005. Cyclin D2 induces proliferation of cardiac myocytes and represses hypertrophy. *Experimental cell research,* 304**,** 149-161.

CEPIEL, A., NOSZCZYK-NOWAK, A., PASŁAWSKI, R., JANISZEWSKI, A. & PASŁAWSKA, U. 2017. Intracardiac electrophysiological conduction parameters in adult dogs. *Veterinary Quarterly,* 37**,** 91-97.

CHENG, S., KEYES, M. J., LARSON, M. G., MCCABE, E. L., NEWTON-CHEH, C., LEVY, D., BENJAMIN, E. J., VASAN, R. S. & WANG, T. J. 2009. Long-term outcomes in individuals with prolonged PR interval or first-degree atrioventricular block. *Jama,* 301**,** 2571-2577.

CHIANG, C.-E., WANG, K.-L. & LIP, G. Y. 2014. Stroke prevention in atrial fibrillation: an Asian perspective. *Thrombosis and haemostasis,* 112**,** 789-797.

CHILES, T. C. 2004. Regulation and function of cyclin D2 in B lymphocyte subsets. *The Journal of Immunology,* 173**,** 2901-2907.

CLAUSS, S., BLEYER, C., SCHUETTLER, D., TOMSITS, P., RENNER, S., KLYMIUK, N., WAKILI, R., MASSBERG, S., WOLF, E. & KÄÄB, S. 2019. Animal models of arrhythmia: classic electrophysiology to genetically modified large animals. *Nature Reviews Cardiology,* 16**,** 457-475.

COSEDIS NIELSEN, J., JOHANNESSEN, A., RAATIKAINEN, P., HINDRICKS, G., WALFRIDSSON, H., KONGSTAD, O., PEHRSON, S., ENGLUND, A., HARTIKAINEN, J. & MORTENSEN, L. S. 2012. Radiofrequency ablation as initial therapy in paroxysmal atrial fibrillation. *New England Journal of Medicine,* 367**,** 1587-1595.

CRESPO-GARCÍA, T., CÁMARA-CHECA, A., DAGO, M., RUBIO-ALARCÓN, M., RAPÚN, J., TAMARGO, J., DELPÓN, E., CABALLERO, R. & INVESTIGATORS, I. 2022. Regulation of cardiac ion channels by transcription factors: Looking for new opportunities of druggable targets for the treatment of arrhythmias. *Biochemical Pharmacology,* 204**,** 115206.

DA COSTA, D., BRADY, W. J. & EDHOUSE, J. 2002. Bradycardias and atrioventricular conduction block. *Bmj,* 324**,** 535-538.

DIEFFENBACH, C., LOWE, T. & DVEKSLER, G. 1993. General concepts for PCR primer design. *PCR methods appl,* 3**,** S30-S37.

ECKSTEIN, J., MAESEN, B., LINZ, D., ZEEMERING, S., VAN HUNNIK, A., VERHEULE, S., ALLESSIE, M. & SCHOTTEN, U. 2011. Time course and mechanisms of endo-epicardial electrical dissociation during atrial fibrillation in the goat. *Cardiovascular research,* 89**,** 816-824.

ENGELAND, K. 2022. Cell cycle regulation: p53-p21-RB signaling. *Cell Death & Differentiation,* 29**,** 946-960.

ESCUDERO-MARTINEZ, I., MORALES-CABA, L. & SEGURA, T. 2023. Atrial fibrillation and stroke: A review and new insights. *Trends in Cardiovascular Medicine,* 33**,** 23-29.

FEGHALY, J., ZAKKA, P., LONDON, B., MACRAE, C. A. & REFAAT, M. M. 2018. Genetics of atrial fibrillation. *Journal of the American Heart Association,* 7**,** e009884.

FOZZARD, H. A. 2002. Cardiac sodium and calcium channels: a history of excitatory currents. *Cardiovascular research,* 55**,** 1-8.

GABISONIA, K., PROSDOCIMO, G., AQUARO, G. D., CARLUCCI, L., ZENTILIN, L., SECCO, I., ALI, H., BRAGA, L., GORGODZE, N. & BERNINI, F. 2019. MicroRNA therapy stimulates uncontrolled cardiac repair after myocardial infarction in pigs. *Nature,* 569**,** 418-422.

GABORIT, N., STEENMAN, M., LAMIRAULT, G., LE MEUR, N., LE BOUTER, S., LANDE, G., LÉGER, J., CHARPENTIER, F., CHRIST, T. & DOBREV, D. 2005. Human atrial ion channel and transporter subunit gene-expression remodeling associated with valvular heart disease and atrial fibrillation. *Circulation,* 112**,** 471-481.

GEERTS, D., SCHILDERINK, N., JORRITSMA, G. & VERSTEEG, R. 2003. The role of the MEIS homeobox genes in neuroblastoma. *Cancer letters,* 197**,** 87-92.

GO, A. S., HYLEK, E. M., PHILLIPS, K. A., CHANG, Y., HENAULT, L. E., SELBY, J. V. & SINGER, D. E. 2001. Prevalence of diagnosed atrial fibrillation in adults: national implications for rhythm management and stroke prevention: the AnTicoagulation and Risk Factors in Atrial Fibrillation (ATRIA) Study. *Jama,* 285**,** 2370-2375.

GRANT, A. O. 2009. Cardiac ion channels. *Circulation: Arrhythmia and Electrophysiology,* 2**,** 185-194.

GRUNNET, M., HANSEN, R. S. & OLESEN, S.-P. 2008. hERG1 channel activators: a new anti-arrhythmic principle. *Progress in biophysics and molecular biology,* 98**,** 347-362.

HEIJMAN, J., VOIGT, N., NATTEL, S. & DOBREV, D. 2014. Cellular and molecular electrophysiology of atrial fibrillation initiation, maintenance, and progression. *Circulation research,* 114**,** 1483-1499.

HJERTEAVDELINGEN, U. 2016. 2016 ESC Guidelines for the management of atrial fibrillation developed in collaboration with EACTS. *European Heart Journal,* 37.

HULSMANS, M., CLAUSS, S., XIAO, L., AGUIRRE, A. D., KING, K. R., HANLEY, A., HUCKER, W. J., WÜLFERS, E. M., SEEMANN, G. & COURTIES, G. 2017. Macrophages facilitate electrical conduction in the heart. *Cell,* 169**,** 510-522. e20.

HUMEAU, J., BRAVO-SAN PEDRO, J. M., VITALE, I., NUNEZ, L., VILLALOBOS, C., KROEMER, G. & SENOVILLA, L. 2018. Calcium signaling and cell cycle: Progression or death. *Cell calcium,* 70**,** 3-15.

ISRAELS, E. & ISRAELS, L. 2000. The cell cycle. *The oncologist,* 5**,** 510-513.

IWASAKI, Y.-K., NISHIDA, K., KATO, T. & NATTEL, S. 2011. Atrial fibrillation pathophysiology: implications for management. *Circulation,* 124**,** 2264-2274.

JANSEN, J. A., VAN VEEN, T. A., DE BAKKER, J. M. & VAN RIJEN, H. V. 2010. Cardiac connexins and impulse propagation. *J Mol Cell Cardiol,* 48**,** 76-82.

JEEVARATNAM, K., CHADDA, K. R., HUANG, C. L. & CAMM, A. J. 2018. Cardiac Potassium Channels: Physiological Insights for Targeted Therapy. *J Cardiovasc Pharmacol Ther,* 23**,** 119-129.

JIANG, M., XU, S., BAI, M. & ZHANG, A. 2021. The emerging role of MEIS1 in cell proliferation and differentiation. *American Journal of Physiology-Cell Physiology,* 320**,** C264-C269.

JOHNSON, D. G. & WALKER, C. L. 1999. Cyclins and cell cycle checkpoints. *Annual review of pharmacology and toxicology,* 39**,** 295-312.

KAESE, S. & VERHEULE, S. 2012. Cardiac electrophysiology in mice: a matter of size. *Frontiers in physiology,* 3**,** 29023.

KASHOU, A. H., GOYAL, A., NGUYEN, T., AHMED, I. & CHHABRA, L. 2017. Atrioventricular block.

KORNEJ, J., BÖRSCHEL, C. S., BENJAMIN, E. J. & SCHNABEL, R. B. 2020. Epidemiology of atrial fibrillation in the 21st century: novel methods and new insights. *Circulation research,* 127**,** 4-20.

LANDSTROM, A. P., DOBREV, D. & WEHRENS, X. H. 2017. Calcium signaling and cardiac arrhythmias. *Circulation research,* 120**,** 1969-1993.

LAWRENCE, T. S., BEERS, W. H. & GILULA, N. B. 1978. Transmission of hormonal stimulation by cell-to-cell communication. *Nature,* 272**,** 501-506.

LEVINE, A. J. 1997. p53, the cellular gatekeeper for growth and division. *cell,* 88**,** 323-331.

LI, N. & WEHRENS, X. H. 2010. Programmed electrical stimulation in mice. *JoVE (Journal of Visualized Experiments)***,** e1730.

LI, P., SUR, S. H., MISTLBERGER, R. E. & MORRIS, M. 1999. Circadian blood pressure and heart rate rhythms in mice. *American Journal of Physiology-Regulatory, Integrative and Comparative Physiology,* 276**,** R500-R504.

LI, W., HUANG, K., GUO, H. & CUI, G. 2014. Meis1 regulates proliferation of non-small-cell lung cancer cells. *Journal of thoracic disease,* 6**,** 850.

LIPPI, G., SANCHIS-GOMAR, F. & CERVELLIN, G. 2021. Global epidemiology of atrial fibrillation: an increasing epidemic and public health challenge. *International Journal of Stroke,* 16**,** 217-221.

LIU, Y., LI, J., XU, N., YU, H., GONG, L., LI, Q., YANG, Z., LI, S., YANG, J. & HUANG, D. 2022. Transcription factor Meis1 act as a new regulator of ischemic arrhythmias in mice. *Journal of Advanced Research,* 39**,** 275-289.

MAGUIRE, C. T., BEVILACQUA, L. M., WAKIMOTO, H., GEHRMANN, J. & BERUL, C. I. 2000. Maturational atrioventricular nodal physiology in the mouse. *Journal of cardiovascular electrophysiology,* 11**,** 557-564.

MAHMOUD, A. I., KOCABAS, F., MURALIDHAR, S. A., KIMURA, W., KOURA, A. S., THET, S., PORRELLO, E. R. & SADEK, H. A. 2013. Meis1 regulates postnatal cardiomyocyte cell cycle arrest. *Nature,* 497**,** 249-253.

MAJEED, H. & SATTAR, Y. 2021. Electrophysiologic Study Indications and Evaluation.

MANDAPATI, R., SKANES, A., CHEN, J., BERENFELD, O. & JALIFE, J. 2000. Stable microreentrant sources as a mechanism of atrial fibrillation in the isolated sheep heart. *Circulation,* 101**,** 194-199.

MASON, F. E., PRONTO, J. R. D., ALHUSSINI, K., MAACK, C. & VOIGT, N. 2020. Cellular and mitochondrial mechanisms of atrial fibrillation. *Basic research in cardiology,* 115**,** 72.

MITCHELL, G. F., JERON, A. & KOREN, G. 1998. Measurement of heart rate and QT interval in the conscious mouse. *American Journal of Physiology-Heart and Circulatory Physiology,* 274**,** H747-H751.

MIYASAKA, Y., BARNES, M. E., GERSH, B. J., CHA, S. S., BAILEY, K. R., ABHAYARATNA, W. P., SEWARD, J. B. & TSANG, T. S. 2006. Secular trends in incidence of atrial fibrillation in Olmsted County, Minnesota, 1980 to 2000, and implications on the projections for future prevalence. *Circulation,* 114**,** 119-125.

MOE, G. & ABILDSKOV, J. 1959. Atrial fibrillation as a self-sustaining arrhythmia independent of focal discharge. *American heart journal,* 58**,** 59-70.

MONT, L., BISBAL, F., HERNÁNDEZ-MADRID, A., PEREZ-CASTELLANO, N., VIÑOLAS, X., ARENAL, A., ARRIBAS, F., FERNANDEZ-LOZANO, I., BODEGAS, A. & COBOS, A. 2014. Catheter ablation vs. antiarrhythmic drug treatment of persistent atrial fibrillation: a multicentre, randomized, controlled trial (SARA study). *European heart journal,* 35**,** 501-507.

MOSKOW, J. J., BULLRICH, F., HUEBNER, K., DAAR, I. O. & BUCHBERG, A. M. 1995. Meis1, a PBX1-related homeobox gene involved in myeloid leukemia in BXH-2 mice. *Molecular and Cellular Biology,* 15**,** 5434-5443.

MUÑOZ-MARTÍN, N., SIMON-CHICA, A., DÍAZ-DÍAZ, C., CADENAS, V., TEMIÑO, S., ESTEBAN, I., LUDWIG, A., SCHORMAIR, B., WINKELMANN, J. & OLEJNICKOVA, V. 2024. Meis transcription factors regulate cardiac conduction system development and adult function. *Cardiovascular Research***,** cvae258.

NASI ‐ ER, B. G., WENHUI, Z., HUAXIN, S., XIANHUI, Z., YAODONG, L., YANMEI, L., HONGLI, W., TUER ‐ HONG, Z. L., QINA, Z. & BAOPENG, T. 2019. Vagus nerve stimulation reduces ventricular arrhythmias and increases ventricular electrical stability. *Pacing and Clinical Electrophysiology,* 42**,** 247-256.

NATTEL, S. 2002. New ideas about atrial fibrillation 50 years on. *Nature,* 415**,** 219-226.

NATTEL, S. & HARADA, M. 2014. Atrial remodeling and atrial fibrillation: recent advances and translational perspectives. *Journal of the American College of Cardiology,* 63**,** 2335-2345.

NATTEL, S., HEIJMAN, J., ZHOU, L. & DOBREV, D. 2020. Molecular basis of atrial fibrillation pathophysiology and therapy: a translational perspective. *Circulation research,* 127**,** 51-72.

NERBONNE, J. M. & KASS, R. S. 2005. Molecular physiology of cardiac repolarization. *Physiological reviews,* 85**,** 1205-1253.

OKNIŃSKA, M., MĄCZEWSKI, M. & MACKIEWICZ, U. 2022. Ventricular arrhythmias in acute myocardial ischaemia—Focus on the ageing and sex. *Ageing Research Reviews,* 81**,** 101722.

OKUMURA, K., SAITO, M., ISOGAI, E., AOTO, Y., HACHIYA, T., SAKAKIBARA, Y., KATSURAGI, Y., HIROSE, S., KOMINAMI, R. & GOITSUKA, R. 2014. Meis1 regulates epidermal stem cells and is required for skin tumorigenesis. *PLoS One,* 9**,** e102111.

OLSSON, S. B., COTOI, S. & VARNAUSKAS, E. 1971. Monophasic action potential and sinus rhythm stability after conversion of atrial fibrillation. *Acta Medica Scandinavica,* 190**,** 381-387.

PANDEY, R., YANG, Y., JACKSON, L. & AHMED, R. P. 2016. MicroRNAs regulating meis1 expression and inducing cardiomyocyte proliferation. *Cardiovascular regenerative medicine,* 3.

PAULY, V., VLCEK, J., ZHANG, Z., HESSE, N., XIA, R., BAUER, J., LOY, S., SCHNEIDER, S., RENNER, S. & WOLF, E. 2023. Effects of Sex on the Susceptibility for Atrial Fibrillation in Pigs with Ischemic Heart Failure. *Cells,* 12**,** 973.

PELLMAN, J. & SHEIKH, F. 2015. Atrial fibrillation: mechanisms, therapeutics, and future directions. *Comprehensive Physiology,* 5**,** 649.

PFEUFER, A., VAN NOORD, C., MARCIANTE, K. D., ARKING, D. E., LARSON, M. G., SMITH, A. V., TARASOV, K. V., MÜLLER, M., SOTOODEHNIA, N. & SINNER, M. F. 2010. Genome-wide association study of PR interval. *Nature genetics,* 42**,** 153-159.

POLYAKOVA, V., MIYAGAWA, S., SZALAY, Z., RISTELI, J. & KOSTIN, S. 2008. Atrial extracellular matrix remodelling in patients with atrial fibrillation. *Journal of cellular and molecular medicine,* 12**,** 189-208.

ROSKELL, N. S., SAMUEL, M., NOACK, H. & MONZ, B. U. 2013. Major bleeding in patients with atrial fibrillation receiving vitamin K antagonists: a systematic review of randomized and observational studies. *Europace,* 15**,** 787-797.

ROUHI, L., FAN, S., CHEEDIPUDI, S. M., BRAZA-BOÏLS, A., MOLINA, M. S., YAO, Y., ROBERTSON, M. J., COARFA, C., GIMENO, J. R. & MOLINA, P. 2022. The EP300/TP53 pathway, a suppressor of the Hippo and canonical WNT pathways, is activated in human hearts with arrhythmogenic cardiomyopathy in the absence of overt heart failure. *Cardiovascular Research,* 118**,** 1466-1478.

SANJEEV SAKSENA, A. J. C. 2004. *Electrophysiological Disorders of the Heart*, Elsevier Churchill Livingstone.

SANTANA, L. F., CHENG, E. P. & LEDERER, W. J. 2010. How does the shape of the cardiac action potential control calcium signaling and contraction in the heart? *Journal of molecular and cellular cardiology,* 49**,** 901.

SCHAFER, K. 1998. The cell cycle: a review. *Veterinary pathology,* 35**,** 461-478.

SCHNABEL, R. B., YIN, X., GONA, P., LARSON, M. G., BEISER, A. S., MCMANUS, D. D., NEWTON-CHEH, C., LUBITZ, S. A., MAGNANI, J. W. & ELLINOR, P. T. 2015. 50 year trends in atrial fibrillation prevalence, incidence, risk factors, and mortality in the Framingham Heart Study: a cohort study. *The Lancet,* 386**,** 154-162.

SCHRODER, E. A., LEFTA, M., ZHANG, X., BARTOS, D. C., FENG, H.-Z., ZHAO, Y., PATWARDHAN, A., JIN, J.-P., ESSER, K. A. & DELISLE, B. P. 2013. The cardiomyocyte molecular clock, regulation of Scn5a, and arrhythmia susceptibility. *American Journal of Physiology-Cell Physiology,* 304**,** C954-C965.

SCHUESSLER, R. B., GRAYSON, T. M., BROMBERG, B. I., COX, J. L. & BOINEAU, J. P. 1992. Cholinergically mediated tachyarrhythmias induced by a single extrastimulus in the isolated canine right atrium. *Circulation research,* 71**,** 1254-1267.

SCHÜTTLER, D., BAPAT, A., KÄÄB, S., LEE, K., TOMSITS, P., CLAUSS, S. & HUCKER, W. J. 2020. Animal models of atrial fibrillation. *Circulation Research,* 127**,** 91-110.

SHAFFER, F. & GINSBERG, J. P. 2017. An overview of heart rate variability metrics and norms. *Frontiers in public health***,** 258.

SHANKLAND, S. J. & WOLF, G. 2000. Cell cycle regulatory proteins in renal disease: role in hypertrophy, proliferation, and apoptosis. *American journal of physiology-Renal physiology,* 278**,** F515-F529.

SHAW, P. H. 1996. The role of p53 in cell cycle regulation. *Pathology-Research and Practice,* 192**,** 669-675.

SHIH, H.-T. 1994. Anatomy of the action potential in the heart. *Texas Heart Institute Journal,* 21**,** 30.

SOLIMAN, E. Z., PRINEAS, R. J., CASE, L. D., ZHANG, Z.-M. & GOFF JR, D. C. 2009. Ethnic distribution of ECG predictors of atrial fibrillation and its impact on understanding the ethnic distribution of ischemic stroke in the Atherosclerosis Risk in Communities (ARIC) study. *Stroke,* 40**,** 1204-1211.

STAERK, L., SHERER, J. A., KO, D., BENJAMIN, E. J. & HELM, R. H. 2017. Atrial fibrillation: epidemiology, pathophysiology, and clinical outcomes. *Circulation research,* 120**,** 1501-1517.

STEINBECK, G. & LÜDERITZ, B. 1976. Sinus node recovery time and sinoatrial conduction time. *Cardiac pacing: diagnostic and therapeutic tools.* Springer.

TANAKA, N., DALTON, N., MAO, L., ROCKMAN, H. A., PETERSON, K. L., GOTTSHALL, K. R., HUNTER, J. J., CHIEN, K. R. & ROSS, J. 1996. Transthoracic echocardiography in models of cardiac disease in the mouse. *Circulation,* 94**,** 1109-1117.

TOMSITS, P., CHATAUT, K. R., CHIVUKULA, A. S., MO, L., XIA, R., SCHÜTTLER, D. & CLAUSS, S. 2021. Analyzing Long-Term Electrocardiography Recordings to Detect Arrhythmias in Mice. *J Vis Exp*.

TOMSITS, P., CHIVUKULA, A. S., CHATAUT, K. R., SIMAHENDRA, A., WECKBACH, L. T., BRUNNER, S. & CLAUSS, S. 2022. Real-Time Electrocardiogram Monitoring during Treadmill Training in Mice. *JoVE (Journal of Visualized Experiments)***,** e63873.

TOMSITS, P., VOLZ, L., XIA, R., CHIVUKULA, A., SCHÜTTLER, D. & CLAUS, S. 2023. Medetomidine/midazolam/fentanyl narcosis alters cardiac autonomic tone leading to conduction disorders and arrhythmias in mice. *Lab Animal,* 52**,** 85-92.

TURAN, R. D., ALBAYRAK, E., USLU, M., SIYAH, P., ALYAZICI, L. Y., KALKAN, B. M., ASLAN, G. S., YUCEL, D., AKSOZ, M. & TUYSUZ, E. C. 2020. Development of Small Molecule MEIS Inhibitors that modulate HSC activity. *Scientific reports,* 10**,** 7994.

TYSON, J. J., CSIKASZ ‐ NAGY, A. & NOVAK, B. 2002. The dynamics of cell cycle regulation. *Bioessays,* 24**,** 1095-1109.

UNNISA, Z., CLARK, J. P., ROYCHOUDHURY, J., THOMAS, E., TESSAROLLO, L., COPELAND, N. G., JENKINS, N. A., GRIMES, H. L. & KUMAR, A. R. 2012. Meis1 preserves hematopoietic stem cells in mice by limiting oxidative stress. *Blood, The Journal of the American Society of Hematology,* 120**,** 4973-4981.

VANOPSTALL, C., PERIKE, S., BRECHKA, H., GILLARD, M., LAMPERIS, S., ZHU, B., BROWN, R., BHANVADIA, R. & VANDER GRIEND, D. J. 2020. MEIS-mediated suppression of human prostate cancer growth and metastasis through HOXB13-dependent regulation of proteoglycans. *Elife,* 9**,** e53600.

WAKILI, R., VOIGT, N., KÄÄB, S., DOBREV, D. & NATTEL, S. 2011. Recent advances in the molecular pathophysiology of atrial fibrillation. *The Journal of clinical investigation,* 121**,** 2955-2968.

WESSELS, A. & SEDMERA, D. 2003. Developmental anatomy of the heart: a tale of mice and man. *Physiological genomics,* 15**,** 165-176.

WIJFFELS, M. C., KIRCHHOF, C. J., DORLAND, R. & ALLESSIE, M. A. 1995. Atrial fibrillation begets atrial fibrillation: a study in awake chronically instrumented goats. *Circulation,* 92**,** 1954-1968.

WILLIAMS, A. H., LIU, N., VAN ROOIJ, E. & OLSON, E. N. 2009. MicroRNA control of muscle development and disease. *Current opinion in cell biology,* 21**,** 461-469.

WIT, A. L. 2018. Afterdepolarizations and triggered activity as a mechanism for clinical arrhythmias. *Pacing and Clinical Electrophysiology,* 41**,** 883-896.

WIT, A. L. & BOYDEN, P. A. 2007. Triggered activity and atrial fibrillation. *Heart Rhythm,* 4**,** S17-S23.

YAAR, S., FILATOVA, T. S., ENGLAND, E., KOMPELLA, S. N., HANCOX, J. C., BECHTOLD, D. A., VENETUCCI, L., ABRAMOCHKIN, D. V. & SHIELS, H. A. 2023. Global air pollutant phenanthrene and arrhythmic outcomes in a mouse model. *Environmental Health Perspectives,* 131**,** 117002.

YE, J., COULOURIS, G., ZARETSKAYA, I., CUTCUTACHE, I., ROZEN, S. & MADDEN, T. L. 2012. Primer-BLAST: a tool to design target-specific primers for polymerase chain reaction. *BMC bioinformatics,* 13**,** 1-11.

YUAN, X. & BRAUN, T. 2017. Multimodal regulation of cardiac myocyte proliferation. *Circulation research,* 121**,** 293-309.

ZHANG, Y., SI, Y. & MA, N. 2016. Meis1 promotes poly (rC) ‐ binding protein 2 expression and inhibits angiotensin II ‐ induced cardiomyocyte hypertrophy. *IUBMB life,* 68**,** 13-22.

ZIPES, D. P. 2018. *Braunwald's heart disease e-book: A textbook of cardiovascular medicine*, Elsevier Health Sciences.

Acknowledgements

I am especially grateful to my supervisor PD Dr.Sebastian Clauß for his professional and patient guidance throughout my doctoral study. When I first began studying arrhythmias and was unfamiliar with the field, he patiently led me mastering every relevant aspect of the subject. His mentorship has been invaluable; he is nice, and consistently provided me with support and constructive feedback on my research. He always encouraged me, especially when experiments did not go as planned. From him, I learned the importance of being well-prepared and organized, qualities that I believe will benefit me throughout my life.

Furthermore, I would also like to thank my thesis advisory committee members, Prof. Dr. med Christian Schulz, Prof. Dr. rer. nat. Daphne Merkus, and Prof. Dr. med. Stefan Kääb, for their insightful suggestions and comments that significantly contributed to the completion of this project. Many thanks to our project collaborator, Prof. Fatih Kocabas, who kindly provided the Meis1 inhibitor.

I am grateful to my colleagues and cooperation partners, especially Dr. Ruibing Xia and Aparna Chivukula. Ruibing greatly helped me with project understanding and thesis writing, providing numerous professional ideas. Aparna's friendship made my PhD journey enjoyable; her support in both professional and personal situations was invaluable, and I cherish our coffee times together.

My heartfelt thanks go out to all of our group members for their support and for creating a welcoming and comfortable time in our laboratory. Special thanks to Dr. Philipp Tomsits, PD Dr. Dominik Schüttler, Bianca Hildebrand, Dr. med. vet. Julia Vlcek, Valerie Pauly, Dr. med. vet. Nora Hesse, Florian Maderspacher, Kavi Chataut, Julia Bauer, Simone Loy, Dr. Zhihao Zhang, Qifang Wu, Lina Volz, Hannes Villgrater, and Katharina Buchberger.

I also extend my gratitude to other colleagues and friends who supported me over the years, including Junbo, Dr.Tianmiao Ma, Dr. Quan Zhou, Xinpei, Pengzhu, Dr. Hao Lin, and many others.

Importantly, I am deeply grateful to the China Scholarship Council (CSC) for providing me with the financial support, which enabled me to complete my doctoral studies in Germany.

Finally, I would like to thank my family members, especially my parents, Dongsheng Mo, Yuanyue Sun, and my husband Shu for their unwavering support and encouragement.

Affidavit

LMU
LUDWIG-MAXIMILIANS-UNIVERSITÄT MÜNCHEN

Dean's Office Medical Faculty
Faculty of Medicine

Affidavit

Mo, Li

Surname, first name

I hereby declare, that the submitted thesis entitled

Investigating the mechanistic role of Myeloid ecotropic insertion site 1 in atrial electrophysiology

is my own work. I have only used the sources indicated and have not made unauthorised use of services of a third party. Where the work of others has been quoted or reproduced, the source is always given.

I further declare that the dissertation presented here has not been submitted in the same or similar form to any other institution for the purpose of obtaining an academic degree.

Tianjin, 04.04.2025

Place, Date

Li Mo

Signature doctoral candidate

LMU LUDWIG-MAXIMILIANS-UNIVERSITÄT MÜNCHEN

Dean's Office Medical Faculty
Doctoral Office

Confirmation of congruency between printed and electronic version of the doctoral thesis

Mo, Li

Surname, first name

I hereby declare that the electronic version of the submitted thesis, entitled:

Investigating the mechanistic role of Myeloid ecotropic insertion site 1 in atrial electrophysiology

is congruent with the printed version both in content and format.

Tianjin, 04.04.2025

Place, Date

Li Mo

Signature doctoral candidate

List of publications

Original papers:

1. Aynura M., Galip S.A., **Mo, L.**, Qifang Wu., Sebastian C., Fatih K., Mechanistic insights into cardiac regeneration and protection through MEIS inhibition. Turkish Journal of Biology. 2024, 48(6): 414-431.
2. Bauer, J., Vlcek, J., Pauly, V., Hesse, N., Xia, R., **Mo, L**., Chivukula, A.S., Villgrater, H., Dressler, M., Hildebrand, B. and Wolf, E., 2024. Biomarker Periodic Repolarization Dynamics Indicates Enhanced Risk for Arrhythmias and Sudden Cardiac Death in Myocardial Infarction in Pigs. Journal of the American Heart Association, 13(9), p.e032405.
3. Tomsits, P., Chataut, K.R., Chivukula, A.S., **Mo, L**., Xia, R., Schüttler, D. and Clauss, S., 2021. Analyzing long-term electrocardiography recordings to detect arrhythmias in mice. JoVE (Journal of Visualized Experiments), (171), p.e62386.
4. Cheng, H., Li, Z., Guo, Z., Shao, S., **Mo, L**., Wei, W. and Xue, M., 2021. Single-cell profiling of D-2-hydroxyglutarate using surface-immobilized resazurin analogs. Biosensors and Bioelectronics, 190, p.113368.
5. Li, Z., Cheng, H., Shao, S., Lu, X., **Mo, L**., Tsang, J., Zeng, P., Guo, Z., Wang, S., Nathanson, D.A. and Heath, J.R., 2018. Surface Immobilization of Redox-Labile Fluorescent Probes: Enabling Single-Cell Co-Profiling of Aerobic Glycolysis and Oncogenic Protein Signaling Activities. Angewandte Chemie International Edition, 57(36), pp.11554-11558.
6. **Mo, L**., Chen, Y., Li, W., Guo, S., Wang, X., An, H. and Zhan, Y., 2017. Anti-tumor effects of (1→ 3)-β-d-glucan from Saccharomyces cerevisiae in S180 tumor-bearing mice. International Journal of Biological Macromolecules, 95, pp.385-392.
7. Guo, S., Chen, Y., Pang, C., Wang, X., Qi, J., **Mo, L**., Zhang, H., An, H. and Zhan, Y., 2017. Ginsenoside Rb1, a novel activator of the TMEM16A chloride channel, augments the contraction of guinea pig ileum. Pflügers Archiv-European Journal of Physiology, 469, pp.681-692.

Reviews:

1. Wang, X., Chen, Y., Zhang, Y., Guo, S., **Mo, L**., An, H. and Zhan, Y., 2017. Eag1 voltage-dependent potassium channels: structure, electrophysiological characteristics, and function in cancer. The Journal of Membrane Biology, 250, pp.123-132.

Conference contributions:

1. **Li Mo**, Philipp Tomsits, Aparna Sharma Chivukula, Ruibing Xia, Julia Vlcek, Valerie Pauly, Nora Hesse, Bianca Hildebrand, Dominik Schüttler, Zhihao Zhang, Hannes Villgrater, Fatih Kocabas, Sebastian Clauss. Investigating the mechanistic role of MEIS1 in atrial electrophysiology. Munich Heart Alliance Summer Meeting 2023 (Poster)
2. Aparna Sharma Chivukula, Kavi Raj Chataut, Philipp Tomsits, **Li Mo**, Ruibing Xia, Julia Vlcek, Bianca Hildebrand, Valerie Pauly, Nora Hesse, Zhihao Zhang, Dominik Schüttler, Ludwing T.Weckbach, Stefan Brunner, Stefan Kääb, Sebastian Clauss. Cardiac arrhythmogenesis in Myocarditis: Is exercise a friend or foe? Munich Heart Alliance Summer Meeting 2023 (Poster)
3. **Li Mo**, Philipp Tomsits, Aparna Sharma Chivukula, Ruibing Xia, Julia Vlcek, Valerie Pauly, Nora Hesse, Bianca Hildebrand, Dominik Schüttler, Zhihao Zhang, Hannes Villgrater, Fatih Kocabas, Sebastian Clauss. Investigating the mechanistic role of MEIS1 in atrial electrophysiology. ERA-Net on Cardiovascular Diseases Symposium 2022 (Poster)
4. Aparna Sharma Chivukula, Kavi Raj Chataut, Philipp Tomsits, **Li Mo**, Ruibing Xia, Julia Vlcek, Bianca Hildebrand, Valerie Pauly, Nora Hesse, Zhihao Zhang, Dominik Schüttler, Ludwing T.Weckbach, Stefan Brunner, Stefan Kääb, Sebastian Clauss. Cardiac arrhythmogenesis in Myocarditis: Is exercise a friend or foe? ERA-Net on Cardiovascular Diseases Symposium 2022 (Poster)